EXtended Finite Element and Meshfree Methods

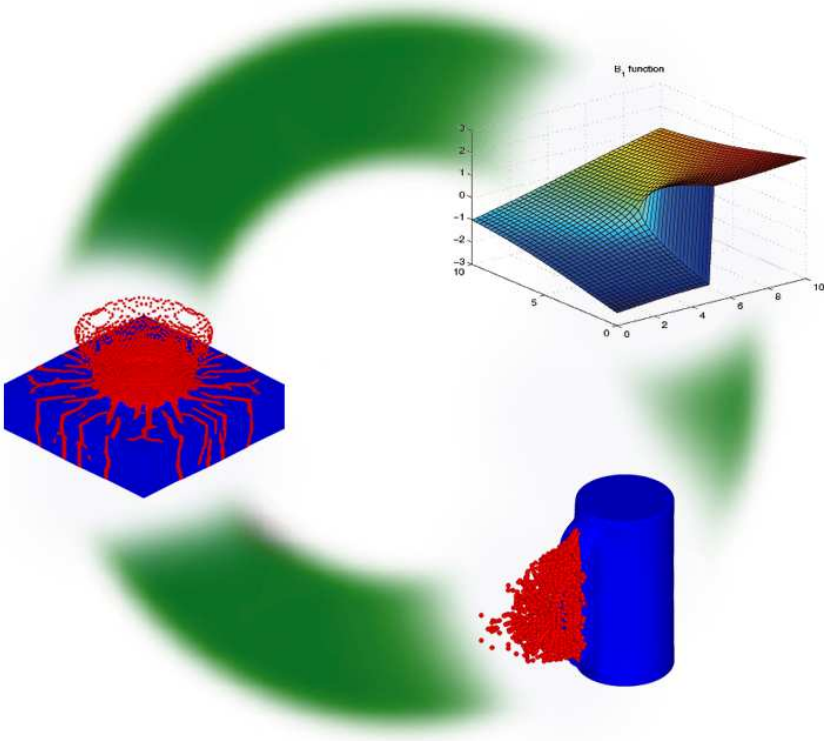

Prof. Dr.-Ing. T. Rabczuk

Chair of Mechanics
Bauhaus University Weimar
Version: SS 2009

Contents

Literature

- T. Belytschko, W.K. Liu, B. Moran: Nonlinear Finite Elements for Continua and Structures, John Wiley and Sons, 2000
- N. Moes, J. Dolbow, T. Belytschko: A finite element method for crack growth without remeshing, International Journal for Numerical Methods in Engineering, 1999, 46(1), 133-150
- T. Belytschko, J.S. Chen: Meshfree and Particle Methods, John Wiley and Sons, 2007
- S. Li, W.K. Liu: Meshfree Particle Methods, Springer, 2005
- T.P. Fries, H. Matthies: Classification and overview of meshfree methods, http://www.digibib.tu-bs.de/?docid=00001418

Preliminaries and Notations

Tensors will be written in compact notation or indicial notation. In indicial notation, the components of a tensor are explicitely specified, e.g f_i for a first order tensor, f_{ij} for a second order tensor. We use Einsein notation and sum over repeated indices. Capital indices denotes a node number, e.g g_{iI} is the first order tensor for node I. Alternatively, we write the tensor in compact notation, e.g. $f_i = \mathbf{f}$ or $f_{ij} = \mathbf{f}$. The symbol $(\cdot)$ denotes a tensor contraction, e.g $f_i g_i = r = \mathbf{f} \cdot \mathbf{g}$ or $f_{ijkl} g_{kl} = r_{ij}$ is in compact notation $\mathbf{f} : \mathbf{g} = \mathbf{r}$. The symbol $\otimes$ denotes a tensor product, e.g. $f_i g_j = r_{ij}$ is in compact notation $\mathbf{f} \otimes \mathbf{g} = \mathbf{r}$. The symbol $\times$ denotes a vector cross product, e.g. $\mathbf{f} \times \mathbf{g} = \epsilon_{ijk}\ f_i\ g_k$ where ϵ_{ijk} is the permutation tensor. We will also used Voigt notation where suitable and write $g_i = (g_1, g_2, g_3, g_{12}, g_{13}, g_{23})$ instead of g_{ij}. When we refer to quantities in the initial configuration, we use capital letters; if we refer to quantities in the current configuration, small letters are used. Therefore, let us consider a body Ω with boundary Γ; their images in the initial state are Ω_0 and Γ_0, respectively[1]. The initial state will also serve as the reference state. The motion is described by

$$\mathbf{x} = \boldsymbol{\phi}(\mathbf{X}, t), \tag{1}$$

where $\mathbf{x}$ are the spatial (Eulerian) coordinates and $\mathbf{X}$ the material (Lagrangian) coordinates. The displacement is then given by

$$\mathbf{u}(\mathbf{X}, t) = \mathbf{x} - \mathbf{X} = \boldsymbol{\phi}(\mathbf{X}, t) - \mathbf{x}, \tag{2}$$

For example, let us consider the material time derivatives of the velocity and acceleration field in a Lagrangian description[2], then we can write:

$$\begin{aligned} \mathbf{v}(\mathbf{X}, t) &= \frac{\partial \mathbf{u}(\mathbf{X}, t)}{\partial t} = \dot{\mathbf{u}} \\ \mathbf{a}(\mathbf{X}, t) &= \frac{\partial^2 \mathbf{u}(\mathbf{X}, t)}{\partial t^2} = \ddot{\mathbf{u}} \end{aligned} \tag{3}$$

where $\mathbf{u}$ is the displacement and $\mathbf{v}$ and $\mathbf{a}$ the velocity and acceleration, respectively. In Eulerian description, advective terms are present in the total time

[1] The subscript 0 is always used when we refer to quantities in the initial configuration
[2] in terms of material coordinates

derivatives:

$$\begin{aligned} \mathbf{a}(\mathbf{X},t) &= \frac{\partial \mathbf{v}(\mathbf{X},t)}{\partial t} + \frac{\partial v_i(\mathbf{x},t)}{\partial x_j}\frac{\partial x_i(\mathbf{X},t)}{\partial t} \\ \mathbf{a}(\mathbf{X},t) &= \frac{\partial \mathbf{v}(\mathbf{X},t)}{\partial t} + \frac{\partial v_i(\mathbf{x},t)}{\partial x_j}\mathbf{v} \end{aligned} \tag{4}$$

A Lagrangian description is generally used for solids while an Eulerian description of motion is used in fluid mechanics. The deformation gradient is defined by

$$\mathbf{F} = \frac{\partial \mathbf{x}}{\partial \mathbf{X}} \tag{5}$$

A strain measured that can be derived from the deformation gradient is given by

$$\boldsymbol{\epsilon} = \frac{\partial \mathbf{u}}{\mathbf{X}} = \mathbf{I} - \mathbf{F} \tag{6}$$

Another useful strain measure is the rate-of-deformation tensor

$$\mathbf{D} = 0.5\left(\mathbf{L} + \mathbf{L}^T\right) \tag{7}$$

where $\mathbf{L} = v_{i,j} = \dot{\mathbf{F}} \cdot \mathbf{F}^{-1}$ is the velocity gradient. The Green Lagrange strain tensor is defined by:

$$\mathbf{E} = 0.5\left(\mathbf{F}^T\mathbf{F} - \mathbf{I}\right) \tag{8}$$

The work-conjugate stress-tensor of the rate-of-deformation tensor is the Cauchy-stress tensor $\boldsymbol{\sigma}$ and e.g. for $\mathbf{E}$, it is the second Piola Kirchhoff stress tensor. The different stress measures can be transformed into each other. For more details, see Belytschko et al. [1].

Symbols

$[\![(\cdot)]\!]$	jump
$\frac{\partial D(\cdot)}{\partial t}, \dot{(\cdot)}$	material time derivative
$\frac{\partial(\cdot)}{\partial \mathbf{X}}, \nabla, (\cdot)_{,i}$	nabla operator

Subscripts/Superscripts

S	symmetric part of a tensor or Shepard function or stress point or crack surface
h	approximation...
u	Dirichlet...
t	von Neumann... or crack tip...
c	crack...
P	particle... or penalty...
L	Lagrange multiplier...
AL	augmented Lagrange...
std	standard...
enr	enriched...
$blnd$	blending/transition...
lin	linear...
(e)	element...
0	refer to quantities in the reference/initial configuration
max	maximum...
min	minimum...
ext	external...
int	internal...
Q	Gauss point...
a, b	enriched node
$diag$	diagonal...
kin	inertia...

Latin letters

E	Young's modulus
G	Shear modulus
K_I, K_{II}	Stress intensity factor
$x, \mathbf{x}$	spatial coordinates
$X, \mathbf{X}$	material coordinates
$u, \mathbf{u}$	displacement
$\mathbf{d}$	displacement vector

$v, \mathbf{v}$	velocities
$a, \mathbf{a}$	accelarations or enrichment
$t, \mathbf{t}$	traction
$\mathbf{n}$	normal
$\mathbf{b}$	body forces or enrichment
$p, \mathbf{p}$	basis polynomial or penalty parameter
$m, \mathbf{m}$	mass or mass matrix
$M, \mathbf{M}$	mass or mass matrix
w	quadrature weights or meshfree shape function
W	kernel/window/weighting function
V	volume or quadrature weight
A	arrea
h	dilation parameter
R	support size
$\mathbf{f}$	force
$\mathbf{F}$	deformation gradient or force
$\mathbf{r}$	residuum
$P, \mathbf{P}$	first Piola Kirchhoff stress
$\mathbf{K}$	stiffness matrix
$N, \mathbf{N}$	shape function
$\mathbf{B}$	B-operator or branch enrichment
$\mathbf{C}$	material tangent matrix
$\mathbf{I}$	identity tensor
J	Jacobian
e	error or internal energy
r, s	local element coordinates
S	crack surface or step function
H	Heaviside function
$\mathcal{S}$	set of nodes

Greek letters

$\lambda, \boldsymbol{\lambda}$	Lagrange multiplier or Lagrange multiplier estimate or eigenvalue
$\Lambda, \boldsymbol{\Lambda}$	Lagrange multiplier estimate or Lagrange multiplier shape function
Π	potential
β	scaling parameter
Δ	increment...
β	scaling parameter
κ	condition number
$\mathcal{K}$	curvature
ϵ_{ijk}	permutation tensor
$\epsilon, \boldsymbol{\epsilon}$	strain
$\sigma, \boldsymbol{\sigma}$	Cauchy stress
$\sigma_{\theta\theta}$	hoop stress

ψ	enrichment function
Ψ	shape function or smoothing function
ϕ	level set
Φ	meshfree shape function
$\delta, \boldsymbol{\delta}$	variation or Kronecker delta or dirac delta function
ξ, η	local element coordinates
ϱ	density
Ω	domain
Γ	boundary

Chapter 1

Introduction

Finite element methods are a very powerful numerical tool to study, predict and model the behavior of materials, structures, fluids and events. They were successfully applied in many areas in Engineering Science. Applications range from the automobile industry, Aerospace and Aeronautical Engineering, Environmental Engineering, over Mechanical and Civil Engineering to Geomechanics, Biomechanics and Material science. Even scientists from disciplines such as applied maths, physics and computational chemistry use finite element methods. Finite element methods can be used as design tool. A typical Engineering application is the design of cars, ships, aircrafts, bridges, dams, armor, new materials etc. Many aspects are studied with finite elements including fluid mechanics, solid mechanics and fluid-fluid-interaction as well as fluid-structure interaction, e.g. the aerodynamic behavior, pollution, acoustic emission, safety and reliability analysis, etc. Finite elements can also be used as predictive tools, e.g. crack growths of existing flaws in wings of aircrafts, avalanches, land slides, damage of human tissue in arteries or the pulmonary system, to name a few applications.

However, while standard finite elements have a wide application spectrum, there are still limitations where standard finite elements do not give acceptable results. One class of problems that finite elements are not able to capture sufficiently are problems that involve strong and weak discontinuities, i.e. jump in the displacement and strain field, respectively. There are two huge application spectra that involve strong and weak discontintuities:

1. Fracture and computational failure mechanics that involves the initiation and propagation of cracks, i.e. strong discontinuities.

2. So-called interface problems, that can be classified into solid-solid, solid-fluid and fluid-fluid interfaces. While solid-fluid interface problems are applications with strong discontinuities, solid-solid and fluid-fluid interface problems involve weak discontinuities.

Standard finite elements are not well suited for such kind of problems due to their smooth interpolation character. The shape function of standard finite elements are piecewise polynomials and strong and weak discontinuities can be incorporated only along element edges. For cracks for example, the numerical results become very sensitive with respect to the orientation of the mesh and also with respect to the chosen size and shape of the elements. Sufficient results can only be obtained by computational expensive remeshing procedures. The data from the old mesh has to be mapped to the new mesh that also leads to loss of accuracy. Similar problems occur in fluid mechanics when the inferface of two different fluids or a fluid and a structure has to be captured.

Within this lecture, extended finite element and meshfree methods will be studied that can handle arbitrary strong and weak discontinuities. These methods modify the approximation space of the test and trial function, such that arbitrary strong and weak discontinuities can be handled. Though it sounds at first illogical, extended finite element methods were born out of meshfree methods. Hence, the lecture will first discuss meshfree methods and some basic concepts that are inherent of extended finite element methods. We will see that meshfree methods have certain advantages over finite element methods with respect to certain applications. These aspects will be discussed within this lecture.

At the end of the lecture you should know

- what is a *global* and *local* partition of unity and how it is related to completeness
- what is completeness and continuity
- what is a Lagrangian and Eulerian kernel function
- what is SPH, RKPM, EFG, PUFEM and how to derive the shape functions of these methods
- what is the difference between an intrinsic and extrinsic basis
- how to derive a weak form from a strong form (and vice versa)
- how to perform a nodal, stress-point and cell-integration in a meshfree method
- how to derive discrete meshfree equations
- why meshfree methods have difficulties in imposing Dirichlet boundary conditions and how to impose them
- what is a strong and weak discontinuity
- how to incorporate strong discontinuities in a meshfree method
- what is a level set and a signed distance function

- the principal of XFEM
- how to incorporate a strong and weak discontinuity in XFEM
- the implementation procedure in XFEM
- different possibilities to close a crack at its crack tip within XFEM
- the principal of Embedded elements and Interface elements

Chapter 2

Meshfree methods

2.1 Completeness, consistency and Partition of Unity

Completeness in finite element and meshfree methods plays the same role as consistency in finite difference methods, Belytschko et al. [1]. While for finite differences, consistency describes how good the difference scheme approximates the differential operator, completeness is expressed in terms of the order of the polynomial which must be represented exactly. For functions depending on the coordinates $\mathbf{X}$, completeness can be stated as follows: a set of approximating functions $\Phi_J(\mathbf{X})$ reproduce $p(\mathbf{X})$ with $u_J = p(\mathbf{X}_J)$, when

$$\Phi_J(\mathbf{X})\ u_J = \Phi_J(\mathbf{X})\ p(\mathbf{X}_J) = p(\mathbf{X}) \tag{2.1}$$

If the approximation is able to reproduce a constant function, then the approximation is called zero-order complete. If the approximation can reproduce linear functions exactly, it is called first-order complete or linear complete and so on. The term *completeness* is sometimes referred to as *reproducing conditions*. In two dimensions, the constant and linear reproducing conditions are given by

$$\sum_J \Phi_J(\mathbf{X}) = 1 \tag{2.2}$$

$$\sum_J \Phi_J(\mathbf{X})\ X_J = X \quad \sum_J \Phi_J(\mathbf{X})\ Y_J = Y \tag{2.3}$$

or in indicial notation

$$\sum_J \Phi_J(\mathbf{X})\ X_{Ji} = X_i \tag{2.4}$$

If the derivatives of a polynomial field is reproduced correctly, we call this the derivative reproducing conditions. In two dimensions, the derivative reproduc-

ing conditions for a constant and linear field are given by

$$\sum_J \Phi_{J,X}(\mathbf{X}) = 0 \quad \sum_J \Phi_{J,Y}(\mathbf{X}) = 0 \tag{2.5}$$

$$\sum_J \Phi_{J,X}(\mathbf{X})\ X_J = 1 \quad \sum_J \Phi_{J,Y}(\mathbf{X})\ X_J = 0 \tag{2.6}$$

$$\sum_J \Phi_{J,X}(\mathbf{X})\ Y_J = 0 \quad \sum_J \Phi_{J,Y}(\mathbf{X})\ Y_J = 1 \tag{2.7}$$

or in indicial notation

$$\sum_J \Phi_{J,i}(\mathbf{X}) = 0 \quad \sum_J \Phi_{J,i}(\mathbf{X})\ X_{Jj} = \delta_{ij} \tag{2.8}$$

If the approximating functions $\Phi_J(\mathbf{x})$ can reproduce the constant and assuming that $u_J = 1$, the approximation should be exactly unity (see eq. (2.2))

$$\sum_J \Phi_J(\mathbf{x}) = 1$$

Functions that possess this property are called *partition of unities* (PU). Isoparametric finite element shape functions meet this condition. Hence, isoparametric finite elements can be classified in the category of partition of unity methods.

2.2 Conservation, stability and convergence

Belytschko et al. [2] have shown that a discretization has to be zero-order complete to guarantee conservation of linear momentum and linear complete to guarantee conservation of angular momentum.

Conservation of linear momentum requires that the rate of change of linear momentum equals the total applied force such that the total change of linear momentum due to internal forces is zero. Thus, in the absence of external forces and body forces, conservation of linear momentum requires that

$$\frac{D}{Dt}\left(\sum_{I\in\mathcal{S}} m_I \mathbf{v}_I\right) = \sum_{I\in\mathcal{S}} m_I \dot{\mathbf{v}}_I = 0 \tag{2.9}$$

where m_I are nodal masses and $\mathbf{v}$ the velocity field. From the linear momentum equation (without external and body forces) we know that

$$m_I \dot{\mathbf{v}}_I = -\sum_{J\in\mathcal{S}} \nabla\Phi_I(\mathbf{X}_J)\cdot\boldsymbol{\sigma}(\mathbf{X}_J)\ w_J \tag{2.10}$$

where $\Phi_I(\mathbf{X}_J)$ are shape functions and w_J are the quadrature weights. Substituting the RHS of eq. (2.10) into eq. (2.9) gives

$$\sum_{I\in\mathcal{S}} m_I \mathbf{v}_I = -\sum_{I\in\mathcal{S}}\sum_{J\in\mathcal{S}} \nabla\Phi_I(\mathbf{X}_J)\cdot\boldsymbol{\sigma}(\mathbf{X}_J)\ w_J = -\sum_{J\in\mathcal{S}}\sum_{I\in\mathcal{S}} \nabla\Phi_I(\mathbf{X}_J)\cdot\boldsymbol{\sigma}(\mathbf{X}_J)\ w_J = 0 \tag{2.11}$$

that requires that $\sum_{I \in \mathcal{S}} \nabla \Phi_I(\mathbf{X}_J) = 0$ for arbitrary stress states that in turn requires zero-order complete shape functions.

Conservation of angular momentum requires that any change in angular momentum is exclusively due to external forces. Hence, let us show that the change of angular momentum in the absence of external forces vanishes. The time rate of change of angular momentum in the absence of external forces can be expressed as

$$\frac{D}{Dt}\left(\sum_I m_I \mathbf{v}_I \times \mathbf{X}_I\right) = \sum_I m_I \left(\dot{\mathbf{v}}_I \times \mathbf{X}_I + \underbrace{\mathbf{v}_I \times \mathbf{v}_I}_{=0}\right) = 0 \tag{2.12}$$

Here, $\times$ denotes the vector cross product. Substituting eq. (2.10) into eq. (2.12) leads to

$$\frac{D}{Dt}\left(\sum_I m_I \mathbf{v}_I \times \mathbf{X}_I\right) = \sum_I \epsilon_{ijk} \left(\sum_J \Phi_{I,m}(\mathbf{X}_J)\ \sigma_{mj}(\mathbf{X}_J) w_J\right) X_{Ik} \tag{2.13}$$

where ϵ_{ijk} is the permutation tensor and X_{Ik} refers to the $k-th$ component of particle I. We sum over repeated indices. Eq. (2.13) can be reformulated to

$$\epsilon_{ijk} \sum_J \underbrace{\left(\sum_I \Phi_{I,m}(\mathbf{X}_J) X_{Ik}\right)}_{\delta_{mk}} \sigma_{mj}(\mathbf{X}_J) w_J = \epsilon_{ijk} \delta_{mk} \sum_J \sigma_{mj}(\mathbf{X}_J) w_J$$

$$= \sum_J \underbrace{\epsilon_{ijm} \sigma_{mj}(\mathbf{X}_J)}_{=0} w_J = 0 \tag{2.14}$$

Note, that we used the linear reproducing conditions of the derivatives of the approximation and the symmetry of the Cauchy stress tensor.

A method is convergent of order k ($k > 0$) if

$$\underbrace{\max}_{i} |u(X_i) - u_i| \leq C h^k \tag{2.15}$$

where C is a constant and h is the dilation parameter in meshfree methods[1] defined later. According to the Lax-Richtmeyr equivalence theorem, a method is convergent if it is consistent and stable. Stability guarantees that a small defect in the discretization remains small. As already mentioned, completeness takes the role of consistency in a Galerkin methods.

2.3 Continuity

An approximation is considered to be $\mathcal{C}^n$ if its approximating functions are n times continuous differentiable.

[1] h would denote the element size in finite elements

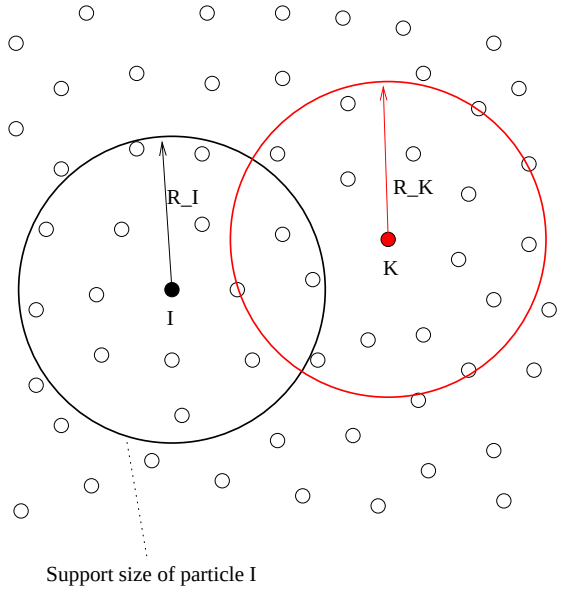

Figure 2.1: Support size of the kernel function

2.4 The weighting function

2.4.1 Requirements of the weighting function

The weighting function plays an important role in meshfree methods. Other names for the weighting function are window and kernel function. Typically, three requirements are imposed on the kernel function:

$$\underbrace{\lim}_{h_0 \to 0} W(\mathbf{X}_I - \mathbf{X}_J, h_0) = \delta(\mathbf{X}_I - \mathbf{X}_J) \tag{2.16}$$

$$\int_{\Omega_0} W(\mathbf{X}_I - \mathbf{X}_J, h_0) d\Omega_0 = 1 \tag{2.17}$$

$$W(\mathbf{X}_I - \mathbf{X}_J, h_0) = 0 \quad \forall \ \mathbf{X}_I - \mathbf{X}_J \geq R \tag{2.18}$$

where δ denotes the Dirac delta function, h_0 is a shape or dilation parameter that determines the size of the domain of influence of the kernel and R is a shape parameter often related to h_0, see figure 2.1. The last condition is called compact support of the shape function. It can be shown that there is an optimal value for the ratio between the dilation parameter h_0 and the distance between particles x. Figure 2.2 shows that for a fixed distribution of particles, x constant, the dilation parameter must be large enough to avoid aliasing (spurious short waves in the approximated solution). It also shows that an excessively large value for h_0 will lead to excessive smoothing. For this reason, it is common to

maintain a constant ratio between the dilation parameter h_0 and the distance between particles x. In most applications, the ratio between the support size[2] and particle separation x lies in the range between 2.8 and 3.2. Usually, also the following symmetry conditions are imposed on the kernel function:

$$W(\mathbf{X}_I - \mathbf{X}_J, h_0) = W(\mathbf{X}_J - \mathbf{X}_I, h_0) \tag{2.19}$$
$$\nabla_0 W(\mathbf{X}_I - \mathbf{X}_J, h_0) = -\nabla_0 W(\mathbf{X}_J - \mathbf{X}_I, h_0) \tag{2.20}$$

There are basically two ways to construct kernel functions in higher order dimensions that lead to different sizes and shapes of the domain of influence. Either, the kernel function has spherical support

$$W(\mathbf{X}) = W_{1D}(\|\mathbf{X}\|), \tag{2.21}$$

or the kernel function has rectangular support

$$W(\mathbf{X}) = W_{1D}(|X_1|)\, W_{1D}(|X_2|)\, W_{1D}(|X_3|) \tag{2.22}$$

where $\mathbf{X} = (X_1, X_2, X_3)$ and $\|\mathbf{X}\| = \sqrt{X_1^2 + X_2^2 + X_3^2}$.

2.4.2 Specific weighting functions

A very popular kernel function is the cubic B-spline given by:

$$\mathrm{W(r)} = \begin{cases} \frac{C}{h^D}\left(1 - 1.5z^2 + 0.75z^3\right) & 0 \le z < 1 \\ \frac{C}{4\,h^D}\left(2 - z\right)^3 & 1 \le z \le 2 \\ 0 & z > 2 \end{cases} \tag{2.23}$$

where D is the dimension, $z = r/h_0$ and C is a constant depending on the dimension

$$\mathrm{C} = \begin{cases} 2/3 & D = 1 \\ 10/(7\,\pi) & D = 2 \\ 1/\pi & D = 3 \end{cases} \tag{2.24}$$

Note, that it is standard to scale the weighting function with the dilation parameter h_0 and express it in non-dimensional form (in terms of z). The first spatial derivatives of the cubic B-spline are obtained by standard differentiation. Defining $\bar{z} = ||\mathbf{X}_I - \mathbf{X}_J||$, we obtain

$$\frac{\partial W}{\partial X_{iJ}} = \frac{\partial W}{\partial \bar{z}} \frac{\partial \bar{z}}{\partial X_{iJ}} \tag{2.25}$$

with

$$\frac{\partial W}{\partial \bar{z}} = \begin{cases} \frac{3C}{h^{D+1}}\left(-z + 0.75z^2\right) & 0 \le z < 1 \\ \frac{-3C}{4\,h^{D+1}}\left(2 - z\right)^2 & 1 \le z \le 2 \\ 0 & z > 2 \end{cases} \tag{2.26}$$

The one dimensional cubic B-spline and its first spatial derivative is shown in

[2] Note that the support size is proportional to the dilation parameter

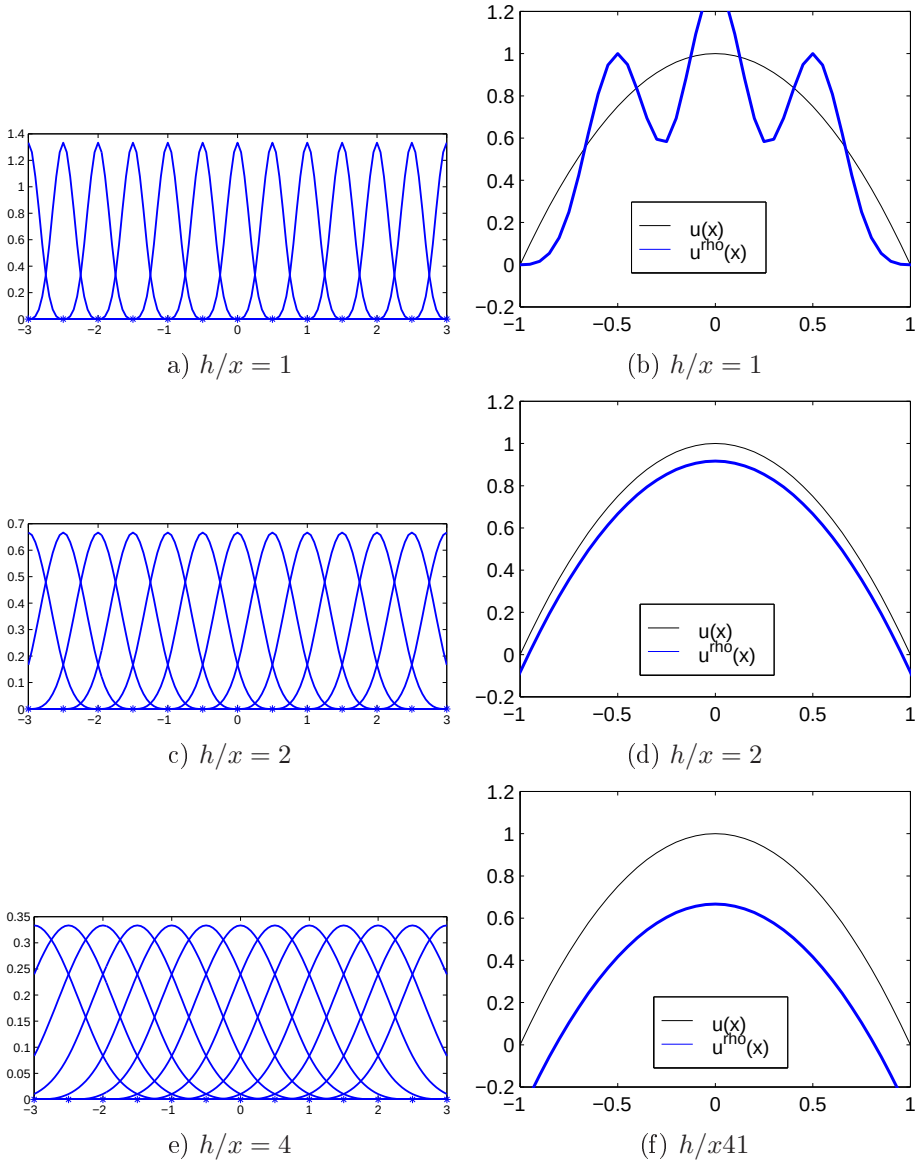

a) $h/x = 1$ (b) $h/x = 1$

c) $h/x = 2$ (d) $h/x = 2$

e) $h/x = 4$ (f) $h/x41$

Figure 2.2: Meshfree (SPH) approximation functions and approximation of $u(x) = 1 - x^2$ with cubic spline window function, distance between particles $x = 0.5$ and quadrature weights $\omega_i = x$, for $h/x = 1, 2, 4$, from [3]

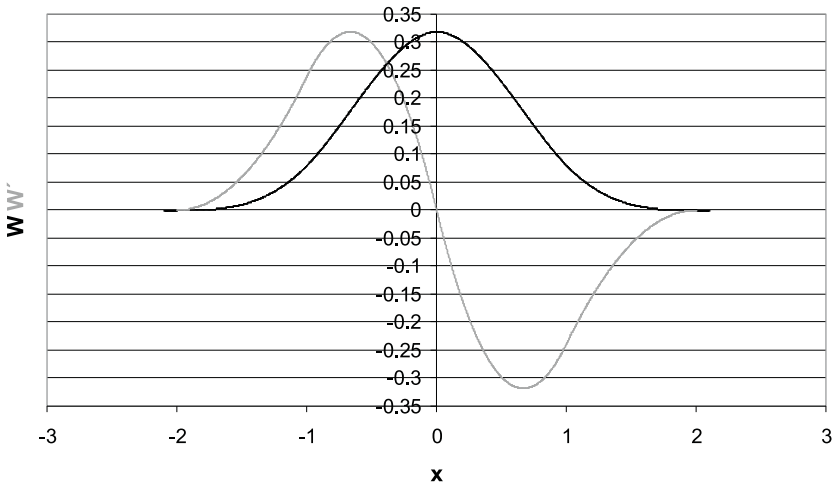

Figure 2.3: Typical kernel function and its first derivative in one dimension

figure 2.3. Another popular kernel is the quartic spline:

$$\mathrm{W(r)} = \begin{cases} 1 - 6z^2 + 8z^3 - 3z^4 & 0 \leq z < 1 \\ 0 & 1 \leq z \end{cases} \tag{2.27}$$

Other kernels are for example:

$$\mathrm{W(r)} = \begin{cases} \|\mathbf{x} - \mathbf{x}_I\| \equiv r & \text{linear} \\ z^2 \log z & \text{thin plate spline} \\ e^{-z^2/c^2} & \text{Gaussian} \\ \left(z^2 + R^2\right)^q & \text{multipolar} \end{cases} \tag{2.28}$$

where c, R and q are shape parameters.

2.4.3 Eulerian and Lagrangian kernels

When the kernel function is expressed in terms of spatial coordinates, we call it an Eulerian kernel:

$$W_J(\mathbf{x}) = W(\mathbf{x} - \mathbf{x}_J(t), h(\mathbf{x}, t)) \tag{2.29}$$

The radius h of the support depends on the spatial coordinates and can change in time. Simple approaches to update h are given by:

$$\begin{aligned} h^{t+\Delta t} &= h^t + \dot{h}\ \Delta t \\ \dot{h} &= 1/3\ \varrho\ \nabla \cdot \mathbf{v} \end{aligned} \tag{2.30}$$

where $\mathbf{v}$ indicates the particle velocity and ϱ is the density. However, the shape of the domain of influence of a given particle still remains a sphere. More realistic tensorial support sizes $\mathbf{h}$ can be obtained by means of the deformation gradient $\mathbf{F}$:

$$\mathbf{h} = h_0 \ \mathbf{F} \tag{2.31}$$

For radial supported shape functions, $\mathbf{h}$ spans a sphere in the initial configuration with h_0 as radius. In the current configuration, the domain of influence becomes an ellipsoid where the eigenvectors of $\mathbf{h}$ span the axis of that ellipsoid.

When the kernel function is expressed in terms of material coordinates, it is called a Lagrangian kernel:

$$W_J(\mathbf{X}) = W(\mathbf{X} - \mathbf{X}_J, h_0) \tag{2.32}$$

For Lagrangian kernels, the neighbors of influence do not change during the course of the simulation but the domain of influence in the current configuration changes with time. For radial kernel functions, the domain of influence in the initial configuration is a circle in two dimensions. In the current configuration the domain of influence can be extremely distorted. This is a disadvantage in simulating fluid flow problems and other problems with very large distortions. On the other hand, it can be shown that many meshfree methods based on Eulerian kernels introduce a so called tensile instability that is not present in meshfree methods based on Lagrangian kernels.

Note that most meshfree methods that use an Eulerian kernel are based on a Lagrangian description of motion. In other words, the standard derivation of the acceleration omits the time dependence of $\mathbf{x}_J(t)$. If we let

$$\mathbf{v}(\mathbf{x}, t) = \sum_{I \in S} W(\mathbf{x} - \mathbf{x}_I(t)) \ \mathbf{v}_I(t), \tag{2.33}$$

then the accelerations are

$$\mathbf{a} = \sum_{I \in S} W(\mathbf{x} - \mathbf{x}_I(t)) \ \dot{\mathbf{v}}_I + \nabla W(\mathbf{x} - \mathbf{x}_I(t)) \ \dot{\mathbf{x}}_I \cdot \mathbf{v}_I. \tag{2.34}$$

The second term is neglected in most Eulerian kernel based meshfree methods. This inconsistency causes severe difficulties when modeling material failure with Eulerian based meshfree methods.

2.5 Specific meshfree approximations

A meshfree approximation can be written as the approximation for finite elements:

$$u^h(\mathbf{X}, t) = \sum_{J \in \mathcal{S}} u_J(t) \ \Phi_J(\mathbf{X}) \tag{2.35}$$

where u_J are the nodal parameters, $\Phi_J(\mathbf{X})$ are the shape functions and $\mathcal{S}$ is the set of nodes with $\Phi_J(\mathbf{X}) \neq 0$. We note one substantial difference between

the meshfree and the finite element approximation. While finite elements are real interpolants, meshfree shape functions are approximants, i.e. they do not go through the data ($\mathbf{u}^h(\mathbf{x}_I) \neq \mathbf{u}_I$ for meshfree methods). In other words, meshfree methods do not fulfill a condition often refered to as Kronecker-Delta property $\Phi_I(\mathbf{X}_J) = \delta_{IJ}$ where δ_{IJ} is the Kronecker delta. This condition is obviously fulfilled by a finite element formulation but it is violated by almost every meshfree approximation. This causes difficulities in imposing Dirichlet boundary conditions. If the shape functions do not vanish along the boundaries, they do not allow for the space $\mathcal{H}^1$ to be represented exactly. This issue will be addressed in detail in section 2.9.

In the following, we will derive all methods in terms of material coordinates (and in terms of a Lagrangian kernel). The equations in terms of spatial coordinates are obtained in the same manner.

2.5.1 Smooth Particle Hydrodynamics (SPH)

The continuous SPH-form

The continuous SPH approximation is given by:

$$u^h(\mathbf{X},t) = \int_{\Omega_0} u(\mathbf{Y},t)\; W\left(\mathbf{X}-\mathbf{Y}, h_0(\mathbf{Y})\right)\; dY \tag{2.36}$$

where Ω_0 is the domain of the problem. The constant reproducing condition

$$\int_{\Omega_0} W\left(\mathbf{X}-\mathbf{Y}, h_0(\mathbf{Y})\right)\; 1\; dY = 1 \tag{2.37}$$

is fulfilled by definition, see eq. (2.16). Linear completeness requires that

$$\int_{\Omega_0} W\left(\mathbf{X}-\mathbf{Y}, h_0(\mathbf{Y})\right)\; Y\; dY = X \tag{2.38}$$

Noting that eq. (2.37) requires that

$$\int_{\Omega_0} W\left(\mathbf{X}-\mathbf{Y}, h_0(\mathbf{Y})\right)\; X\; dY = X \tag{2.39}$$

and subtracting eq. (2.39) from eq. (2.38) leads to

$$\int_{\Omega_0} W\left(\mathbf{X}-\mathbf{Y}, h_0(\mathbf{Y})\right)\; (X-Y)\; dY = 0 \tag{2.40}$$

This integral is the first moment of the weighting function. The above equation is met if the weighting function is symmetric about its origin. Hence, the continuous SPH form is linear complete.

The spatial partial derivatives of $u^h(\mathbf{X},t)$ are given by

$$\nabla_0 u^h(\mathbf{X},t) = \int_{\Omega_0} \nabla_0 u(\mathbf{Y},t)\; W\left(\mathbf{X}-\mathbf{Y}, h_0(\mathbf{Y})\right)\; dY \tag{2.41}$$

Integration by parts gives

$$\begin{aligned}\nabla_0 u^h(\mathbf{X},t) &= \int_{\Omega_0} \nabla_0 \left[u(\mathbf{Y},t)\; W\left(\mathbf{X}-\mathbf{Y},h_0(\mathbf{Y})\right)\right]\; dY \\ &- \int_{\Omega_0} \nabla_0 u(\mathbf{Y},t)\; W\left(\mathbf{X}-\mathbf{Y},h_0(\mathbf{Y})\right)\; dY \end{aligned} \tag{2.42}$$

Applying the divergence theorem on the first term of the RHS of eq. (2.42), we obtain

$$\begin{aligned}\nabla_0 u^h(\mathbf{X},t) &= \int_{\Gamma_0} u(\mathbf{Y},t)\; W\left(\mathbf{X}-\mathbf{Y},h_0(\mathbf{Y})\right)\; \mathbf{n}_0\; d\Gamma_0 \\ &- \int_{\Omega_0} \nabla_0 u(\mathbf{Y},t)\; W\left(\mathbf{X}-\mathbf{Y},h_0(\mathbf{Y})\right)\; dY \end{aligned} \tag{2.43}$$

In all SPH versions, the surface integrals are neglected so that the final approximation of the derivatives are

$$\nabla_0 u^h(\mathbf{X},t) = -\int_{\Omega_0} \nabla_0 u(\mathbf{Y},t)\; W\left(\mathbf{X}-\mathbf{Y},h_0(\mathbf{Y})\right)\; dY \tag{2.44}$$

The discrete SPH-form

In the discrete SPH method, the shape functions are given by a product of the particle volume and the weighting function:

$$\Phi_J(\mathbf{X}) = W(\mathbf{X}-\mathbf{X}_J,h_0)\, V_J^0 \tag{2.45}$$

where V_J^0 is the volume in the initial configuration[3] associated with the node J. In the application to partial differential equations (PDEs), an approximation of a function gradient is needed. In SPH, an approximation of the gradient of a function is given by

$$\nabla_0 u^h(\mathbf{X}) = -\sum_{J\in\mathcal{S}} u_J \nabla_0 \Phi_J(\mathbf{X}) \quad \text{with} \quad \nabla_0 \Phi_J = \nabla_0 W(\mathbf{X}-\mathbf{X}_J,h_0)\, V_J^0 \tag{2.46}$$

where the minus sign results from the integration by parts, see eq. (2.42).

It can easily be shown that the discrete SPH form is unable to reproduce even constant functions correctly even for uniformly spaced particle arrangements. Therefore, consider a one-dimensional uniform particle arrangement as shown in figure 2.4. Particles are located at the positions 2,3,4,5. The dilation parameter is chosen to be twice the particle distance, we use the cubic B-spline as kernel function and try to reproduce the constant function of 1. Figure 2.4 shows the values of every single kernel function and its superposition. We note that the zero-order completeness is not fulfilled at the boundaries. For an uneven particle arrangement, the results will get even worse.

[3] Note that V_J^0 is the quadrature weight

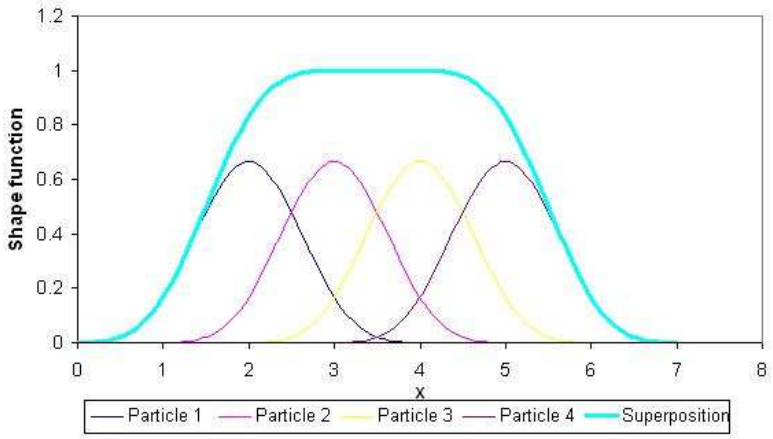

Figure 2.4: Shape functions of the SPH approximation in one dimension

Since equation (2.46) does not fulfill zero-order completeness on the boundary even for a regular particle configuration, Gingold and Monaghan [4] introduced a so called symmetrization. In this procedure they assume that

$$\left(\sum_{J \in \mathcal{S}} \nabla_0 W(\mathbf{X} - \mathbf{X}_J, h_0)\ V_J^0 \right)\ u_I \equiv 0 \tag{2.47}$$

although this is only true for a uniform distribution of particles away from any boundary. Note that eq. (2.47) is equivalent to assuming zero-order completeness (note the quantity inside the parenthesis in (2.47)). Subtracting equation (2.46) to equation (2.47) gives

$$\nabla_0 u_h(\mathbf{X}) = \sum_{J \in \mathcal{S}} (u_J - u_I)\, \nabla_0 W(\mathbf{X}_I - \mathbf{X}_J, h_0)\ V_J^0 \tag{2.48}$$

A remarkable feature of the symmetrization procedure is that it yields zero-order completeness for the derivatives of a function for an irregular particle arrangement.

2.5.2 Corrected SPH forms

The Krongauz-Belytschko correction

Johnson and Beissel [5] noted that errors in the extensional strains due to lack of linear completeness could be corrected by simple scaling, thus improving accuracy. Another correction that enables the derivatives of constant or linear

fields to be reproduced exactly was developed by Krongauz and Belytschko [6]. The corrected derivatives are approximated by

$$\nabla_0 u^h(\mathbf{X},t) = \sum_{I\in\mathcal{S}} \mathbf{G}_I(\mathbf{X})\ u_I(t) \tag{2.49}$$

or in iditial notation

$$u^h_{,i}(\mathbf{X},t) = \sum_{I\in\mathcal{S}} G_{iI}(\mathbf{X})\ u_I(t) \tag{2.50}$$

where $\mathbf{G}_I$ is a linear combination of the Shepard functions:

$$W_I^S(\mathbf{X}) = \frac{W_I(\mathbf{X})}{\sum\limits_{I\in\mathcal{S}} W_I(\mathbf{X})} \tag{2.51}$$

The approximation functions for the derivatives $\mathbf{G}_I$ are defined as linear combinations of the exact derivatives by a linear transformation

$$\mathbf{G}_I(\mathbf{X}) = \mathbf{a}(\mathbf{X}) \cdot \nabla_0 W_I^S(\mathbf{X}) = a_{ij}(\mathbf{X}) W_{jI}^S(\mathbf{X}) \tag{2.52}$$

where $\mathbf{a}(\mathbf{X})$ are arbitrary parameters. To obtain linear complete reproducing conditions for the derivatives of the approximation, the following reproducing condition for the derivative of a linear function must be fulfilled (see also eq. (2.8)):

$$\sum_{I\in\mathcal{S}} \mathbf{G}_I(\mathbf{X}) \otimes \mathbf{X}_I = \delta_{ij} \tag{2.53}$$

Let $\mathbf{A}$ be the matrix of the cross product between the derivatives of the Shepard function and the Lagrangian coordinate vector. Then the parameters $\mathbf{a}$ can be easily determined from

$$\mathbf{A}\ \mathbf{a}^T = \mathbf{I} \tag{2.54}$$

where $\mathbf{I}$ is the identity matrix and

$$\mathbf{A} = \begin{bmatrix} W_{I,X}^S\ X_I & W_{I,Y}^S\ X_I \\ W_{I,X}^S\ Y_I & W_{I,Y}^S\ Y_I \end{bmatrix}$$

$$\mathbf{a} = \begin{bmatrix} a_{XX} & a_{XY} \\ a_{YX} & a_{YY} \end{bmatrix}$$

Finally, we obtain the approximation for the derivatives of a function from (2.52) and (2.53) as

$$\nabla_0 u^h(\mathbf{X},t) = \sum_{I\in\mathcal{S}} \mathbf{a}(\mathbf{X}) \cdot \nabla_0 W_I^S(\mathbf{X})\ u_I(t) \tag{2.55}$$

Alternative 1

The corrected derivatives can also be obtained by a correction of the form

$$\begin{aligned} \Phi_I &= (a_{11}(\mathbf{X}) + a_{12}(\mathbf{X}) + a_{13}(\mathbf{X}))\, W_I^S(\mathbf{X}) \\ G_{XI} &= (a_{21}(\mathbf{X}) + a_{22}(\mathbf{X}) + a_{23}(\mathbf{X}))\, W_I^S(\mathbf{X}) \\ G_{YI} &= (a_{31}(\mathbf{X}) + a_{32}(\mathbf{X}) + a_{33}(\mathbf{X}))\, W_I^S(\mathbf{X}) \end{aligned} \tag{2.56}$$

If the coordinate system is shifted to the point of evaluation $\mathbf{X}$, then the coefficients $\mathbf{a}$ are obtained as in (2.54) with $\mathbf{A}$ given by

$$\mathbf{A} = \sum_I W_I^S(\mathbf{X}) \begin{bmatrix} 1 & X_I - X & Y_I - Y \\ X_I - X & (X_I - X)^2 & (X_I - X)(Y_I - Y) \\ Y_I - Y & (X_I - X)(Y_I - Y) & (Y_I - Y)^2 \end{bmatrix}$$

In contrast to the method above, a 3×3 matrix needs to be inverted. An advantage of this method is that linear complete shape functions are obtained in addition to the linear complete corrected derivatives.

Alternative 2

Consider shape functions and shape function derivatives of the form

$$\begin{aligned} \bar{\Phi}_I &= a_{11}(\mathbf{X}) W_{I,X}^S(\mathbf{X}) + a_{12}(\mathbf{X}) W_{I,Y}^S(\mathbf{X}) + a_{13}(\mathbf{X}) W_I^S(\mathbf{X}) \\ G_{XI} &= a_{21}(\mathbf{X}) W_{I,X}^S(\mathbf{X}) + a_{22}(\mathbf{X}) W_{I,Y}^S(\mathbf{X}) + a_{23}(\mathbf{X}) W_I^S(\mathbf{X}) \\ G_{YI} &= a_{31}(\mathbf{X}) W_{I,X}^S(\mathbf{X}) + a_{32}(\mathbf{X}) W_{I,Y}^S(\mathbf{X}) + a_{33}(\mathbf{X}) W_I^S(\mathbf{X}) \end{aligned} \tag{2.57}$$

Now, $\mathbf{a}$ is obtained by requiring the approximation $\bar{\Phi}$ to reproduce linear functions and the derivatives of the approximation to reproduce the derivatives of linear functions. To achieve this, (2.57) is substituted into the constant and linear reproducing conditions, eqs. (2.2) to (2.8). Shifting the coordinate system to the point of evaluation $\mathbf{X}$, the coefficients $\mathbf{a}$ can be obtained by (2.54) with

$$\mathbf{A} = \sum_I \begin{bmatrix} W_{I,X}^S(\mathbf{X}) & W_{I,Y}^S(\mathbf{X}) & W_I^S(\mathbf{X}) \\ W_{I,X}^S(\mathbf{X})\ X_I & W_{I,Y}^S(\mathbf{X})\ X_I & W_I^S(\mathbf{X})\ X_I \\ W_{I,X}^S(\mathbf{X})\ Y_I & W_{I,Y}^S(\mathbf{X})\ Y_I & W_I^S(\mathbf{X})\ Y_I \end{bmatrix}$$

As in Alternative 1, the computational cost is higher, but therefore the shape functions themselves are able to reproduce linear functions.

Interpolation estimate

Let us show for the two dimensional case that for derivative approximations which satisfy linear reproducing conditions, the errors in derivative approximants are of order $O(h)$. Therefore, let us develop the function $u(\mathbf{X})$ into a Taylor series expansion around $\mathbf{X}$:

$$\begin{aligned} u(\mathbf{X}_I) &= u(\mathbf{X}) + u_{,X}(\mathbf{X})\,(X_I - X) \\ &+ u_{,Y}(\mathbf{X})\,(Y_I - Y) + 0.5 u_{,XX}(\mathbf{X})\,(X_I - X)^2 \\ &+ u_{,XY}(\mathbf{X})\,(X_I - X)\,(Y_I - Y) \\ &+ 0.5 u_{,YY}(\mathbf{X})\,(Y_I - Y)^2 + O(h^3) \end{aligned} \tag{2.58}$$

Ignoring higher order terms, we can write $u^h_{,X}(\mathbf{X}) - u_{,X}$ as

$$\begin{aligned} u^h_{,X}(\mathbf{X}) - u_{,X} &= \sum_I G_{XI}(\mathbf{X})\ u_I - u_{,X} \\ &= \sum_I G_{XI}(\mathbf{X})\ u(\mathbf{X}_I) - u_{,X} \end{aligned} \tag{2.59}$$

Substituting (2.58) into (2.59), we obtain

$$\begin{aligned} u^h_{,X}(\mathbf{X}) - u_{,X} &= u(\mathbf{X}) \sum_I G_{XI}(\mathbf{X}) + u_{,X}(\mathbf{X}) \left(\sum_I G_{XI}(\mathbf{X})(X_I - X) - 1 \right) \\ &+ u_{,Y}(\mathbf{X}) \sum_I G_{XI}(\mathbf{X})\ (Y_I - Y) \\ &+ 0.5\ u_{,XX}(\mathbf{X}) \sum_I G_{XI}(\mathbf{X})(X_I - X)^2 \\ &+ u_{,XY}(\mathbf{X}) \sum_I G_{XI}(\mathbf{X})(X_I - X)\ (Y_I - Y) \\ &+ 0.5\ u_{,YY}(\mathbf{X}) \sum_I G_{XI}(\mathbf{X})(Y_I - Y)^2 \end{aligned} \tag{2.60}$$

With the constant and linear reproducing conditions $\sum_I G_{XI} = 0$, $\sum_I G_{XI}(X_I - X) = 1$, $\sum_I G_{XI}(Y_I - Y) = 0$, eq. (2.60) can be simplified

$$\begin{aligned} u^h_{,X}(\mathbf{X}) - u_{,X} &= 0.5\ u_{,XX}(\mathbf{X}) \sum_I G_{XI}(\mathbf{X})(X_I - X)^2 \\ &+ u_{,XY}(\mathbf{X}) \sum_I G_{XI}(\mathbf{X})(X_I - X)\ (Y_I - Y) \\ &+ 0.5\ u_{,YY}(\mathbf{X}) \sum_I G_{XI}(\mathbf{X})(Y_I - Y)^2 \end{aligned} \tag{2.61}$$

From (2.61), we obtain

$$\begin{aligned} |u^h_{,X}(\mathbf{X}) - u_{,X}| &\leq 0.5\ |u_{,XX}(\mathbf{X})|\ |\sum_I G_{XI}(\mathbf{X})(X_I - X)^2| \\ &+ |u_{,XY}(\mathbf{X})|\ |\sum_I G_{XI}(\mathbf{X})(X_I - X)\ (Y_I - Y)| \\ &+ 0.5\ |u_{,YY}(\mathbf{X})|\ |\sum_I G_{XI}(\mathbf{X})(Y_I - Y)^2| \end{aligned} \tag{2.62}$$

Since the shape functions have compact support, there exists a constant d such that for any $\mathbf{X} = (X\ Y)$

$$|X_I - X| \leq d, \quad |Y_I - Y| \leq d \tag{2.63}$$

Then

$$|u^h_{,X}(\mathbf{X}) - u_{,X}| \leq (0.5\ |u_{,XX}(\mathbf{X})| + |u_{,XY}(\mathbf{X})| + 0.5|u_{,YY}(\mathbf{X})|)\ d^2 \\ |\sum_I G_{XI}(\mathbf{X})| \tag{2.64}$$

If we assume that G_{XI} satisfies

$$|G_{XI}| \leq \frac{C_1}{h_0} \tag{2.65}$$

then if the supports of the shape functions are chosen that the size of the support is proportional to the local refinement parameter h_0, i.e. $d = \tilde{d}h_0$, then

$$|u^h_{,X}(\mathbf{X}) - u_{,X}| \leq C \\ (0.5\ |u_{,XX}(\mathbf{X})| + |u_{,XY}(\mathbf{X})| + 0.5|u_{,YY}(\mathbf{X})|)\ h_0 \tag{2.66}$$

So the approximation error in the derivative is of order h for a corrected derivative approximation. Similar observations hold for the Y-derivative.

The Randles-Libersky correction

Randles and Libersky [7] developed a similar correction which they called normalization. To fulfill the first-order completeness, they modified the SPH approximation for the gradient of the function u with a matrix $\mathbf{B}$:

$$\nabla_0 u^h(\mathbf{X}, t) = \left(-\sum_{J \in \mathcal{S}} (u_J(t) - u_I(t))\ \nabla_0 W(\mathbf{X}_J - \mathbf{X}, h_0)\ V_J^0 \right) \cdot \mathbf{B}(\mathbf{X}) \tag{2.67}$$

with

$$\mathbf{B}(\mathbf{X}) = \left(-\sum_{J \in \mathcal{S}} (\mathbf{X}_J - \mathbf{X}) \otimes \nabla_0 W(\mathbf{X}_J - \mathbf{X}, h_0)\ V_J^0 \right)^{-1} \tag{2.68}$$

If the SPH shape functions $W(\mathbf{X} - \mathbf{X}_J, h)\ V_J^0$ are replaced by the Shepard functions, the expression for $\mathbf{B}$ becomes:

$$\mathbf{B}(\mathbf{X}) = \left(-\sum_{J \in \mathcal{S}} \mathbf{X}_J \otimes \nabla_0 W^S(\mathbf{X}_J - \mathbf{X}, h_0) \right)^{-1} \tag{2.69}$$

which is similar to the Krongauz-Belytschko correction; subtle differences arise from the symmetrization in (2.67) and (2.68). Note, that the SPH shape functions in equation (2.67) have to be replaced by the Shepard functions when using eq. (2.69) for the computation of $\mathbf{B}$. The approximation for the gradient of the function u is then formulated in the unsymmetrized form because the Shepard functions are zero-order complete by construction:

$$\nabla_0 u^h(\mathbf{X}, t) = \left(-\sum_{J \in \mathcal{S}} u_J(t)\ \nabla_0 W^S(\mathbf{X}_J - \mathbf{X}, h_0)\ V_J^0 \right) \cdot \mathbf{B}(\mathbf{X}) \tag{2.70}$$

Reproducing kernel particle method (RKPM)

The Reproducing kernel particle method (RKPM) [8] can be considered as an improvement of the continuous SPH approximation. In order to increase the order of completeness of the approximation, a correction function $C(\mathbf{X},\mathbf{Y})$ is introduced into the approximation:

$$u^h(\mathbf{X}) = \int_{\Omega_\mathbf{Y}} C(\mathbf{X},\mathbf{Y})W(\mathbf{X}-\mathbf{Y})u(\mathbf{Y})\mathrm{d}\Omega_\mathbf{Y} \tag{2.71}$$

with $K(\mathbf{X},\mathbf{Y}) = C(\mathbf{X},\mathbf{Y})W(\mathbf{X}-\mathbf{Y})$ and where $C(\mathbf{X},\mathbf{Y})$ is defined such that the approximation is n-th order complete.

$$u(\mathbf{X}) = \mathbf{p}^\mathrm{T}(\mathbf{X})\mathbf{a} \tag{2.72}$$

$$\mathbf{p}(\mathbf{X})u(\mathbf{X}) = \mathbf{p}(\mathbf{X})\mathbf{p}^\mathrm{T}(\mathbf{X})\mathbf{a} \tag{2.73}$$

$$\int_{\Omega_\mathbf{Y}} \mathbf{p}(\mathbf{Y})W(\mathbf{X}-\mathbf{Y})u(\mathbf{Y})\mathrm{d}\Omega_\mathbf{Y} = \int_{\Omega_\mathbf{Y}} \mathbf{p}(\mathbf{Y})\mathbf{p}^\mathrm{T}(\mathbf{Y})W(\mathbf{X}-\mathbf{Y})\mathrm{d}\Omega_\mathbf{Y}\mathbf{a} \tag{2.74}$$

This is a system of equation from which $\mathbf{a}$ is solved and substituted into the approximation $u^h(\mathbf{X}) = \mathbf{p}^\mathrm{T}(\mathbf{X})\mathbf{a}$, it yields

$$u^h(\mathbf{X}) = \mathbf{p}^\mathrm{T}(\mathbf{X})\left[\int_{\Omega_\mathbf{Y}} \mathbf{p}(\mathbf{Y})\mathbf{p}^\mathrm{T}(\mathbf{Y})W(\mathbf{X}-\mathbf{Y})\mathrm{d}\Omega_\mathbf{Y}\right]^{-1}\int_{\Omega_\mathbf{Y}} \mathbf{p}(\mathbf{Y})w(\mathbf{X}-\mathbf{Y})u(\mathbf{Y})\mathrm{d}\Omega_\mathbf{Y} \tag{2.75}$$

with the corrected function

$$\begin{aligned} C(\mathbf{X},\mathbf{Y}) &= \mathbf{p}^\mathrm{T}(\mathbf{X})\left[\int_{\Omega_\mathbf{Y}} \mathbf{p}(\mathbf{Y})\mathbf{p}^\mathrm{T}(\mathbf{Y})W(\mathbf{X}-\mathbf{Y})\mathrm{d}\Omega_\mathbf{Y}\right]^{-1}\mathbf{p}(\mathbf{Y}) \\ &= \mathbf{p}^\mathrm{T}(\mathbf{X})[\mathbf{M}(\mathbf{X})]^{-1}\mathbf{p}(\mathbf{Y}) \end{aligned} \tag{2.76}$$

To evaluate this continuous expression, numerical integration must be employed. This step leads from the reproducing kernel method to its discrete version, the reproducing kernel particle method [8].

$$\begin{aligned} u^h(\mathbf{X}) &= \int_{\Omega_\mathbf{Y}} C(\mathbf{X},\mathbf{Y})W(\mathbf{X}-\mathbf{Y})u(\mathbf{Y})\mathrm{d}\Omega_\mathbf{Y} \\ &= \sum_{I\in\mathcal{S}} C(\mathbf{X},\mathbf{X}_I)w(\mathbf{X}-\mathbf{Y}_I)u_I V_I^0 \\ &= \mathbf{p}^\mathrm{T}(\mathbf{X})[\mathbf{M}(\mathbf{X})]^{-1}\sum_{I\in\mathcal{S}} \mathbf{p}(\mathbf{X}_I)W(\mathbf{X}-\mathbf{X}_I)u_I V_I^0 \end{aligned} \tag{2.77}$$

$$\tag{2.78}$$

The moment matrix $\mathbf{M}(\mathbf{X})$ is also computed by numerical integration

$$\begin{aligned}\mathbf{M}(\mathbf{X}) &= \int_{\Omega_{\mathbf{Y}}} \mathbf{p}(\mathbf{Y})\mathbf{p}^{\mathrm{T}}(\mathbf{Y})W(\mathbf{X}-\mathbf{Y})\mathrm{d}\Omega_{\mathbf{Y}} \\ &= \sum_{I\in\mathcal{S}} \mathbf{p}(\mathbf{X}_I)\mathbf{p}^{\mathrm{T}}(\mathbf{X}_I)W(\mathbf{X}-\mathbf{X}_I)V_I^0 \end{aligned} \tag{2.79}$$

2.5.3 Element-free Galkerin method (EFG)

The EFG method employs a moving least square approximation that was originally developed for curve fitting. We will go one step back and first look at least-square fitting.

Least square approximation

For the sake of simplicity, we first present this method in one dimension. The method is then naturally extended to higher dimensions. Let us consider the data fitting problem where we want to find a function $u^h(x)$ fitting the data points (x_I, u_I) with $u_I = u(x_I)$. Assume that the approximation function $u^h(x)$ is a polynomial of order m:

$$u^h(x) = a_0 + a_1 x + a_2 x^2 + ... + a_m x^m \tag{2.80}$$

that can be written in compact form as

$$u^h(x) = \mathbf{p}^{\mathrm{T}}(x)\mathbf{a} \tag{2.81}$$

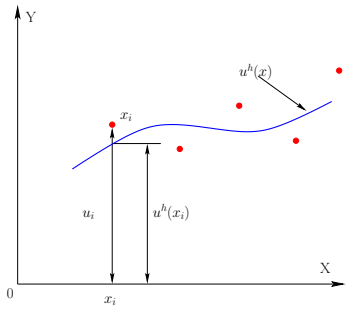

Figure 2.5: Data fitting using least square method

The parameters $\mathbf{a}$ can be determined by minimizing the square of difference between u_I and $u^h(x_I)$

$$\mathcal{J} = \sum_{I=1}^{n} [u^h(x_I) - u_I]^2 = \sum_{I=1}^{n} [\mathbf{p}^{\mathrm{T}}(x_I)\mathbf{a} - u_I]^2 \tag{2.82}$$

Taking derivatives with respect to $\mathbf{a}$ leads to the equation

$$\sum_{I=1}^{n} \mathbf{p}(x_I)\mathbf{p}^{\mathrm{T}}(x_I)\mathbf{a} = \sum_{I=1}^{n} \mathbf{p}(x_I)u_I \tag{2.83}$$

which allows us to solve for the unknowns $\mathbf{a}$. Then the approximation function $u^h(x)$ is completely defined.

Example Let us consider the data fitting example given in table 2.5.3.

x_I	1	2	3
u_I	1	1.5	4

Let us define a line approximating these points. In this case, we have

$$\mathbf{p}^{\mathrm{T}}(x) = [1 \quad x] \quad \mathbf{a}^{\mathrm{T}} = [a_0 \quad a_1] \tag{2.84}$$

Eq. (2.83) becomes

$$\sum_{I=1}^{3} \begin{bmatrix} 1 & x_I \\ x_I & x_I^2 \end{bmatrix} \mathbf{a} = \sum_{I=1}^{3} \begin{bmatrix} 1 \\ x_I \end{bmatrix} u_I \tag{2.85}$$

$$\begin{bmatrix} 3 & 6 \\ 6 & 14 \end{bmatrix} \mathbf{a} = \begin{bmatrix} 6.5 \\ 16 \end{bmatrix} \tag{2.86}$$

The solution is $a_0 = -5/6$ and $a_1 = 1.5$, hence the approximating line is given by

$$u^h(x) = -\frac{5}{6} + \frac{3}{2}x \tag{2.87}$$

It is clear that this way of approximation equals the role of all data points which often gives inaccurate results if some points are more *important* than others.

Moving least square approximation

In the moving least square (MLS) approximation, the unknown a will depend on the coordinates X or $\mathbf{X}$ when we consider higher order dimensions. The MLS-approximation fulfills the reproducing conditions by construction, so no corrections are needed. To satisfy the linear reproducing conditions, linear base functions $\mathbf{p}$ are chosen to be

$$\mathbf{p}(\mathbf{X}) = \begin{pmatrix} 1 & X & Y \end{pmatrix} \quad \forall \mathbf{X} \in \Re^2 \tag{2.88}$$

The MLS approximation is

$$u_h(\mathbf{X}, t) = \sum_{I=1}^{M} \mathbf{p}_I(\mathbf{X})\, \mathbf{a}_I(\mathbf{X}, t) = \mathbf{p}^T(X_i)\ \mathbf{a}(X_i) \tag{2.89}$$

where M determines the size of the polynomial basis and with $\mathbf{a}$ chosen to minimize the quadratic form

$$\begin{aligned} \mathcal{J}(\mathbf{a}(X_i)) &= \sum_{J=1}^{N} W(\mathbf{X}-\hat{\mathbf{X}}_J, h_0) \left(\sum_{I=1}^{M} \mathbf{p}_I(\hat{\mathbf{X}}_J)^T \, \mathbf{a}_I(\mathbf{X},t) - u(\hat{\mathbf{X}}_J) \right)^2 \\ &= \left[\mathbf{P}(\hat{\mathbf{X}}) \; \mathbf{a}(\mathbf{X}) - \mathbf{u}(\hat{\mathbf{X}}) \right]^T \; \mathbf{W}(\mathbf{X}) \; \left[\mathbf{P}(\hat{\mathbf{X}}) \; \mathbf{a}(\mathbf{X}) - \mathbf{u}(\hat{\mathbf{X}}) \right] \end{aligned} \tag{2.90}$$

where N denotes the number of neighbors where $W(\mathbf{X}) \neq 0$ and with

$$\mathbf{u}^T(\hat{\mathbf{X}}) = \Big(u(\hat{\mathbf{X}}_1) \; u(\hat{\mathbf{X}}_2) \; ... \; u(\hat{\mathbf{X}}_N) \Big)$$

$$\mathbf{P}(\hat{\mathbf{X}}) = \begin{pmatrix} p_1(\hat{\mathbf{X}}_1) & p_2(\hat{\mathbf{X}}_1) & ... & p_M(\hat{\mathbf{X}}_1) \\ p_1(\hat{\mathbf{X}}_2) & p_2(\hat{\mathbf{X}}_2) & ... & p_M(\hat{\mathbf{X}}_2) \\ \vdots & \vdots & \ddots & \vdots \\ p_1(\hat{\mathbf{X}}_N) & p_2(\hat{\mathbf{X}}_N) & ... & p_M(\hat{\mathbf{X}}_N) \end{pmatrix}$$

$$\mathbf{W}(\mathbf{X}) = \begin{pmatrix} W(\mathbf{X}-\hat{\mathbf{X}}_1) & 0 & ... & 0 \\ 0 & W(\mathbf{X}-\hat{\mathbf{X}}_2) & ... & 0 \\ \vdots & \vdots & \ddots & 0 \\ 0 & 0 & ... & W(\mathbf{X}-\hat{\mathbf{X}}_N) \end{pmatrix}$$

Minimizing equation (2.90) with respect to $\mathbf{a}$ leads to

$$\begin{aligned} \frac{\partial \mathcal{J}(\mathbf{a}(X_i))}{\partial \mathbf{a}(X_i)} &= -2\mathbf{P}^T(\hat{\mathbf{X}}) \; \mathbf{W}(\mathbf{X}) \; \mathbf{u}(\hat{\mathbf{X}}) \\ &+ \; 2\mathbf{P}^T(\hat{\mathbf{X}}) \; \mathbf{W}(\mathbf{X}) \; \mathbf{P}(\hat{\mathbf{X}}) \; \mathbf{a}(\hat{\mathbf{X}}) = 0 \end{aligned} \tag{2.91}$$

Bringing the left term on the RHS, we obtain

$$\mathbf{P}^T(\hat{\mathbf{X}}) \; \mathbf{W}(\mathbf{X}) \; \mathbf{u}(\hat{\mathbf{X}}) = \mathbf{P}^T(\hat{\mathbf{X}}) \; \mathbf{W}(\mathbf{X}) \; \mathbf{P}(\hat{\mathbf{X}}) \; \mathbf{a}(\hat{\mathbf{X}}) \tag{2.92}$$

and solving for $\mathbf{a}$ gives finally

$$\mathbf{a}(\mathbf{x}) = \underbrace{\mathbf{P}^T(\hat{\mathbf{X}}) \; \mathbf{W}(\mathbf{X}) \; \mathbf{P}^T(\hat{\mathbf{X}})}_{=\mathbf{A}\in R^{M\times M}} \; \underbrace{\mathbf{P}^T(\hat{\mathbf{X}}) \; \mathbf{W}(\mathbf{X})}_{=\mathbf{B}\in R^{M\times N}} \; \mathbf{u}(\hat{\mathbf{X}}) \tag{2.93}$$

With (2.89), we can write the approximation as

$$u^h(\mathbf{X},t) = \mathbf{p}^T(\mathbf{X}) \; \mathbf{A}^{-1}(\mathbf{X}) \; \mathbf{B}(\mathbf{X}) \; \mathbf{u}(\hat{\mathbf{X}}) \tag{2.94}$$

or in summation form

$$u^h(\mathbf{X},t) = \sum_{J=1}^{M} \sum_{K=1}^{M} \sum_{I=1}^{N} \mathbf{p}_J(\mathbf{X}) \; \mathbf{A}^{-1}_{JK}(\mathbf{X}) \; \mathbf{B}_{KI}(\mathbf{X}) \; \mathbf{u}_I(\hat{\mathbf{X}}) \tag{2.95}$$

where the meshfree shape functions $\Phi_I(\mathbf{X})$ are

$$\Phi_I(\mathbf{X},t) = \sum_{J=1}^{M}\sum_{K=1}^{M} \mathbf{p}_J(\mathbf{X})\ \mathbf{A}^{-1}_{JK}(\mathbf{X})\ \mathbf{B}_{KI}(\mathbf{X}) \tag{2.96}$$

Comparing the MLS approximation with the reproducing kernel particle method, eq. (2.77), we note that if V_I^0 in eq. (2.77) is equal to one, then both approximations are identical.

Example Let us illustrate the computation of the matrix

$$\mathbf{A}(\hat{\mathbf{X}}) = \begin{bmatrix} P_{11} & \dots & P_{1N} \\ \vdots & \ddots & \vdots \\ P_{M1} & \dots & P_{MN} \end{bmatrix} \begin{bmatrix} W_1 & \dots & 0 \\ \vdots & \ddots & \vdots \\ 0 & \dots & W_N \end{bmatrix} \begin{bmatrix} P_{11} & \dots & P_{M1} \\ \vdots & \ddots & \vdots \\ P_{1N} & \dots & P_{MN} \end{bmatrix}$$

for the case of $M = 1$, i.e. the polynomial basis $p(X) = 1$. Then we obtain

$$\mathbf{A}(\hat{\mathbf{X}}) = \begin{bmatrix} 1 & \dots & 1 \end{bmatrix} \begin{bmatrix} W_1 & \dots & 0 \\ \vdots & \ddots & \vdots \\ 0 & \dots & W_N \end{bmatrix} \begin{bmatrix} 1 \\ \vdots \\ 1 \end{bmatrix}$$

and the matrix $\mathbf{A}$ turns out to be a scalar value. It is easy to show that the shape function with the basis $p(x) = 1$, will lead to the shape function

$$\Phi_I(\mathbf{X}) = \frac{W_I(\mathbf{X})}{\sum\limits_{I\in\mathcal{S}} W_I(\mathbf{X})} \tag{2.97}$$

that is well known as Shepard function and was defined already in eq. (2.51).

Let us consider the case[4] of $M = 3$ with $p(\mathbf{X}) = [1\ X\ Y]^T$, then the matrix $\mathbf{A}$ is

$$\mathbf{A}(\hat{\mathbf{X}}) = \begin{bmatrix} 1 & \dots & 1 \\ x_1 & \dots & x_N \\ y_1 & \dots & y_N \end{bmatrix} \begin{bmatrix} W_1 & \dots & 0 \\ \vdots & \ddots & \vdots \\ 0 & \dots & W_N \end{bmatrix} \begin{bmatrix} 1 & x_1 & y_1 \\ \vdots & \vdots & \vdots \\ 1 & x_N & y_N \end{bmatrix}$$

The matrix $\mathbf{A}$ for this case is a 3×3 matrix. The higher the order of completeness, the higher will be the order of the matrix $\mathbf{A}$ and the higher is the computational cost to determine the MLS shape functions.

Conditioning of the A-matrix

For the computation of the MLS-shape function, the matrix $\mathbf{A}$ has to be inverted. Since the matrix $\mathbf{W}(\mathbf{X})$ is non-singular, it can be assumed that $\mathbf{A}$ is non-singular if $\mathbf{P}$ is non-singular. A necessary condition for a regular matrix $\mathbf{A}$ is that the number of neighbors N is larger than size of the polynomial basis M. For example, a linear complete basis in two dimension $p(\mathbf{X}) = [1\ X\ Y]$ requires at least three neighbor particles. For a linear complete polynomial basis and 3

[4] This corresponds to the two dimensional case with linear completeness

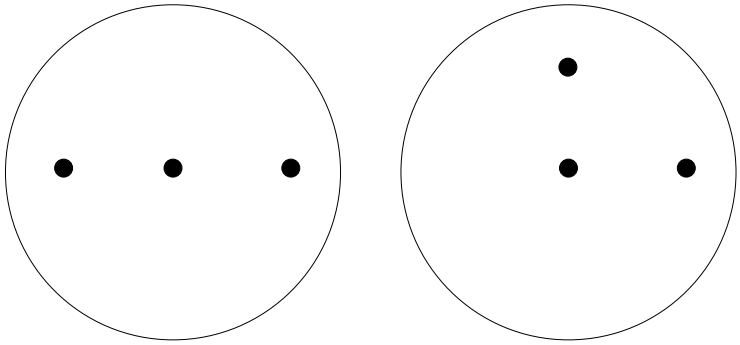

Figure 2.6: Particle arrangement for a linear complete MLS shape function in 2D: a) singular **A**-matrix, b) regular **A**-matrix

neighboring particles in two dimensions (see figure 2.6), it can be shown that the matrix **A** becomes singular when the particles are lying on a line. It can be shown that the matrix **A** is regular when the three nodes are located in different coordinate directions, see figure 2.6. This observation might be compared to finite elements where the accuracy of the solution is detoriated for distorted finite element shapes. The same observation is made in the extension to three dimensions and for higher order polynomial basis.

A measurement of the conditioning of a matrix is the condition number between the maximum and minimum eigenvalue of the matrix

$$\kappa = \frac{\lambda_{max}}{\lambda_{min}} \tag{2.98}$$

High values of κ indicate an ill-conditioned matrix. If $\kappa \to \infty$, then the matrix is singular. A shifting and centering of the shape function as will be described later improves the conditioning of **A**. Another opportunity to improve the conditioning of the matrix **A** is by Gram-Schmidt orthogonalization.

Spatial derivatives of the shape functions
The first derivatives of the MLS shape functions are obtained by simple differentiation

$$\begin{aligned} \frac{\partial \Phi(\mathbf{X})}{\partial X_i} &= \frac{\partial \mathbf{p}^T(\mathbf{X})}{\partial X_i}\mathbf{A}^{-1}\ \mathbf{B} + \mathbf{p}^T(\mathbf{X})\frac{\partial \mathbf{A}^{-1}(\mathbf{X})}{\partial X_i}\mathbf{B} \\ &+ \mathbf{p}^T(\mathbf{X})\ \mathbf{A}^{-1}(\mathbf{X})\frac{\partial \mathbf{B}(\mathbf{X})}{\partial X_i} \end{aligned} \tag{2.99}$$

with

$$\frac{\partial \mathbf{B}(\mathbf{X})}{\partial X_i} = \mathbf{P}(\hat{\mathbf{X}})\frac{\partial \mathbf{W}(\mathbf{X})}{\partial X_i} \tag{2.100}$$

To obtain the spatial partial derivatives of $\mathbf{A}^{-1}(\mathbf{X})$, let us consider

$$\mathbf{I} = \mathbf{A}^{-1}(\mathbf{X})\ \mathbf{A}(\mathbf{X}) \tag{2.101}$$

Taking spatial derivative of eq. (2.101) we obtain

$$\mathbf{0} = \frac{\partial \mathbf{A}^{-1}(\mathbf{X})}{\partial X_i}\ \mathbf{A}(\mathbf{X}) + \mathbf{A}^{-1}(\mathbf{X})\frac{\partial \mathbf{A}(\mathbf{X})}{\partial X_i} \tag{2.102}$$

Eq. (2.101) can be reformulated to

$$\begin{aligned} \frac{\partial \mathbf{A}^{-1}(\mathbf{X})}{\partial X_i} &= -\mathbf{A}^{-1}(\mathbf{X})\frac{\partial \mathbf{A}(\mathbf{X})}{\partial X_i}\mathbf{A}^{-1}(\mathbf{X}) \\ &= \mathbf{A}^{-1}(\mathbf{X})\ \mathbf{P}(\hat{\mathbf{X}})\frac{\partial \mathbf{W}(\mathbf{X})}{\partial X_i}\mathbf{P}^T(\hat{\mathbf{X}})\ \mathbf{A}^{-1}(\mathbf{X}) \end{aligned} \tag{2.103}$$

The second partial derivatives are then

$$\begin{aligned} \frac{\partial^2 \Phi(\mathbf{X})}{\partial X_i \partial X_j} &= \frac{\partial^2 \mathbf{p}^T(\mathbf{X})}{\partial X_i \partial X_j}\ \mathbf{A}^{-1}(\mathbf{X})\ \mathbf{B}(\mathbf{X}) \\ &+ 2\frac{\partial \mathbf{p}^T(\mathbf{X})}{\partial X_i}\left(\frac{\partial \mathbf{A}^{-1}(\mathbf{X})}{\partial X_j}\ \mathbf{B}(\mathbf{X}) + \mathbf{A}^{-1}(\mathbf{X})\frac{\partial \mathbf{B}(\mathbf{X})}{\partial X_i}\right) \\ &+ \mathbf{p}^T(\mathbf{X})\left(\frac{\partial^2 \mathbf{A}^{-1}(\mathbf{X})}{\partial X_i \partial X_j}\ \mathbf{B}(\mathbf{X}) + \mathbf{A}^{-1}(\mathbf{X})\ \frac{\partial^2 \mathbf{B}(\mathbf{X})}{\partial X_i \partial X_j} + \frac{\partial \mathbf{A}^{-1}(\mathbf{X})}{\partial X_i}\frac{\partial \mathbf{B}(\mathbf{X})}{\partial X_j}\right) \\ &+ \mathbf{p}^T(\mathbf{X})\left(\frac{\partial \mathbf{A}^{-1}(\mathbf{X})}{\partial X_j}\frac{\partial \mathbf{B}(\mathbf{X})}{\partial X_i}\right) \end{aligned} \tag{2.104}$$

Fast evaluation of the MLS shape functions

A fast evaluation procedure for the gradient of the shape function Φ_J can be derived by rewriting eq. (2.96):

$$\Phi_J(\mathbf{X}) = \boldsymbol{\gamma}(\mathbf{X}) \cdot \mathbf{p}(\mathbf{X}_J)\, W(\mathbf{X} - \mathbf{X}_J, h_0) \tag{2.105}$$

with

$$\mathbf{A}(\mathbf{X}) \cdot \boldsymbol{\gamma}(\mathbf{X}) = \mathbf{p}(\mathbf{X}_J) \tag{2.106}$$

such that the coefficients $\boldsymbol{\gamma}$ can be obtained by an LU decomposition and back-substitution that requires fewer computations than inverting the matrix $\mathbf{A}$. Then the derivatives of the shape functions can be written as

$$\nabla_0 \mathbf{A}(\mathbf{X}) \cdot \boldsymbol{\gamma}(\mathbf{X}) + \mathbf{A}(\mathbf{X}) \cdot \nabla_0 \boldsymbol{\gamma}(\mathbf{X}) = \nabla_0 \mathbf{p}(\mathbf{X}_J) \tag{2.107}$$

Rearranging this equation, $\nabla_0 \boldsymbol{\gamma}(\mathbf{X})$ is obtained. The evaluation of the derivatives of the shape functions requires little extra computer cost and, moreover, higher order derivatives can also be computed repeating the same process.

MLS centered and scaled approach

For computational purposes[5], it is usual and preferable to center in $\mathbf{X}_I$ and

[5] centering will improve the conditioning of the matrix $\mathbf{A}$

scale with h_0 also the polynomials involved in the definition of the meshfree approximation functions. Thus, the EFG shape functions will read:

$$\Phi_I(\mathbf{X}) = W(\mathbf{X}_I, \mathbf{X})\, \mathbf{P}^T \left(\frac{\mathbf{X}_I - \mathbf{X}}{h_0} \right)\, \boldsymbol{\gamma}(\mathbf{X}), \tag{2.108}$$

which is similar to (2.96). Recall also that typical expressions for the window function are of the following type: $W(\mathbf{Y}, \mathbf{X}) = W\left((\mathbf{Y} - \mathbf{X})/h_0\right)$. The consistency condition becomes in this case:

$$\mathbf{P}(0) = \sum_{I \in \mathcal{S}} \Phi_I(\mathbf{X})\, \mathbf{P} \left(\frac{\mathbf{X}_I - \mathbf{X}}{h_0} \right) \tag{2.109}$$

After substitution of (2.108) in (2.109) the linear system of equations that determines $\boldsymbol{\gamma}(\mathbf{X})$ is obtained:

$$\mathbf{A}(\mathbf{X})\, \boldsymbol{\gamma}(\mathbf{X}) = \mathbf{P}(0) \tag{2.110}$$

where

$$\mathbf{A}(\mathbf{X}) = \sum_{J \in \mathcal{S}} W(\mathbf{X}_J, \mathbf{X})\, \mathbf{P}^T \left(\frac{\mathbf{X}_J - \mathbf{X}}{h_0} \right)\, \mathbf{P} \left(\frac{\mathbf{X}_J - \mathbf{X}}{h_0} \right) \tag{2.111}$$

For a varying dilation parameter h_{0I}, h_{0I} associated to particle $\mathbf{X}_I$, is embedded in the definition of the weighting function:

$$W(\mathbf{X}_I, \mathbf{X}) = W \left(\frac{\mathbf{X}_I - \mathbf{X}}{h_{0I}} \right) \tag{2.112}$$

Note that a constant h_0 is employed in the scaling of the polynomials $\mathbf{P}$. The constant value h_0 is typically chosen as the mean value of all the h_{0J}. The consistency condition in this case is also (2.109). It also imposes the reproducibility of the polynomials in $\mathbf{P}$.

This centered expression for the EFG shape functions can also be obtained with a discrete MLS development with the discrete centered scalar product

$$< f, g >_{\mathbf{X}} = \sum_{J \in \mathcal{S}} W(\mathbf{X}_J, \mathbf{X})\, f \left(\frac{\mathbf{X}_J - \mathbf{X}}{h_0} \right)\, g \left(\frac{\mathbf{X}_J - \mathbf{X}}{h_0} \right) \tag{2.113}$$

The MLS development in this case is as follows: for fixed $\mathbf{X}$, and for $\mathbf{Z}$ near $\mathbf{X}$, u is approximated as

$$u(\mathbf{Z}) \simeq u^h(\mathbf{Z}, \mathbf{X}) = \mathbf{P}^T \left(\frac{\mathbf{Z} - \mathbf{X}}{h_0} \right)\, \mathbf{c}(\mathbf{X}) \tag{2.114}$$

where $\mathbf{c}$ is obtained, as usual, through a least-squares fitting with the discrete centered scalar product (2.113).

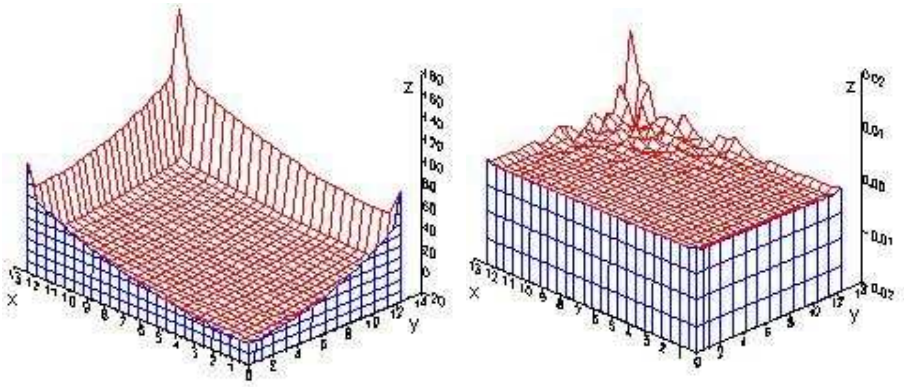

a) (b)

Figure 2.7: Absolute error of the quadratic function $F(X,Y) = X^2 + Y^2$ for the a) SPH approximation ($R = 0.8$), b) MLS approximation ($R = 0.3$); R denotes the support size of the shape function

2.5.4 Hp-clouds and PUFEM

While the approximations that were described previously are based on a so called intrinsic basis[6], the hp-cloud method [9] uses a so called extrinsic basis to increase the order of completeness:

$$u^h(\mathbf{X}) = \sum_{J \in \mathcal{S}} \Phi_J(\mathbf{X}) \left(u_J + \sum_{K=1}^{L} \mathbf{p}_K(\mathbf{X})\ a_{JK} \right) \tag{2.115}$$

where a_{JK} are additional degrees of freedom introduced in the variational formulation. In contrast to the hp-cloud method, the Partition of Unity Finite Element Method (PUFEM) uses generally finite element shape functions.

2.5.5 Generalized Finite Element Method (GFEM)

In GFEM [10] different shape functions are used for the "usual" part of the approximation and the extrinsically introduced additional degrees of freedom:

$$u^h(\mathbf{X}) = \sum_{J \in \mathcal{S}} \Phi_J(\mathbf{X})\ u_J + \sum_{J \in \mathcal{S}} \tilde{\Phi}_J(\mathbf{X}) \sum_{K=1}^{L} \mathbf{p}_K(\mathbf{X})\ a_{JK} \tag{2.116}$$

Note that GFEM, PUFEM as well as the hp-cloud method employ the partition of unity concept. The enrichment in these methods is usually employed in the entire domain. Therefore, these methods are often referred to as *global* partition of unity methods.

[6] The order of completeness is increased by a higher polynomial basis

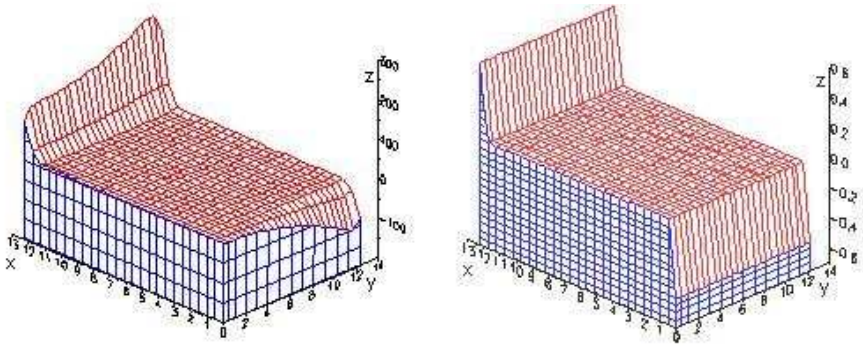

a) (b)

Figure 2.8: Absolute error of the derivative of the quadratic function $F(X,Y) = X^2 + Y^2$ for the a) SPH approximation ($R = 0.8$), b) MLS approximation ($R = 0.3$); R denotes the support size of the shape function

2.5.6 Examples

In this section, we will study the SPH-method, in usual and symmetrized form, and the linear MLS approximation with respect to their ability to approximate some given functions. A cubic B-spline with circular support is employed as weighting function. We will look at regular as well as irregular particle arrangements and restrict our studies to two dimensions.

Function approximation at regular particle arrangement

The function $F(X,Y) = X^2 + Y^2$
Consider a 25×25 regular particle arrangement with particle separation of 0.511. Figure 2.7 shows the absolute error of the MLS approximation and the SPH approximation where a support size R of $R = 0.6$ and $R = 1.6$ is chosen for the MLS and SPH approximation, respectively. Note that a support size of $R = 0.6$ corresponds to the minimum number of neighboring particles such that the matrix $\mathbf{A}$ in the MLS approximation just remains regular. Note also that the accuracy increases with increasing dilation parameter. i.e. support size. So, even with a small dilation parameter, the error does not exceed 0.05% for the MLS approximation while the error increases drastically with increasing X and Y coordinates for the SPH approximation. The highest errors occur at the boundary due to the lack of neighbor particles and at locations with high gradients.

The spatial derivatives of the function F in x-direction is $F_{,X} = 2X$. The absolute errors of the numerical approximation are shown in figure 2.8. The absolute error for the MLS approximation away from the boundary does not exceed 0.005%. Also the error of the "usual" SPH approximation is with a maximum error of 0.2% away from the boundary accurate. Inaccuracies occur

at the boundaries.

The function $F(X,Y) = \sin\left(X^2+Y^2\right)$
Let us consider a more complex function F within the interval $0 \leq X \leq \frac{\pi}{2}$, $0 \leq Y \leq \frac{\pi}{2}$. The partial derivatives[7] of the function F in x-direction is shown in figure 2.9a. The particle separation is set to $\sqrt{\pi/300}$ and the support size R is set as in the last example. We will look only at the approximation of the first derivatives since the derivatives are crucial in the applicatiion to partial differential equations (PDE). The absolute error of the numerical approximation is shown in figure 2.9b,c,d. The global absolute error of the MLS approximation is 0.01 while the error of the standard SPH approximation is 0.42. A symmetrization is able to decrease the error of the SPH approximation to a value of 0.12.

Finally, it can be concluded that the MLS approximation produces significantly better results than the SPH approximation. However, for complex functions, even the MLS approximation looses accuracy. The symmetrized SPH version is able to reduce the error significantly.

Error evolution for the SPH method in two dimensions

Let us consider the error evolution of the partial derivatives of a quadratic function in x-direction. Therefore, we will consider a regular particle arrangement. The particle volume is assumed to be $V = d^2$ where d is the particle separation. Furthermore, h is chosen such that only particle 2,4,6 and 8 are within the domain of influence of particle 5 (figure 2.10), the particle under consideration: $d < h < \sqrt{2}d$. The standard SPH approximation of the derivatives in x-direction of a function is given by:

$$u_{,X}(\mathbf{X}) = -\sum_{J=1}^{N} V_J W_{J,X}(\mathbf{X}) u_J \tag{2.117}$$

where the minus in front of the sum results from the integration by parts that is standard in SPH procedures. For particle 5, we obtain

$$u_{,X}(\mathbf{X}^{(5)}) = -V_J \left(W_{,X}^{(25)} u_2 + W_{,X}^{(45)} u_4 + W_{,X}^{(55)} u_5 + W_{,X}^{(65)} u_6 + W_{,X}^{(85)} u_8 \right) \tag{2.118}$$

Since the x-coordinate of particle 2,5 and 8 are identical, $W_{,X}^{(25)} = W_{,X}^{(55)} = W_{,X}^{(85)} = 0$. Due to the symmetry condition of the kernel, the indices in W^{IJ} can be exchanged that results in a change in the sign:

$$u_{,X}(\mathbf{X}^{(5)}) = V_J \left(W_{,X}^{(54)} u_4 + W_{,X}^{(56)} u_6 \right) \tag{2.119}$$

Error evolution for quadratic function
Let us consider the function $f(X) = aX^2 + bX + c$. Since Y is constant for particle 4 and 6, the argument in y-direction can be omitted. In figure 2.11, the

[7] $F_{,X} = 2X\,\cos\left(X^2+Y^2\right)$

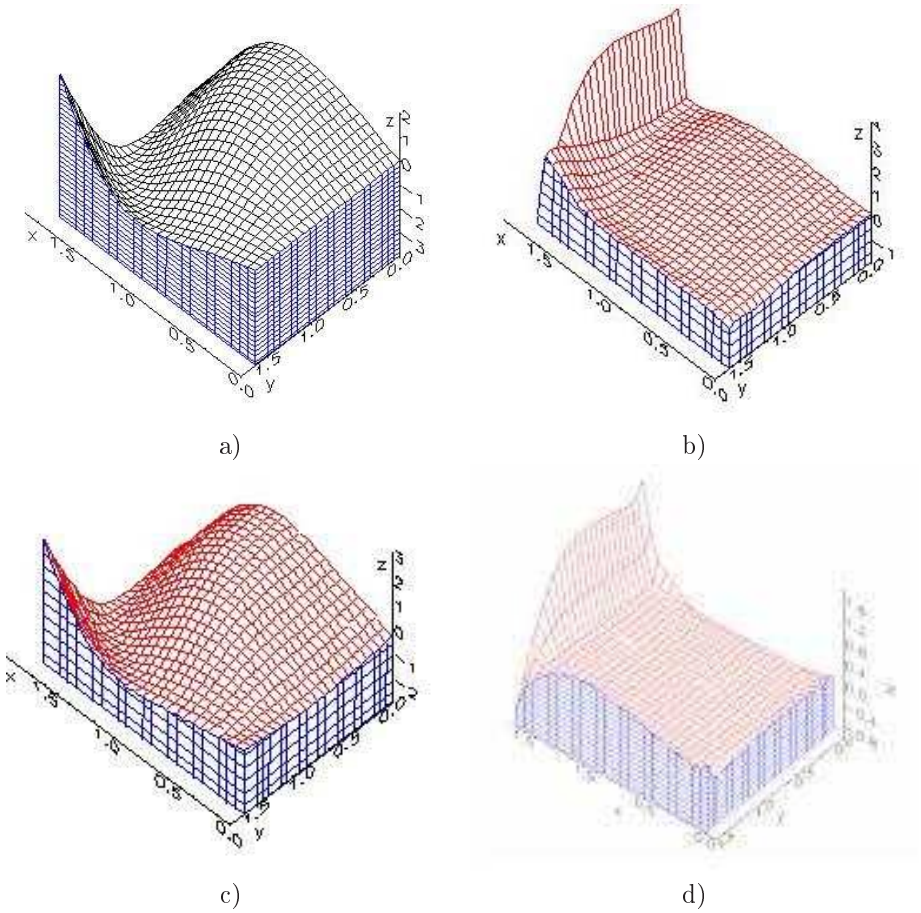

a) b)

c) d)

Figure 2.9: a) The derivative of the function $F(X,Y) = \sin\left(X^2+Y^2\right)$. b) Absolute error of the derivative of the sinus function $F(X,Y) = \sin\left(X^2+Y^2\right)$ for the MLS approximation ($R = 0.6$); b) Absolute error of the derivative of the sinus function $F(X,Y) = \sin\left(X^2+Y^2\right)$ for the SPH approximation ($R = 1.6$); Absolute error of the derivative of the sinus function $F(X,Y) = \sin\left(X^2+Y^2\right)$ for the symmetrized SPH approximation ($R = 1.6$)

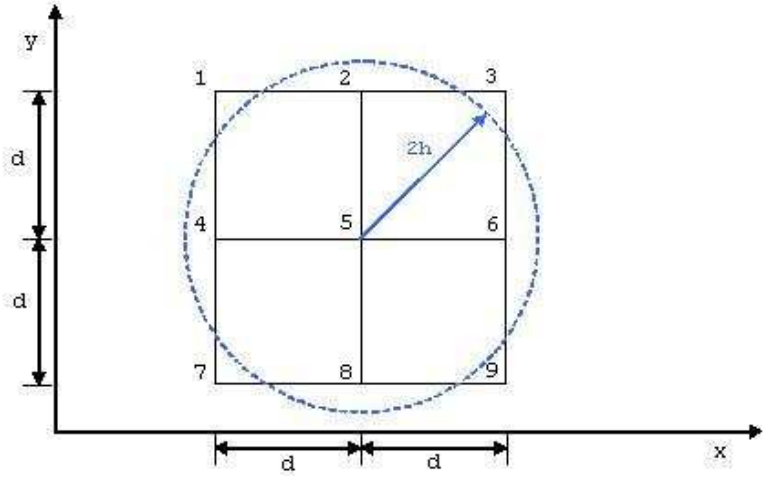

Figure 2.10: Regular particle arrangement

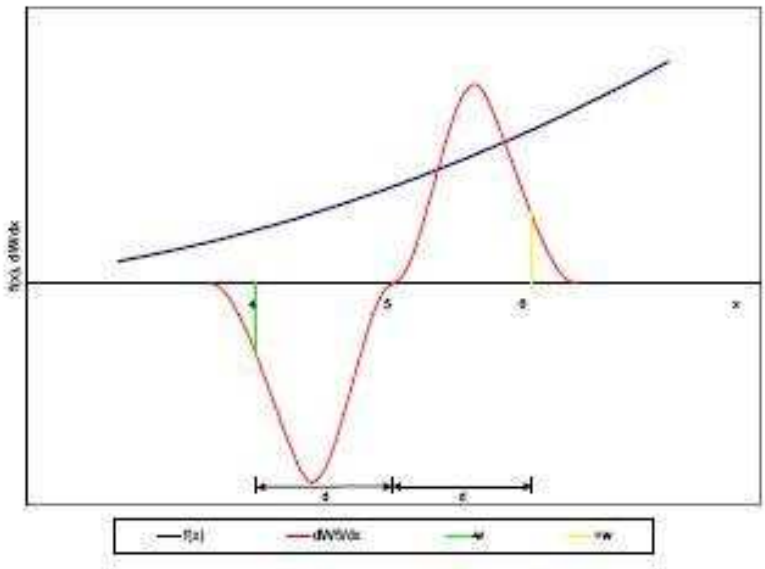

Figure 2.11: Graphical representation of the function $f(X) = aX^2 + bX + c$ and the value of the shape function of the particles 4 and 6 for this approximation

quadratic function f is shown in blue while the red curve shows the derivatives of the cubic B-spline of particle 5 in x-direction. The value w of the derivatives of the spline at the location of particle 4 and 6 are illustrated in green and yellow, respectively. Note that w is assumed to be always positive. With eq. (2.119), we can write now

$$\begin{aligned} f_{,X}(\mathbf{X}^{(5)}) &= V_J \left(W_{,X}^{(54)} f_4 + W_{,X}^{(56)} f_6 \right) \\ &= V_J \left[-w \left(a\ (x^{(4)})^2 + b x^{(4)} + c \right) + w \left(a\ (x^{(6)})^2 + b x^{(6)} + c \right) \right] \\ &= V_J\ w \left[a \left((x^{(5)} + d)^2 - (x^{(5)} - d)^2 \right) + b \left((x^{(5)} + d) - (x^{(5)} - d) \right) \right] \\ &= V_J\ w \left(4\ a\ d\ x^{(5)} + 2\ b\ d \right) \\ &= 2\ V_J\ w\ d \left(2\ a\ x^{(5)} + b \right) \end{aligned} \tag{2.120}$$

With the particle volume $V_J = d^2$, we obtain at least a linear function that should be obtained by differentiation of the function f:

$$f_{,X}(\mathbf{X}^{(I)}) = 2\ w\ d^3 \left(2\ a\ x^{(I)} + b \right) \tag{2.121}$$

While the parameters a and b are given by the function f, the parameter d and h can be varied[8]. The absolute error of the approximation can be given in terms of d, h and $x^{(I)}$

$$\begin{aligned} err_{abs}(d, h, x^{(I)}) &= 2\ a\ x^{(I)} + b - 2\ w(d,h)\ d^3 \left(2\ a\ x^{(I)} + b \right) \\ &= \left(2\ a\ x^{(I)} + b \right) \left(1 - 2\ w(d,h) d^3 \right) \end{aligned} \tag{2.122}$$

The relative error is obtained by scaling with the analytical solution:

$$\begin{aligned} err_{rel}(d, h, x^{(I)}) &= \frac{\left(2\ a\ x^{(I)} + b \right) \left(1 - 2\ w(d,h) d^3 \right)}{2\ a\ x^{(I)} + b} \\ &= 1 - 2\ w(d,h) d^3 \end{aligned} \tag{2.123}$$

To remove the error, the following condition holds:

$$1 - 2\ w(d,h) d^3 \equiv 0 \ \Leftrightarrow\ w(d,h)\ d^3 = 0.5 \tag{2.124}$$

It is easy to show that there does not exist any pair of (d, h) that fulfills the above condition. However, the best approximation is obtained for $d/h = \sqrt{2}$. The relative error is 35%. Increasing the dilation parameter significantly improves the results. With 28 neighoring particles, the error can be decreased to 0.2%. However, we omit an analytical consideration for that case.

Irregular particle arrangement

[8] Note that w in eq. (2.121) depends on d and h

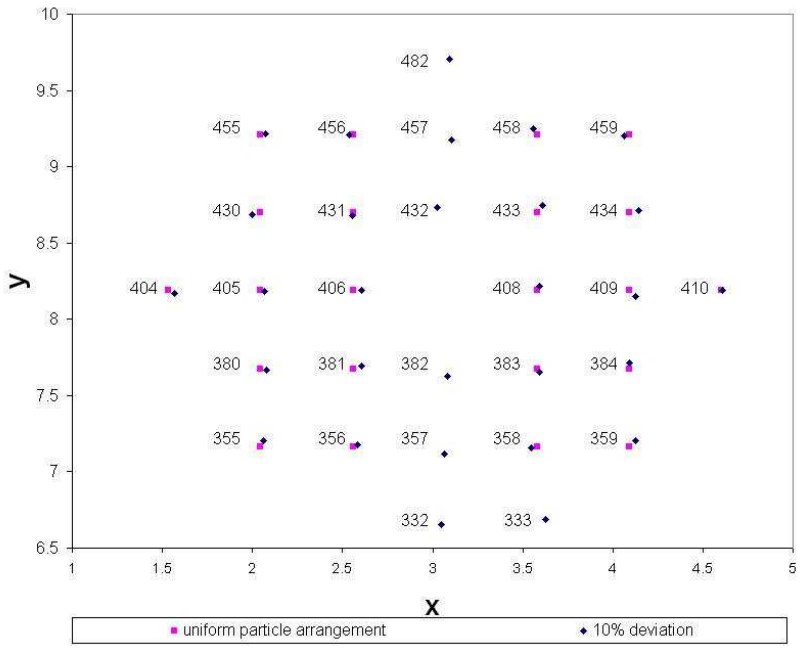

Figure 2.12: Regular and irregular particle arrangements around particle 407

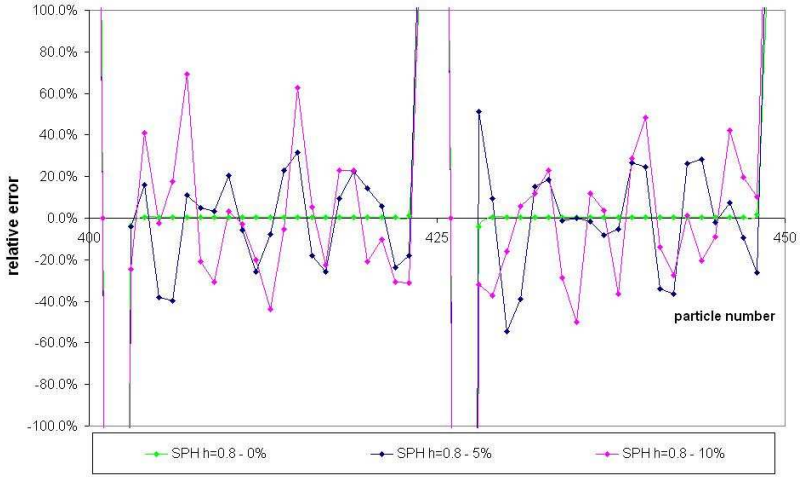

Figure 2.13: Relative error of the gradient of the quadratic function $F(X,Y) = X^2 + Y^2$ for the SPH method for regular and irregular particle arrangements ($R = 1.6$)

To realize an irregular particle arrangement, the boundary particles are kept on their original locations. The particles inside the domain were relocated randomly with a deviation of 5% and 10% from their original position. The outcome for one particle, that has the number 407, is shown in figure 2.12-the particles within its domain of influence are illustrated. For the 10% deviation, an additional particle (number 333) is within the domain of influence of particle 407. We will now consider again the quadratic function of section 2.5.6 and look at the error in the approximation of it's derivatives.

The error of the usual SPH approximation is shown in figure 2.13 for two layers of particles, from particle number 401 to 425 (first layer) and 426 to 450 (second layer). Recall that we used a $25 \times 25 = 625$ particle discretization that is numbered from 1 to 625. We note that the error is increased significantly with the irregularity of the particle discretization. One reason might be the insufficient assumption for the quadrature weights $V_J = d^2$. The error introduced by this assumption can be maximal 21% since $V_{new,J} = (1.1d)^2 = 1.21\ V_{old,J}$. However, since the approximation is based on a summation where the different values can have different signs (due to the value of the kernel function), it is difficult to study the error of the approximation of the partial derivatives in general. Therefore, let us consider one specific particle, number 407 (figure 2.12), that has a large relative error of around 70% (figure 2.13). Under the assumption of equivalent particle volumes we can reformulate the derivative approximation by

$$\frac{\nabla_0 u(\mathbf{X}^{(407)})}{V_I} \equiv -\sum_{J \in \mathcal{S}} \nabla_0 W_J^{(407)}(\mathbf{X})\ u_J \tag{2.125}$$

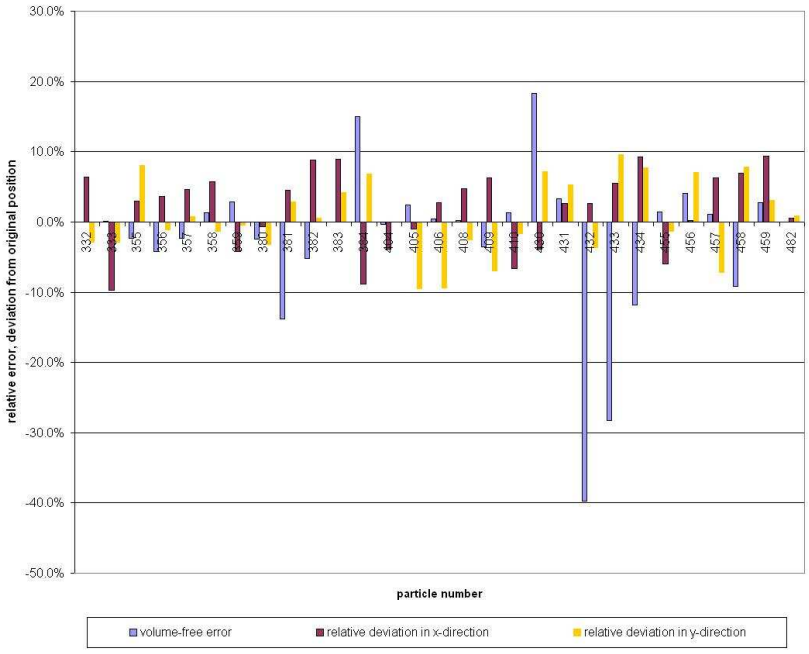

Figure 2.14: Volume-free relative error and particle deviations (deviation is 10%) from their original position

The "volume-free" relative error is then calculated by

$$\frac{\nabla_0 W_J^{(407)}(\mathbf{X})\ u_J}{\sum\limits_{K\in\mathcal{S}} \nabla_0 W_K^{(407)}(\mathbf{X})\ u_K} \tag{2.126}$$

In figure 2.14, all particles with the relative error $\frac{\partial W_J^{(407)}(\mathbf{X})}{\partial X}\ u_J \neq 0$ are shown for the volume-free relative error for the case of a 10% particle location deviation from the original configuration. The deviation from the original particle position is illustrated as well. As can be seen from that figure, the particle position deviation plays a minor role. The largest error occurs for particle number 432 with a relatively small deviation. Hence, the kernel approximation itself is mainly responsible for the inaccurate approximation. Note that the relative position of the neighboring particles with respect to the central particle, the particle of interest, is crucial in the kernel approximation.

The error of the symmetrized SPH approximation is shown in figure 2.15 for the 5% and 10% deviation. We note that the symmetrization drastically decreases the relative error. The relative error of the MLS approximation is by far smaller compared to the SPH approximation for an irregular particle arrangement, see figure 2.16.

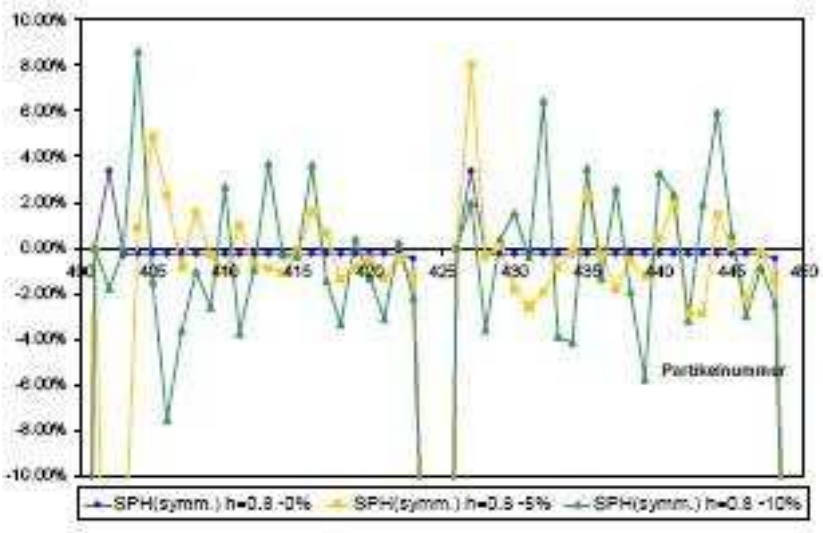

Figure 2.15: Relative error of the gradient of the quadratic function $F(X,Y) = X^2 + Y^2$ for the symmetrized SPH method for regular and irregular particle arrangements ($R = 1.6$)

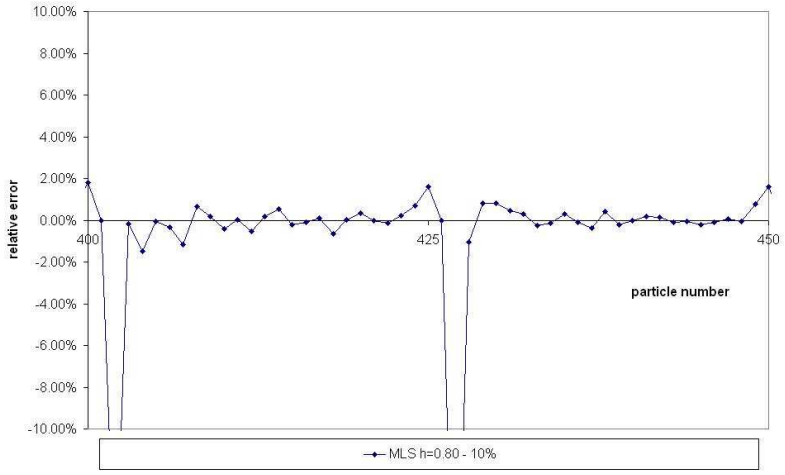

Figure 2.16: Relative error of the gradient of the quadratic function $F(X,Y) = X^2 + Y^2$ for the MLS method for an irregular particle arrangements ($R = 0.6$)

2.6 Governing equations

2.6.1 Statics

In statics, the governing equation is the equation of equilibrium given in the total Lagrangian description for small strains by

$$\nabla_0 \cdot \mathbf{P} - \mathbf{b} = \emptyset \quad \forall \mathbf{X} \in \Omega_0 \tag{2.127}$$

where $\mathbf{P}$ is the nominal stress tensor (note that $\mathbf{P}$ is the transpose of the first Piola Kirchhoff (1PK) tensor), $\mathbf{b}$ are the body forces, $\mathbf{X}$ are the material coordinates, ∇_0 is the gradient operator with respect to the material coordinates and Ω_0 is the domain of the body in the initial configuration. The boundary conditions are

$$\mathbf{u}(\mathbf{X}, t) = \bar{\mathbf{u}}(\mathbf{X}, t) \quad \text{on} \quad \Gamma_0^u \tag{2.128}$$

$$\mathbf{n}_0 \cdot \mathbf{P}(\mathbf{X}, t) = \bar{\mathbf{t}}_0(\mathbf{X}, t) \quad \text{on} \quad \Gamma_0^t \tag{2.129}$$

where $\bar{\mathbf{u}}$ and $\bar{\mathbf{t}}_0$ are the prescribed displacements and tractions, respectively and $\Gamma_0^u \bigcup \Gamma_0^t = \Gamma_0$, $(\Gamma_0^u \bigcap \Gamma_0^t) = \emptyset$.

2.6.2 Dynamics

Neglecting thermomechanical and frictional forces, the conservation equations in the total Lagrangian formulation are given by:

$$\varrho \; J = \varrho_0 \; J_0 \tag{2.130}$$

$$\ddot{\mathbf{u}} = \frac{1}{\varrho_0} \nabla_0 \cdot \mathbf{P} + \mathbf{b} \;\; \text{on} \;\; \Omega_0 \tag{2.131}$$

$$\dot{e} = \frac{1}{\varrho_0} \; \dot{\mathbf{F}} : \mathbf{P}^{\mathbf{T}} \tag{2.132}$$

where J and J_0 are the Jacobian determinant and initial Jacobian determinant, respectively, $\mathbf{u}$ is the displacement vector, ϱ_0 is the initial density, $\mathbf{P}$ are the nominal stresses, $\mathbf{b}$ are the body forces per mass unit, e is the internal energy, $\mathbf{F} = \nabla \mathbf{u} + \mathbf{I}$ denotes the deformation gradient where $\mathbf{I}$ is the second order identity tensor and a superimposed dot denotes material time derivatives. Note that the mass conservation equation is written in algebraic form since it is integrable for a Lagrangian description.

The boundary conditions are:

$$\mathbf{u}(\mathbf{X}, t) = \bar{\mathbf{u}}(\mathbf{X}, t) \quad \text{on} \quad \Gamma_0^u \tag{2.133}$$

$$\mathbf{n}_0 \cdot \mathbf{P}(\mathbf{X}, t) = \bar{\mathbf{t}}_0(\mathbf{X}, t) \quad \text{on} \quad \Gamma_0^t \tag{2.134}$$

where $\bar{\mathbf{u}}$ and $\bar{\mathbf{t}}_0$ are the prescribed displacement and traction, respectively, $\mathbf{n}_0$ is the outward normal to the domain and $\Gamma_0^u \cup \Gamma_0^t = \Gamma_0$, $(\Gamma_0^u \cap \Gamma_0^t) = \emptyset$.

2.6.3 From the strong form to the weak form

Let us consider at least $\mathcal{C}^0$ test and trial functions:

$$\delta\mathbf{u}^h(\mathbf{X}) = \sum_{J\in\mathcal{S}} \Phi_J(\mathbf{X})\ \delta\mathbf{u}_J \tag{2.135}$$

$$\mathbf{u}^h(\mathbf{X}) = \sum_{J\in\mathcal{S}} \Psi_J(\mathbf{X})\ \mathbf{u}_J \tag{2.136}$$

The test and trial functions belong to the following spaces:

$$\begin{aligned} \mathcal{V} &= \left\{\mathbf{u}(\cdot,t)|\mathbf{u}(\cdot,t)\in\mathcal{H}^1,\quad \mathbf{u}(\cdot,t)=\bar{\mathbf{u}}(t) \text{ on } \Gamma_0^u,\right\} \\ \mathcal{V}_0 &= \left\{\delta\mathbf{u}|\delta\mathbf{u}\in\mathcal{H}^1,\quad \delta\mathbf{u}=0 \text{ on } \Gamma_0^u,\right\} \end{aligned} \tag{2.137}$$

The weak from of the linear momentum equation is obtained by multiplying (2.131) with test functions:

$$\int_{\Omega_0} \nabla_0\cdot\mathbf{P}\cdot\delta\mathbf{u}\ d\Omega_0 + \int_{\Omega_0} \varrho_0\,(\mathbf{b}-\ddot{\mathbf{u}})\cdot\delta\mathbf{u}\ d\Omega_0 = 0 \tag{2.138}$$

The first term on the RHS of the momentum equation can be transformed by integration by parts

$$\int_{\Omega_0} \nabla_0\cdot\mathbf{P}\cdot\delta\mathbf{u}\ d\Omega_0 = \int_{\Omega_0} \nabla_0\cdot(\mathbf{P}\cdot\delta\mathbf{u})\ d\Omega_0 - \int_{\Omega_0} (\nabla_0\otimes\delta\mathbf{u})^T:\mathbf{P}\ d\Omega_0 \tag{2.139}$$

The Gauss theorem applied on the first term of the right hand side of (2.139) gives:

$$\int_{\Omega_0} \nabla_0\cdot(\mathbf{P}\cdot\delta\mathbf{u})\ d\Omega_0 = \int_{\Gamma_0^t} \mathbf{n}_0\cdot\mathbf{P}\cdot\delta\mathbf{u}\ d\Gamma_0 \tag{2.140}$$

With the relation between stress vector and stress tensor $\mathbf{t}=\mathbf{n}_0\cdot\mathbf{P}$ we obtain

$$\int_{\Omega_0} \nabla_0\cdot(\mathbf{P}\cdot\delta\mathbf{u})\ d\Omega_0 = \int_{\Gamma_0^t} \mathbf{t}\cdot\delta\mathbf{u}\ d\Gamma_0 \tag{2.141}$$

so that we finally obtain

$$\int_{\Omega_0} (\nabla_0\otimes\delta\mathbf{u})^T:\mathbf{P}\ d\Omega_0 - \int_{\Omega_0} \varrho_0\ \mathbf{b}\cdot\delta\mathbf{u}\ d\Omega_0 + \int_{\Gamma_0^t} \bar{\mathbf{t}}_0\cdot\delta\mathbf{u}\ d\Gamma_0 + \int_{\Omega_0} \varrho_0\ \delta\mathbf{u}\cdot\ddot{\mathbf{u}}\ d\Omega_0 = 0 \tag{2.142}$$

2.7 Construction of specific meshfree methods

Let us consider the weak form of the linear momentum equation[9], eq. (2.142). Substituting the test and trial functions into the linear momentum equation

[9] The equilibrium equation could be considered as well, for example

leads finally to the system of equations that we need to solve[10]:

$$\sum_J m_{IJ}\ \ddot{\mathbf{u}}_J = \mathbf{f}_I^{ext} - \mathbf{f}_I^{int}, \tag{2.143}$$

where $\mathbf{f}_I^{ext}$ and $\mathbf{f}_I^{int}$ are the external and the internal forces, given by

$$\mathbf{f}_I^{ext} = \int_{\Omega_0} \varrho_0\ \Phi_I\ \mathbf{b}\ d\Omega_0 + \int_{\Gamma_0^t} \Phi_I\ \bar{\mathbf{t}}\ d\Gamma_0 \tag{2.144}$$

$$\mathbf{f}_I^{int} = \int_{\Omega_0} \nabla_0 \Phi_I \cdot \mathbf{P}\ d\Omega_0 \tag{2.145}$$

and

$$m_{IJ} = \sum_{I \in S} \int_{\Omega_0} \varrho_0\ \Psi_I(\mathbf{X})\ \Phi_J(\mathbf{X})\ d\Omega_0. \tag{2.146}$$

The above mass matrix is the consistent mass matrix. To obtain the final discrete equations, the integrals above have to be evaluated by numerical integration, that will be discussed in the following sections. Depending on the choice of the shape function for the test and trial function, a large variety of meshfree methods can be constructed. For example, if we choose $\Phi_J(\mathbf{X}) = \delta(\mathbf{X} - \mathbf{X}_I)$, then we will obtain a collocation method that is closely related to a Galerkin method based on nodal integration. Differences occur only for the boundary integrals. If we choose $\Psi_J(\mathbf{X}) = \Phi_J(\mathbf{X})$, then we obtain a Bubnov Galerkin method. If $\Psi_J(\mathbf{X}) \neq \Phi_J(\mathbf{X})$, we will obtain a Petrov Galkerin method.

2.8 Spatial integration

2.8.1 Nodal integration

An efficient discretization in a Galerkin method is by nodal integration:

$$\int_{\Omega_0} f(\mathbf{X})\ d\Omega_0 = \sum_{J \in \mathcal{S}} f(\mathbf{X}_J)\ V_J^0 \tag{2.147}$$

where the weights V_J^0 represent tributary volumes associated with particle J. Note that we used nodal integration previously to obtain the discrete SPH and RKPM approximations in section 2.5.1 and 2.5.2. Applying this technique e.g. to the computation of the internal forces (2.145) gives:

$$\mathbf{f}_I^{int} = \sum_{J \in \mathcal{S}} V_J^0\ \nabla_0 \Phi_I(\mathbf{X}_J) \cdot \mathbf{P}_J \tag{2.148}$$

The nodal masses m_I are usually obtained by a Voronoi procedure, i.e. after placement of the nodes, a triangulation is performed and the intersections of the

[10] For more details, see e.g. Belytschko et al. [1]

perpendicular bisectors of the side on the triangles form the Voronoi cell[11], see also figure 2.19. The particle masses m_I are then computed just by multiplying the volume of the Voronoi cell V_J^0 with the density. Note that in general the physical mass m_I varies from the numerical mass m_{IJ}. However, it can be shown that the physical mass is recovered by diagonalizing the consistent mass matrix m_{IJ} with a standard row-sum technique:

$$\begin{aligned} m_I &= \sum_{J\in\mathcal{S}} m_{IJ} = \sum_{J\in\mathcal{S}} \int_{\Omega_0} \varrho_0 \; \Phi_I(\mathbf{X}) \; \Psi_J(\mathbf{X}) \; d\Omega_0 \\ &= \int_{\Omega_0} \varrho_0 \; \Phi_I(\mathbf{X}) \left(\sum_{J\in\mathcal{S}} \Psi_J(\mathbf{X}) \right) \; d\Omega_0 \end{aligned} \tag{2.149}$$

With an at least zero-order complete approximation, eq. (2.149) finally becomes

$$m_I = \int_{\Omega_0} \varrho_0 \; \Phi_I(\mathbf{X}) \; d\Omega_0 \tag{2.150}$$

After nodal integration we obtain

$$m_I = \sum_{J\in\mathcal{S}} \varrho_J \; \Phi_I(\mathbf{X}) \; V_J^0 \tag{2.151}$$

When the test functions are also at least zero-order complete, it is easy to verify that after adding up all lumped masses, the total physical mass M of the body is retained:

$$\sum_{I=1}^{N_{tot}} m_I = \sum_{I=1}^{N_{tot}} \sum_{J\in\mathcal{S}} \varrho_J \; \Phi_I(\mathbf{X}) \; V_J^0 = \sum_{J\in\mathcal{S}} \varrho_J \left(\sum_{I=1}^{N_{tot}} \Phi_I(\mathbf{X}) \right) V_J^0 = \sum_{J\in\mathcal{S}} \varrho_J \; V_J^0 = M \tag{2.152}$$

Crucial is also how to consider and discretize the 'real' geometric volume of a body. It can be discretized with particles arranged as in figure 2.17a where the particles are inside the volume. No particles lie on the boundaries of the body. The body can also be discretized as illustrated on figure 2.17b where particles are placed exactly on the boundaries. For figure 2.17a, all masses are equal. For the discretization in figure 2.17b, the boundary particles have only half of the mass of the interior particles for a Voronoi method. The masses of the particles at the corners are only a quarter of the masses of the interior particles. The boundary integrals for natural boundary conditions (external forces) (2.144) differ for the two models as shown in figure 2.17. When the particles are located directly on the boundary, the value of the shape function differs from when the particles are at a certain distance from the boundaries (see figure 2.17).

[11] Note that the volume of the Voronoi cell is the quadrature weight

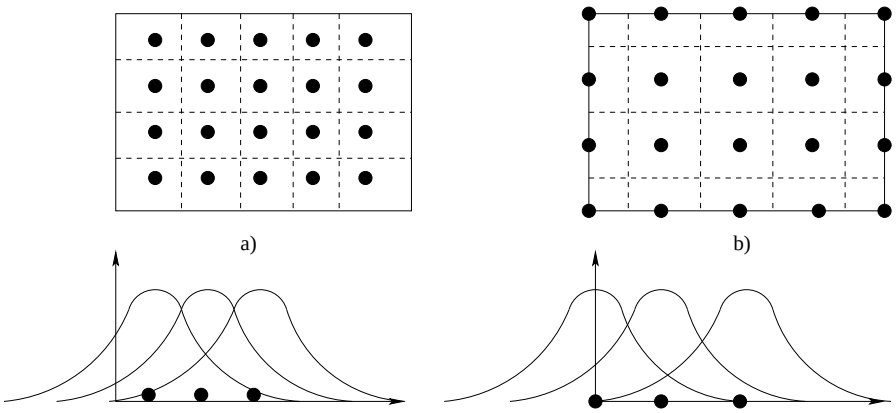

Figure 2.17: Value of the shape function for boundary particles lying directly on the boundaries or inside the boundaries

2.8.2 Stabilized nodal integration

Nodal integration often leads to instabilities due to rank deficiency and to low convergence rates. Chen et al. [11] showed that the vanishing derivatives of the meshfree shape functions at the particles are the cause of the instabilities. They notice that linear complete meshfree methods have to satisfy the following integration constraint

$$\int_{\Omega_0} \nabla \Phi_I(\mathbf{X})\ d\Omega_0 = \int_{\Gamma_0} \mathbf{n}_0 \Phi_I(\mathbf{X})\ d\Gamma_0 \tag{2.153}$$

This integration constraint comes from the equilibrium of the internal and external forces of the linear complete Galerkin approximation and is similar to the linear completeness in the constant stress patch test in finite elements. Chen et al. [11] propose a stabilized conforming nodal integration using strain smoothing. In the strain smoothing procedure, the nodal strains are computed as the divergence of a spatial average of the strain field. The strain smoothing avoids evaluating derivatives of the shape functions at the nodes and hence eliminates defective modes. The smooth strain field $\tilde{\boldsymbol{\epsilon}}$ at a material point $\mathbf{X}_M$ can be expressed as

$$\tilde{\boldsymbol{\epsilon}}(\mathbf{X}_M) = \int_{\Omega_0} \tilde{\boldsymbol{\epsilon}}\ \Psi(\mathbf{X} - \mathbf{X}_M)\ d\Omega_0 \tag{2.154}$$

where $\boldsymbol{\epsilon}$ is the strain from the compatibility condition ($\boldsymbol{\epsilon} = 0.5(u_{i,j} + u_{j,i})$), Ω_0 is the domain of the Voronoi cell and $\Psi(\mathbf{X} - \mathbf{X}_M)$ is the smoothing function that has to fulfill the following requirements:

$$\begin{aligned} \Psi(\mathbf{X} - \mathbf{X}_M) &\geq 0 \\ \int_{\Omega_0} \Psi(\mathbf{X} - \mathbf{X}_M)\ d\Omega_0 &= 1 \end{aligned} \tag{2.155}$$

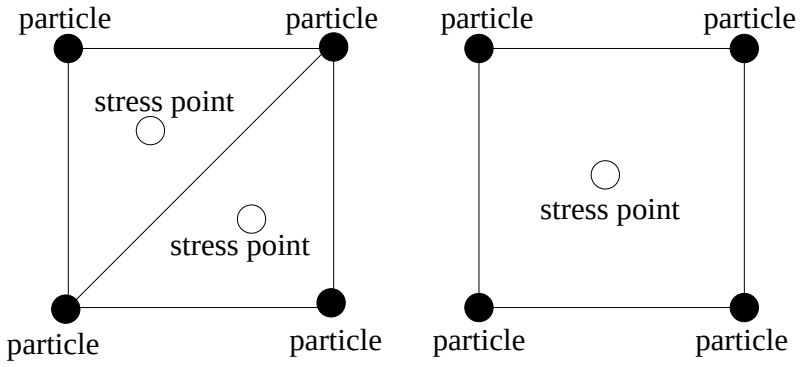

Figure 2.18: Arrangement of the stresspoints in two dimensions

Chen et al. [11] chose

$$\Psi(\mathbf{X}-\mathbf{X}_M) = \frac{1}{A_M} \quad \forall \mathbf{X}_M \in \Omega_0, \text{ otherwise } \Psi(\mathbf{X}-\mathbf{X}_M) = 0 \tag{2.156}$$

where A_M is the area of the smoothing (=Voronoi) cell. Substituting eq. (2.156) into (2.154), we obtain

$$\begin{aligned} \tilde{\boldsymbol{\epsilon}}(\mathbf{X}_M) &= \frac{1}{2A_M}\int_{\Omega_0} (u_{i,j}+u_{j,i})\ d\Omega_0 \\ &= \frac{1}{2A_M}\int_{\Gamma_0} (u_i\ n_j + u_j\ n_i)\ d\Gamma_0 \end{aligned} \tag{2.157}$$

As can be seen, integration is performed along a surface (the surface of the Voronoi cell) instead of a volume. It should be noted that the smoothed strain field does not satisfy the compatibility relations with the displacement field at all points in the discretized domain. However, the smooth, non-local strain and the local strain can be considered as two independent fields- the non-local strain field can be viewed as an assumed strain field. Thus, a two-field variational principle is suitable for this approximation.

2.8.3 Stress-point integration

Stress point integration was proposed by Dyka and Ingel [12] in one dimension to stabilize the SPH method. Randles and Libersky [13] extended stress point integration to higher dimensions to stabilize the normalized form of SPH. Stress point integration eliminates instabilities due to rank deficiency.
In stress point integration methods, stress points are interspersed between the particles and the contributions of the stresses are added to the integration of (2.147):

$$\int_{\Omega_0} f(\mathbf{X})\ d\Omega_0 = \sum_{J\in\mathcal{N}^P} f_J^P\ V_J^{0P} + \sum_{J\in\mathcal{N}^S} f_J^S\ V_J^{0S} \tag{2.158}$$

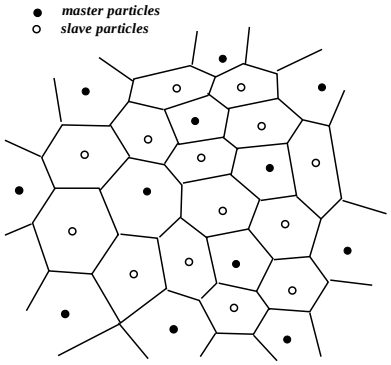

Figure 2.19: Scheme of stress point integration

where $\mathcal{N}_P$ and $\mathcal{N}_S$ indicate the supporting original particles and stress point nodes, respectively, to the original particle $\mathbf{X}_I^P$. There are different ways for arranging the stress points between the original particles. Some of them are shown in figure 2.18. Note that all kinematic values such as displacements and velocities are obtained via interpolation from the original particles:

$$\mathbf{u}_I^S = \sum_{J \in \mathcal{S}} \Phi_J(\mathbf{X}_I^S)\ \mathbf{u}_J^P, \qquad \mathbf{v}_I^S = \sum_{J \in \mathcal{S}} \Phi_J(\mathbf{X}_I^S)\ \mathbf{v}_J^P \tag{2.159}$$

where the superscripts S indicate stress points and the P the original particles. $\Phi_J(\mathbf{X}_I^S)$ is the shape function of the supporting master node J at $\mathbf{X}_I^S$. The internal forces for examples are calculated by

$$\mathbf{f}_I^{int} = \sum_{J \in \mathcal{N}_P} V_J^{0P}\ \nabla_0 \Phi_I(\mathbf{X}_J^P) \cdot \mathbf{P}_J^P + \sum_{J \in \mathcal{N}_S} V_J^{0S}\ \nabla_0 \Phi_I(\mathbf{X}_J^S) \cdot \mathbf{P}_J^S \tag{2.160}$$

The volumes V_J^{0P} and V_J^{0S} are computed from the Voronoi diagramm (see figure 2.19) so that their sums results in the total geometric initial volume:

$$V^0 = \sum_{J \in \mathcal{N}_P} V_J^{0P} + \sum_{J \in \mathcal{N}_S} V_J^{0S} \tag{2.161}$$

2.8.4 Gauss integration

There are two ways to construct a background mesh for the Gauss integration. The background mesh can be aligned with the particles as shown in figure 2.20a or the background mesh is not aligned with the particles as illustrated in figure 2.20b. In each integration cell, Gauss quadrature is performed. Note that in Gauss quadrature a polynomial of degree $2n_Q - 1$ can be exactly integrated with

n_Q quadrature points[12]. However, exact integration is difficult to perform in meshfree methods since meshfree shape functions are often not polynomial. It is common to increase the number of quadrature points to reduce integration errors. The number n_Q of Gauss points depends on the number of nodes in a cell. The number of Gauss points can be given by numerical experiments according to

$$n_Q = \sqrt{m} + 2 \tag{2.162}$$

where m denotes the number of nodes in one cell.

The integral of a function is given by

$$\int_{\Omega_0} f(\mathbf{X})\ d\Omega_0 = \int_{-1}^{+1}\int_{-1}^{+1} f(\xi,\eta)\ \ det\ \mathbf{J}^{\boldsymbol{\xi}}(\xi,\eta)\ d\xi d\eta = \sum_{J=1}^{m} w_J\ f(\boldsymbol{\xi}_{\boldsymbol{J}})\ det\ \mathbf{J}^{\boldsymbol{\xi}}(\boldsymbol{\xi}_{\boldsymbol{J}}) \tag{2.163}$$

where $\boldsymbol{\xi} = (\xi, \eta)$ are scaled local coordinates, m is the total number of quadrature points, $w_J = w(\xi_J)\ w(\eta_J)$ are the quadrature weights which is the product of the weight at the corresponding Gauss point in ξ- and η-direction and $det\ \mathbf{J}^{\boldsymbol{\xi}}$ is the Jacobian determinant given by

$$\mathbf{J}^{\boldsymbol{\xi}} = \frac{\partial \mathbf{X}}{\partial \boldsymbol{\xi}} \tag{2.164}$$

The internal forces are then

$$\mathbf{f}_{int} = \sum_{J=1}^{m} w_J\ det\mathbf{J}^{\boldsymbol{\xi}}(\boldsymbol{\xi}_J)\ \nabla_0\Phi(\mathbf{X}(\boldsymbol{\xi}_J) - \mathbf{X}_P)\ \mathbf{P}(\boldsymbol{\xi}_J) \tag{2.165}$$

where the superscript P indicates the particle position.

Example: The EFG-method for elastostatics

Let us consider a Bubnov-Galerkin method in a static setting with EFG-shape functions. Furthermore, we assume linear elastic material behavior, the hypothesis of small strains and no geometric non-linearities. Then we can write the equilibrium equation in variational formulation: find $\mathbf{u} \in \mathcal{V}$ such that

$$\delta W = \delta W_{int} - \delta W_{ext} = 0\ \ \forall \delta\mathbf{u} \in \mathcal{H}^1 \tag{2.166}$$

where

$$\delta W_{int} = \int_{\Omega_0} (\nabla \otimes \delta\mathbf{u})^T : \mathbf{P}\ d\Omega_0 \tag{2.167}$$

[12]Example: For a 2D quadrilateral finite element with bilinear shape functions, we have a maximum of quadratic terms for the shape functions plus linear terms for the Jacobian, i.e. maximum cubic terms; so we need $n_Q = 2$ quadrature points. An 8-node quadrilateral will require $n_Q = 3$ quadrature points since the highest polynomial is of order 5 (order 3 for the shape function and order 2 for the Jacobian)

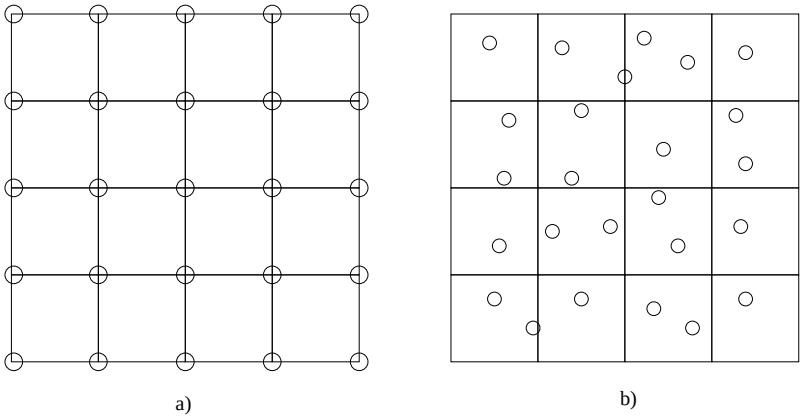

Figure 2.20: Different ways of cell integration

$$\delta W_{ext} = \int_{\Omega_0} \varrho_0 \ \delta \mathbf{u} \cdot \mathbf{b} \ d\Omega_0 + \int_{\Gamma_0^t} \delta \mathbf{u} \cdot \bar{\mathbf{t}}_0 \ d\Gamma_0 \tag{2.168}$$

where

$$\begin{aligned} \mathcal{V} &= \left\{ \mathbf{u}(\cdot,t) | \mathbf{u}(\cdot,t) \in \mathcal{H}^1, \ \ \mathbf{u}(\cdot,t) = \bar{\mathbf{u}}(t) \text{ on } \Gamma_0^u, \right\} \\ \mathcal{V}_0 &= \left\{ \delta\mathbf{u} | \delta\mathbf{u} \in \mathcal{H}^1, \ \delta\mathbf{u} = 0 \text{ on } \Gamma_0^u, \right\} \end{aligned} \tag{2.169}$$

After substituting the test and trial functions into eq. (2.166), the system of equations reads:

$$\mathbf{K} \ \mathbf{u} = \mathbf{f}^{ext} \tag{2.170}$$

where $\mathbf{K}$ is the stiffness matrix

$$\mathbf{K}_{IJ} = \int_{\Omega_0} \mathbf{B}_I \ \mathbf{C}^t \mathbf{B}_J \ d\Omega_0 \tag{2.171}$$

with the following $\mathbf{B}$-matrix (in two dimensions)

$$\mathbf{B}_I = \begin{bmatrix} \Phi_{I,X} & 0 \\ 0 & \Phi_{I,Y} \\ \Phi_{I,Y} & \Phi_{I,X} \end{bmatrix} \tag{2.172}$$

The external and body forces are given by

$$\mathbf{f}_I^{ext} = \int_{\Gamma_0^t} \Phi_I(\mathbf{X}) \ \mathbf{t}_0 \ d\Gamma_0 + \int_{\Omega_0} \Phi_I(\mathbf{X}) \ \mathbf{b} \ d\Omega_0 \tag{2.173}$$

Note that the test functions do not vanish at the boundaries and hence do not allow for $\mathcal{H}^1$ to be represented exactly. Hence, special techniques need to be introduced to handle essential boundary conditions.

2.9 Essential boundary conditions

2.9.1 Lagrange multiplier method

Essential boundary conditions can be imposed by means of Lagrange multiplier method. Therefore, we modify the variational formulation given in the last section: find $\mathbf{u} \in \mathcal{V}$ such that

$$\delta W = \delta W_{int} - \delta W_{ext} - \delta W_u = 0 \;\; \forall \delta \mathbf{u} \in \mathcal{H}^1 \tag{2.174}$$

where

$$\delta W_{int} = \int_{\Omega_0 \setminus \Gamma_0^c} (\nabla \otimes \delta \mathbf{u})^T : \mathbf{P} \; d\Omega_0 \tag{2.175}$$

$$\delta W_{ext} = \int_{\Omega_0 \setminus \Gamma_0^c} \varrho_0 \; \delta \mathbf{u} \cdot \mathbf{b} \; d\Omega_0 + \int_{\Gamma_0^t} \delta \mathbf{u} \cdot \bar{\mathbf{t}}_0 \; d\Gamma_0 \tag{2.176}$$

where

$$\begin{aligned} \mathcal{V} &= \left\{ \mathbf{u}(\cdot,t) | \mathbf{u}(\cdot,t) \in \mathcal{H}^1, \;\; \mathbf{u}(\cdot,t) = \bar{\mathbf{u}}(t) \text{ on } \Gamma_0^u, \right\} \\ \mathcal{V}_0 &= \left\{ \delta \mathbf{u} | \delta \mathbf{u} \in \mathcal{H}^1, \;\; \delta \mathbf{u} = 0 \text{ on } \Gamma_0^u, \right\} \end{aligned} \tag{2.177}$$

The term δW_u in eq. (2.174) is introduced for the imposition of Dirichlet boundary conditions. With the Lagrange multiplier method, δW_u reads:

$$\delta W_u = \int_{\Gamma_u^0} \delta \boldsymbol{\lambda} \cdot (\mathbf{u} - \bar{\mathbf{u}}) \, d\Gamma_0 + \int_{\Gamma_0} \delta \mathbf{u} \boldsymbol{\lambda} \; d\Gamma_0 \tag{2.178}$$

where $\boldsymbol{\lambda}$ are the Lagrange multipliers that can be considered as tractions across the boundaries. As for the approximation of the test and trial functions, there are several ways to discretize the Lagrange multiplier field:

$$\boldsymbol{\lambda} = \sum_{J \in \mathcal{S}} \Phi_J^L(\mathbf{X}) \; \boldsymbol{\lambda}_J \tag{2.179}$$

where $\Phi_J^L(\mathbf{X})$ are the approximation functions for the Lagrange multipliers that can be finite element shape functions, meshfree shape functions or Dirac Delta functions. The resulting discrete form reads then

$$\begin{bmatrix} \mathbf{K} & \mathbf{G} \\ \mathbf{G} & 0 \end{bmatrix} \begin{pmatrix} \mathbf{u} \\ \boldsymbol{\lambda} \end{pmatrix} = \begin{pmatrix} \mathbf{f}^{ext} \\ \mathbf{q} \end{pmatrix} \tag{2.180}$$

where $\mathbf{K} = \mathbf{K}_{IJ}$ is the stiffness matrix given above,

$$\mathbf{G}_{IK} = -\int_{\Gamma_u} \Phi_I(\mathbf{X}) \; \Phi_K^L(\mathbf{X}) \; \mathbf{S} \; d\Gamma \tag{2.181}$$

and

$$\mathbf{q}_K = -\int_{\Gamma_u} \Phi_K^L(\mathbf{X}) \; \mathbf{S} \; \bar{\mathbf{u}} \; d\Gamma \tag{2.182}$$

where $\mathbf{S}$ is a 2×2 matrix with S_{ij} equal to 1 for $j = i$ and 0 otherwise. The disadvantages of using Lagrange multipliers are:

- The dimension of the resulting system of equations is increased.
- The global matrix is no longer positive definite even if $\mathbf{K}$ is symmetric and semi-positive definite.
- The final discrete system and the weak form problem induce a saddle point problem which precludes an arbitrary choice of the interpolation/approximation space for $\mathbf{u}$ and $\boldsymbol{\lambda}$. The resolution of the multiplier field must be fine enough in order to obtain an acceptable solution, but the system of equations will be singular if the resolution of Lagrange multipliers field is too fine. In fact, the interpolation spaces for the Lagrange multiplier and the principal unknown $\mathbf{u}$ must verify an $inf - sup$ condtion, known as Babuska-Brezzi stability condition, in order to ensure the convergence of the approximation. While in finite elements, it is trivial to chose the approximation for the Lagrange multiplier to verify the Babuska-Brezzi condition, this choice is not trivial in meshfree methods.

Example
For simplicity, let us consider the following problem: find the minimum of the function Π with constrained conditions:

$$\Pi = 2a_1^2 - 2a_1a_2 + a_2^2 + 18a_1 + 6a_2 \tag{2.183}$$

with constraint

$$a_1 = a_2 \tag{2.184}$$

This problem is solved by introducing a Lagrange multiplier λ as new unknown

$$\begin{aligned} \overline{\Pi} &= \Pi + \lambda(a_1 - a_2) \\ &= 2a_1^2 - 2a_1a_2 + a_2^2 + 18a_1 + 6a_2 + \lambda(a_1 - a_2) \end{aligned} \tag{2.185}$$

Differentiation with respect to three unknowns a_i and λ gives:

$$\frac{\partial\overline{\Pi}}{\partial a_1} = 0 \quad \frac{\partial\overline{\Pi}}{\partial a_2} = 0 \quad \frac{\partial\overline{\Pi}}{\partial\lambda} = 0 \tag{2.186}$$

The solution of the above equations gives us values for a_1, a_2 and λ.

$$a_1 = a_2 = -12 \quad \lambda = 6$$

2.9.2 Penalty method

In the penalty method, a different δW_u is used as compared to the previous section:

$$\delta W_u = 0.5p \int_{\Gamma_u^0} \|\mathbf{u} - \bar{\mathbf{u}}\|^2 d\Gamma_0 \tag{2.187}$$

where p is the penalty parameter that has to be specified by the user. A high penalty number will lead to a more accurate solution since in the penalty method

the imposed boundary condition is not exact. However, a high penalty number also leads to an ill conditioned global stiffness matrix. The advantage of the penalty method is that the dimension of the resulting system of equations remains unchanged.

Another alternative is the augmented Lagrange method that combines the Lagrange multiplier and penalty method and will be discussed in section 2.10.3.

2.9.3 Transformation method

Let us consider the approximation:

$$u^h(\mathbf{x}) = \sum_{I=1}^{N} \Phi_I(\mathbf{x}_J)\hat{u}_I \tag{2.188}$$

where $u^h(\mathbf{x})$ is actually displacement at particle $\mathbf{x}_J$ whereas $\hat{u_I}$ are fictitious values since the meshfree shape functions do not satisfy the Kronecker delta property. With N particles in the entire domain, we have N equations that can be given in matrix form by

$$\mathbf{u} = \mathbf{D}\hat{\mathbf{u}} \tag{2.189}$$

Noting that the size of matrix $\mathbf{D}$ is $N \times N$. Since the essential boundary conditions are imposed over the true displacement not over the fictitious parameters $\hat{\mathbf{u}}$, it is natural to eliminate them by the relation $\hat{\mathbf{u}} = \mathbf{D}^{-1}\mathbf{u}$. Hence, we have the transformed approximation written in terms of true nodal displacement

$$u^h(\mathbf{x}) = \sum_{I=1}^{n} \Phi_I(\mathbf{x})\mathrm{D}_{IJ}^{-1} u_I \tag{2.190}$$

Now, the essential boundary conditions can be applied directly. However, this method requires the inversion of a matrix of size $N \times N$ which is computationally too expensive. Hence, let us consider separately the boundary nodes on Γ^u from the interior nodes. The number of interior particles is denoted by N_Ω and the number of particles on the essential boundary Γ^u as N_{Γ^u}. We can write the approximation as follows

$$u^h(\mathbf{x}) = \sum_{I=1}^{N_\Omega} \Phi_I(\mathbf{x}_J)\hat{u_I}^{\Omega} + \sum_{I=1}^{N_{\Gamma^u}} \Phi_I(\mathbf{x}_J)\hat{u_I}^{\Gamma^u} \tag{2.191}$$

Along Γ^u, the prescribed displacement is imposed by

$$u(\mathbf{x}_J) = g(\mathbf{x}_J), \quad J = 1, ..., N_{\Gamma^u} \tag{2.192}$$

which is rewritten in matrix form

$$\underbrace{\mathbf{D}^{\Omega}\hat{\mathbf{u}}^{\Omega}}_{(N_{\Gamma^u}\times N_\Omega)(N_\Omega\times 1)} + \underbrace{\mathbf{D}^{\Gamma^u}\hat{\mathbf{u}}^{\Gamma^u}}_{(N_{\Gamma^u}\times N_{\Gamma^u})(N_{\Gamma^u}\times 1)} = \underbrace{\mathbf{g}}_{(N_{\Gamma^u}\times 1)} \tag{2.193}$$

Eliminating $\hat{\mathbf{u}}^{\Gamma^u}$ from the above equation, we have

$$\hat{\mathbf{u}}^{\Gamma^u} = \left[\mathbf{D}^{\Gamma^u}\right]^{-1} (\mathbf{g} - \mathbf{D}^{\Omega}\hat{\mathbf{u}}^{\Omega}) \tag{2.194}$$

and get the transformed meshless approximation

$$u^h(\mathbf{x}) = \sum_{I=1}^{N_\Omega} \Phi_I(\mathbf{x}_J)\hat{u_I}^{\Omega} + \sum_{I=1}^{N_{\Gamma^u}} \Phi_I(\mathbf{x}_J)\left([\mathrm{D}_{IJ}^{\Gamma^u}]^{-1}(g_I - \mathrm{D}_{IJ}^{\Omega}\hat{u}_J^{\Omega})\right) \tag{2.195}$$

After rearranging, the final form of the new approximation reads

$$u^h(\mathbf{x}) = \sum_{i=I}^{N_\Omega}\left(\Phi_I(\mathbf{x}) - \Phi_I(\mathbf{x})[\mathrm{D}_{IJ}^{\Gamma^u}]^{-1}\mathrm{D}_{IJ}^{\Omega}\right)u_I + \sum_{I=1}^{N_{\Gamma^u}} \Phi_I(\mathbf{x})[\mathrm{D}_{IJ}^{\Gamma^u}]^{-1}g_J \tag{2.196}$$

2.10 Coupling to finite elements

2.10.1 Coupling via ramp functions

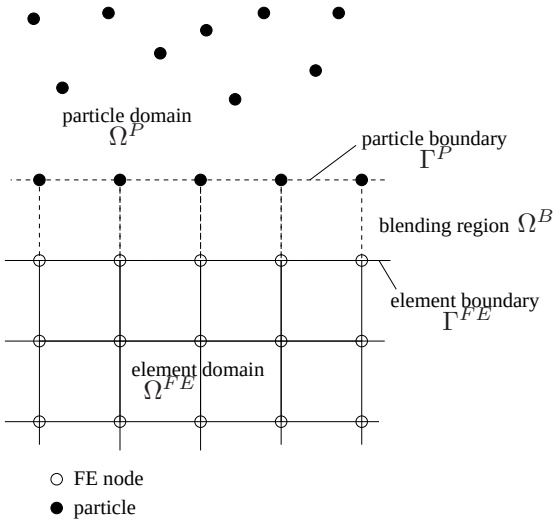

Figure 2.21: Coupling of Finite Elements and Particles via ramp functions

Consider a domain of problem with a hybrid discretization between finite elements and particles as illustrated in figure 2.21. The transition region is designates by Ω^B, Ω^P denotes the particle domain and Ω^{FE} is the element domain. The element and particle boundary is Γ^{FE} and Γ^P, respectively. In the interface region, an approximation is given by:

$$\mathbf{u}^h = \mathbf{u}^{FE}(\mathbf{X}) + R(\mathbf{X})\ \left(\mathbf{u}^P(\mathbf{X}) - \mathbf{u}^{FE}(\mathbf{X})\right)\quad,\quad \mathbf{X} \in \Omega_B \tag{2.197}$$

where $\mathbf{u}^{FE}$ and $\mathbf{u}^{P}$ are the finite element and particle approximations for $\mathbf{u}$ in the transition region and $R(\mathbf{X})$ is a ramp function, so that $R(\mathbf{X}) = 1, \mathbf{X} \in \Gamma^P$ and $R(\mathbf{X}) = 0, \mathbf{X} \in \Gamma^{FE}$. It is constructed with the use of a linear ramp function along the interface element boundaries so that continuity is ensured:

$$R(\mathbf{X}) = 3\ r^2(\mathbf{X}) - 2\ r^3(\mathbf{X}) \tag{2.198}$$

with

$$r(\mathbf{X}) = \sum_{J \in S_{\Gamma^P}} N_J(\mathbf{X}) \tag{2.199}$$

where S_{Γ^P} is the set of nodes on Γ^P. Substituting the FE approximations and the meshfree approximation into eq. (2.199) the approximation in the transition region is obtained:

$$\mathbf{u}^h(\mathbf{X}) = \sum_I \tilde{N}_I(\mathbf{X})\mathbf{u}_I \quad , \quad \mathbf{X}_I \in \Omega^B \tag{2.200}$$

with the interface shape function

$$\tilde{N}_I(\mathbf{X}) = (1 - R(\mathbf{X}))\ N_I(\xi(\mathbf{X})) + R(\mathbf{X})\ N_I(\mathbf{X}) \quad \mathbf{X} \in \Omega^B \tag{2.201}$$

$$\tilde{N}_I(\mathbf{X}) = R(\mathbf{X})\ N_I(\mathbf{X}) \quad \mathbf{X} \notin \Omega^B \tag{2.202}$$

Linear completeness is preserved in the entire domain. If the integrals for the particles are evaluated by a nodal integration with stress points, the shape functions in the blending domain have only to be evaluated at the particle boundary Γ^P and element boundary Γ^{FE} and are reduced to:

$$\tilde{N}_I(\mathbf{X}) = N_I(\mathbf{X}) \quad \mathbf{X} \in \Omega^B \text{ on } \Gamma^{FE} \tag{2.203}$$

$$\tilde{N}_I(\mathbf{X}) = 0 \quad \mathbf{X} \notin \Omega^B \text{ on } \Gamma^{FE} \tag{2.204}$$

$$\tilde{N}_I(\mathbf{X}) = N(\mathbf{X}) \quad \mathbf{X} \notin \Omega^B \text{ on } \Gamma^{P} \tag{2.205}$$

since $R(\mathbf{X}) = 1$ on Γ^P and $R(\mathbf{X}) = 0$ on Γ^{FE}. The approximation of the test functions in the blending region have the same structure.

2.10.2 Coupling with Lagrange multipliers

The particle and finite element domain can also be coupled by use of Lagrange multipliers. For the static case, the potential to be minimized is

$$W = W^{int} - W^{ext} + \boldsymbol{\lambda}^T\ \mathbf{g} \tag{2.206}$$

where W^{int} is the internal and W^{ext} is the external energy. The last term on the RHS are the constraints. The Lagrange multipliers are denoted by $\boldsymbol{\lambda}$ and

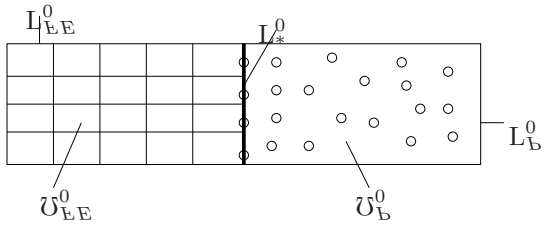

Figure 2.22: Coupling of particle and finite elements

$\mathbf{g} = \mathbf{u}^{FE} - \mathbf{u}^P$ is the gap of the particle and the finite element domain along the common boundary as illustrated in figure 2.22. The Lagrange multipliers are located at the particle positions and are

$$\mathbf{g}_h = \sum_{J=1}^{N} N_J^{FE}(\mathbf{X},t)\ \mathbf{u}_J^{FE} - \sum_{J\in S} N_J^P(\mathbf{X},t)\ \mathbf{u}_J^P \tag{2.207}$$

The Lagrange multiplier estimates are placed at the particle position and finite element shape functions are used to discretize the Lagrange multiplier field $\delta\boldsymbol{\lambda}$:

$$\delta\boldsymbol{\lambda}_h^P(\mathbf{X},t) = \sum_{J=1}^{N} N_J^{FE}(\mathbf{X},t)\ \delta\boldsymbol{\Lambda}_J(t) \tag{2.208}$$

Note that for the interpolation in eq. (2.208), the position of the Lagrange multipliers in the local element coordinate system[13] has to be known. If the global position $\mathbf{X}^L$ of the Lagrange multiplier is known then the local position can simply be obtained by solving $\mathbf{X}^L = \Phi_I(\boldsymbol{\xi})\mathbf{X}_I$ with respect to the local coordinates $\boldsymbol{\xi}$. The test and trial functions are

$$\delta\mathbf{u}_h(\mathbf{X},t) = \sum_{J=1}^{N} N_J^{FE}(\mathbf{X},t)\ \delta\mathbf{u}_J^{FE}(t) + \sum_{J\in\mathcal{S}} N_J^P(\mathbf{X},t)\ \delta\mathbf{u}_J^P(t) \tag{2.209}$$

$$\mathbf{u}_h(\mathbf{X},t) = \sum_{J=1}^{N} N_J^{FE}(\mathbf{X},t)\ \mathbf{u}_J^{FE}(t) + \sum_{J\in\mathcal{S}} N_J^P(\mathbf{X},t)\ \mathbf{u}_J^P(t) \tag{2.210}$$

and

$$\begin{aligned} N^{FE}(\mathbf{X},t) &= 0\ \forall\ \mathbf{X}\in\Omega_0^P \\ N^P(\mathbf{X},t) &= 0\ \forall\ \mathbf{X}\in\Omega_0^{FE} \end{aligned} \tag{2.211}$$

where $\mathcal{S}$ is the set of nodes in the particle model. Minimizing eq. (2.206) with respect to $\mathbf{u}$ and $\boldsymbol{\lambda}$ leads to the following equations:

$$\begin{aligned} \frac{\partial W}{\partial \mathbf{u}} = \frac{\partial W^{int}}{\partial \mathbf{u}} - \frac{\partial W^{ext}}{\partial \mathbf{u}} + \boldsymbol{\lambda}\,\frac{\partial \mathbf{g}}{\partial \mathbf{u}} = \mathbf{f}^{int} - \mathbf{f}^{ext} + \boldsymbol{\lambda}\,\frac{\partial \mathbf{g}}{\partial \mathbf{u}} = 0 \\ \frac{\partial W}{\partial \boldsymbol{\lambda}} = \mathbf{g} = 0 \end{aligned} \tag{2.212}$$

[13] on the boundary

The derivatives of W^{int} and W^{ext} with respect to $\mathbf{u}$ are the internal and external forces, respectively:

$$\mathbf{f}^{int} = \int_{\Omega_0^P \cup \Omega_0^{FE}} (\nabla_0 \otimes \delta\mathbf{u})^T : \mathbf{P} \; d\Omega_0 \tag{2.213}$$

$$\mathbf{f}^{ext} = \int_{\Omega_0^P \cup \Omega_0^{FE}} \delta\mathbf{u} \cdot \mathbf{b} \; d\Omega_0 + \int_{\Gamma_0^{P,t} \cup \Gamma_0^{FE,t}} \delta\mathbf{u} \cdot \bar{\mathbf{t}}_0 \; d\Gamma_0 \tag{2.214}$$

The additional forces $\boldsymbol{\lambda} \frac{\partial \mathbf{g}}{\partial \mathbf{u}}$ are linear combinations of the Lagrange multipliers. To obtain the discrete system of nonlinear equations we will do a linearization. Therefore, we take a Taylor series expansion of eq. (2.212) neglecting any higher order terms:

$$\begin{aligned} 0 &= \mathbf{f}^{int} - \mathbf{f}^{ext} + \boldsymbol{\lambda}\frac{\partial \mathbf{g}}{\partial \mathbf{u}} + \frac{\partial \mathbf{f}^{int}}{\partial \mathbf{u}} \; \Delta\mathbf{u} - \frac{\partial \mathbf{f}^{ext}}{\partial \mathbf{u}} \; \Delta\mathbf{u} + \frac{\partial \mathbf{g}}{\partial \mathbf{u}} \; \Delta\boldsymbol{\lambda} + \boldsymbol{\lambda}\frac{\partial^2 \mathbf{g}}{\partial \mathbf{u}\partial \mathbf{u}} \; \Delta\mathbf{u} \\ 0 &= \mathbf{u} + \frac{\partial \mathbf{g}}{\partial \mathbf{u}} \; \Delta\mathbf{u} \end{aligned} \tag{2.215}$$

Substituting the test and trial functions into (2.215) we finally obtain the following system of equations:

$$\begin{aligned} &\begin{bmatrix} \mathbf{K}^{FE} + \boldsymbol{\lambda}\frac{\partial^2 \mathbf{g}}{\partial \mathbf{u}\partial \mathbf{u}} & 0 & \left(\mathbf{K}^{FE-FE}\right)^T \\ 0 & \mathbf{K}^P + \boldsymbol{\lambda}\frac{\partial^2 \mathbf{g}}{\partial \mathbf{u}\partial \mathbf{u}} & \left(\mathbf{K}^{FE-P}\right)^T \\ \mathbf{K}^{FE-FE} & \left(\mathbf{K}^{FE-P}\right)^T & 0 \end{bmatrix} \cdot \begin{bmatrix} \Delta\mathbf{u}_J^{FE} \\ \Delta\mathbf{u}_J^P \\ \Delta\boldsymbol{\Lambda} \end{bmatrix} \\ &\qquad = \begin{bmatrix} \mathbf{f}^{ext,FE} - \mathbf{f}^{int,FE} - \boldsymbol{\lambda}^T \; \mathbf{K}^{FE-FE} \\ \mathbf{f}^{ext,P} - \mathbf{f}^{int,P} - \boldsymbol{\lambda}^T \; \mathbf{K}^{FE-P} \\ -\mathbf{g} \end{bmatrix} \end{aligned} \tag{2.216}$$

where $\mathbf{K}^{FE-FE}$ and $\mathbf{K}^{FE-P}$ denotes the derivatives of $\mathbf{g}$ with respect to $\mathbf{u}$ for the finite element ($\mathbf{u}^{FE}$) and particle domain ($\mathbf{u}^P$), respectively and $\mathbf{K}^{FE}$ and $\mathbf{K}^P$ are the derivatives of the internal and external forces with respect to $\mathbf{u}$. If neither $\mathbf{b}$ nor the traction boundary conditions $\bar{\mathbf{t}}$ depend on $\mathbf{u}$, then we can give the matrices:

$$\begin{aligned} \mathbf{K}^{FE-FE} &= \int_{\Gamma_0^*} \left(\mathbf{N}^{FE}\right)^T \cdot \mathbf{N}^{FE} \; d\Gamma_0 \\ \mathbf{K}^{FE-P} &= -\int_{\Gamma_0^*} \left(\mathbf{N}^{FE}\right)^T \cdot \mathbf{N}^P \; d\Gamma_0 \\ \mathbf{K}^P &= \int_{\Omega_0^P} \left(\mathbf{B}^P\right)^T \; \mathbf{C} \; \mathbf{B}^P \; d\Omega_0 \\ \mathbf{K}^{FE} &= \int_{\Omega_0^{FE}} \left(\mathbf{B}^{FE}\right)^T \; \mathbf{C} \; \mathbf{B}^{FE} \; d\Omega_0 \end{aligned} \tag{2.217}$$

and the vectors for internal and external forces

$$\begin{aligned}
\mathbf{f}^{ext,FE} &= \int_{\Omega_0^{FE}} \left(\mathbf{N}^{FE}\right)^T \mathbf{b}\, d\Omega_0 + \int_{\Gamma_0^{FE,t}} \left(\mathbf{N}^{FE}\right)^T \bar{\mathbf{t}}_0\, d\Gamma_0 \\
\mathbf{f}^{ext,P} &= \int_{\Omega_0^{P}} \left(\mathbf{N}^{P}\right)^T \mathbf{b}\, d\Omega_0 + \int_{\Gamma_0^{P,t}} \left(\mathbf{N}^{P}\right)^T \bar{\mathbf{t}}_0\, d\Gamma_0 \\
\mathbf{f}^{int,FE} &= \int_{\Omega_0^{FE}} \left(\mathbf{B}^{FE}\right)^T \cdot \mathbf{P}\, d\Omega_0 \\
\mathbf{f}^{int,P} &= \int_{\Omega_0^{P}} \left(\mathbf{B}^{P}\right)^T \cdot \mathbf{P}\, d\Omega_0
\end{aligned} \tag{2.218}$$

For a linear problem in elastostatics, we have a linear stiffness matrix $\mathbf{K}$, the starting value is zero, i.e. $\Delta\mathbf{u} = \mathbf{u}$ and $\Delta\boldsymbol{\lambda} = \boldsymbol{\lambda}$ and the term $\frac{\partial^2 \mathbf{g}}{\partial \mathbf{u} \partial \mathbf{u}}$ vanishes for linear constraint. Hence we obtain the well-known discrete equations for a linear problem in elastostatics:

$$\begin{bmatrix} \mathbf{K}^{FE} & 0 & \left(\mathbf{K}^{FE-FE}\right)^T \\ 0 & \mathbf{K}^{P} & \left(\mathbf{K}^{FE-P}\right)^T \\ \mathbf{K}^{FE-FE} & \left(\mathbf{K}^{FE-P}\right)^T & 0 \end{bmatrix} \cdot \begin{bmatrix} \mathbf{u}_J^{FE} \\ \mathbf{u}_J^{P} \\ \boldsymbol{\Lambda} \end{bmatrix} = \begin{bmatrix} \mathbf{f}^{ext,FE} \\ \mathbf{f}^{ext,P} \\ -\mathbf{g} \end{bmatrix} \tag{2.219}$$

2.10.3 Bridging domain coupling method

We denote the complete domain in the initial configuration by Ω_0 and its boundaries by Γ_0 ; Γ_0 consists of traction boundaries Γ_0^t and the displacement boundaries Γ_0^u. The domains are subdivided into the subdomains treated by finite element methods, Ω_0^{FE}, and that treated by particle methods, Ω_0^P; the latter is the domain encompassed by the particles of the model. The intersection of these two domains is denoted by Ω_0^{int} in the initial configuration, Ω^{int} in the current configuration; $\Omega^{int}$is often called the overlapping subdomain (or bridging domain); Γ_0^α denotes the edge of the finite element domain; an example of a model is shown in figure 2.23.

In expressing the total internal potential energy of the system, we employ a scaling parameter α in the overlapping subdomain. The parameter α is defined as $\alpha = \frac{l(\mathbf{X})}{l_0}$ where $l(\mathbf{X})$ is the least square of the projection of $\mathbf{X}$ onto Γ_0^α as shown in figure 2.23. The scaling parameter α is unity at the edge of the finite element domain and vanishes at the other edge of Ω_0^{int}; it is important that Ω_0^{int} includes the last line of particles. In the absence of heat transmission, the conservation of energy of governing equations in the entire domain is:

$$W^{int} = \int_{\Omega_0^{FE}} \beta^{FE} \mathbf{F}^T \cdot \mathbf{P} d\Omega_0^{FE} + \int_{\Omega_0^{P}} \beta^{P} \mathbf{F}^T \cdot \mathbf{P} d\Omega_0^{P} \tag{2.220}$$

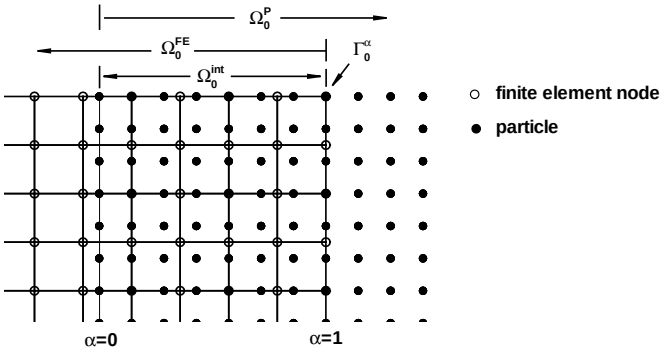

Figure 2.23: Finite element model coupled with particle method

where the scaling multiplier field β is defined as

$$\beta^{FE}(\mathbf{X}) = \begin{cases} 0 & \text{in } \Omega_0^P \\ 1-\alpha & \text{in } \Omega_0^{int} \\ 1 & \text{in } \Omega_0^{FE} - \Omega_0^{int} \end{cases} \tag{2.221}$$

$$\beta^{P}(\mathbf{X}) = \begin{cases} 0 & \text{in } \Omega_0^{FE} \\ \alpha & \text{in } \Omega_0^{int} \\ 1 & \text{in } \Omega_0^{P} - \Omega_0^{int} \end{cases} \tag{2.222}$$

The external energy is:

$$\begin{aligned} W^{ext} &= \int_{\Omega_0^{FE}} \beta^{FE}\rho_0 \mathbf{b}\cdot\mathbf{u} d\Omega_0^{FE} + \int_{\Omega_0^{P}} \beta^{P}\rho_0 \mathbf{b}\cdot\mathbf{u} d\Omega_0^{P} \\ &+ \int_{\Gamma_0^{FE}} \beta^{FE}\overline{\mathbf{t}}\cdot\mathbf{u} d\Gamma_0^{FE} + \int_{\Gamma_0^{P}} \beta^{P}\overline{\mathbf{t}}\cdot\mathbf{u} d\Gamma_0^{P} \end{aligned} \tag{2.223}$$

In Ω_0^{int} the displacements can be approximated in the terms of finite element shape functions $N_I(\mathbf{X})$ or meshfree functions $w_I(\mathbf{X})$, respectively, by:

$$\mathbf{u}^{FE}(\mathbf{X},t) = \sum_I N_I(\mathbf{X})\mathbf{u}_I^{FE}(t) \tag{2.224}$$

$$\mathbf{u}^{P}(\mathbf{X},t) = \sum_I w_I(\mathbf{X})\mathbf{u}_I^{P}(t) \tag{2.225}$$

Therefore, the constraints condition in Ω_0^{int} at the discrete position of particles are

$$\mathbf{g}_I = \{g_{iI}\} = \left\{u_{iI}^{FE} - u_{iI}^{P}\right\} = \left\{\sum_J N_{JI}u_{iJ}^{FE} - \sum_K w_{KI}u_{iK}^{P}\right\} \tag{2.226}$$

The Lagrange multiplier field is also expressed in terms of shape functions denoted by $\Lambda_I(\mathbf{X})$:

$$\lambda_i(\mathbf{X},t) = \sum_I \Lambda_I(\mathbf{X})\overline{\lambda}_{iI}(t) \tag{2.227}$$

Generally, the shape functions for the Lagrange multiplier field $\Lambda_I(\mathbf{X})$ will differ from that for the displacement, $N_I(\mathbf{X})$ or $w_I(\mathbf{X})$, and they must satisfy the Babuska Brezzi conditions. The Lagrange multiplier field is usually represented by inserting finite elements in the intersection domain and the finite element approximation is applied on the particles of the overlapping subdomain. To distinguish the Lagrange multiplier field λ_i in eq. (2.227), $\overline{\lambda}_{iI}$ is denoted as the unknown Lagrange multiplier at the Lagrange multiplier nodes.

Discrete Equations

The energy function for the augmented Lagrangian method is

$$W_{AL} = W^{int} - W^{ext} + \lambda^T\mathbf{g} + \frac{1}{2}p\mathbf{g}^T\mathbf{g} \tag{2.228}$$

where p is the penalty parameter. If $p = 0$, eq. (2.228) will be identical to the expression of the energy function for the Lagrange multiplier method. The discrete equations are then obtained by setting the derivatives of W_{AL} with respect to $\mathbf{u_I}$ and λ_I to zero. This gives

$$\begin{aligned}
\frac{\partial W_{AL}}{\partial u_{iI}^{FE}} &= (F_{iI}^{int} - F_{iI}^{ext}) + \sum_L \left[\left(\sum_K \Lambda_{KL}\overline{\lambda}_K\right) N_{IL}\right] \\
&+ p\sum_L \left[\left(\sum_K N_{KL}u_{iK}^{FE} - \sum_K w_{KL}u_{iK}^{P}\right) N_{IL}\right] = 0 \qquad (2.229)\\
\frac{\partial W_{AL}}{\partial u_{iI}^{P}} &= (f_{iI}^{int} - f_{iI}^{ext}) - \sum_L \left[\left(\sum_K \Lambda_{KL}\overline{\lambda}_K\right) w_{IL}\right] \\
&- p\sum_L \left[\left(\sum_K N_{KL}u_{iK}^{FE} - \sum_K w_{KL}u_{iK}^{P}\right) w_{IL}\right] = 0 \qquad (2.230)\\
\frac{\partial W_{AL}}{\partial \overline{\lambda}_{iI}} &= \sum_L \Lambda_{IL}\left[\sum_K N_{KL}u_{iK}^{FE} - \sum_K w_{KL}u_{iK}^{P}\right] = 0 \qquad (2.231)
\end{aligned}$$

where

$$N_{KI} = N_K(\mathbf{X}_I) \quad \Lambda_{KI} = \Lambda_K(\mathbf{X}_I) \tag{2.232}$$

$\mathbf{F}^{int}$ and $\mathbf{F}^{ext}$ are internal and external force in the finite element subdomain Ω_0^{FE} and they are expressed as:

$$\begin{aligned}
\mathbf{F}_{iI}^{int} &= \int_{\Omega_0^{FE}} \beta^{FE} N_{I,j}(\mathbf{X})\mathbf{P}_{ji}(\mathbf{X})d\Omega_0^{FE} \qquad (2.233)\\
\mathbf{F}_{iI}^{ext} &= \int_{\Omega_0^{FE}} \beta^{FE}\, N_I(\mathbf{X})\rho_0 b_i d\Omega_0^{FE} + \int_{\Gamma_0^t} \beta^{FE}\, N_I(\mathbf{X})\bar{t}_i d\Gamma_0^t \qquad (2.234)
\end{aligned}$$

and $\mathbf{f}^{int}$ and $\mathbf{f}^{ext}$ are internal and external force in the particle subdomain Ω_0^P given by

$$\mathbf{f}_{iI}^{int} = \int_{\Omega_0^P} \beta^P w_{I,j}(\mathbf{X}) \mathbf{P}_{ji}(\mathbf{X}) d\Omega_0^P \tag{2.235}$$

$$\mathbf{f}_{iI}^{ext} = \int_{\Omega_0^P} \beta^P \; w_I(\mathbf{X}) \rho_0 b_i d\Omega_0^P + \int_{\Gamma_0^t} \beta^P \; w_I(\mathbf{X}) \bar{t}_i d\Gamma_0^t \tag{2.236}$$

Letting $\mathbf{d}$ denote the array of $\mathbf{u}$, the increments in the internal nodal force can be approximated in terms of increments in the nodal displacement by stiffness matrices:

$$\Delta \mathbf{F}_I^{int} = \sum_J \mathbf{K}_{IJ}^{FE} \Delta \mathbf{u}_J^{FE} \quad \text{or} \quad \Delta \mathbf{F}^{int} = \mathbf{K}^{FE} \Delta \mathbf{d}^{FE} \tag{2.237}$$

$$\Delta \mathbf{f}_I^{int} = \sum_J \mathbf{K}_{IJ}^{P} \Delta \mathbf{u}_J^{P} \quad \text{or} \quad \Delta \mathbf{f}^{int} = \mathbf{K}^{P} \Delta \mathbf{d}^{P} \tag{2.238}$$

where $\mathbf{K}^{FE}$ and $\mathbf{K}^P$ are tangent stiffness matrices given by

$$\mathbf{K}^{FE} = \begin{bmatrix} \mathbf{K}_{11}^{FE} & \mathbf{K}_{12}^{FE} & & \\ \mathbf{K}_{21}^{FE} & \mathbf{K}_{22}^{FE} & & \\ & & \ddots & \\ & & & \mathbf{K}_{nn}^{FE} \end{bmatrix} \quad \mathbf{K}_{IJ}^{FE} = \frac{\partial \mathbf{F}_I^{int}}{\partial \mathbf{u}_J^{FE}} \tag{2.239}$$

$$\mathbf{K}^{P} = \begin{bmatrix} \mathbf{K}_{11}^{P} & \mathbf{K}_{12}^{P} & & \\ \mathbf{K}_{21}^{P} & \mathbf{K}_{22}^{P} & & \\ & & \ddots & \\ & & & \mathbf{K}_{mm}^{P} \end{bmatrix} \quad \mathbf{K}_{IJ}^{P} = \frac{\partial \mathbf{f}_I^{int}}{\partial \mathbf{u}_J^{P}} \tag{2.240}$$

$$\mathbf{d}^{FE} = \begin{Bmatrix} \mathbf{d}_1^{FE} \\ \mathbf{d}_2^{FE} \\ \vdots \\ \mathbf{d}_n^{FE} \end{Bmatrix} \quad \mathbf{d}_I^{FE} = \begin{Bmatrix} u_{xI}^{FE} \\ u_{yI}^{FE} \end{Bmatrix} \quad \mathbf{d}^{P} = \begin{Bmatrix} \mathbf{d}_1^{P} \\ \mathbf{d}_2^{P} \\ \vdots \\ \mathbf{d}_m^{P} \end{Bmatrix} \quad \mathbf{d}_I^{P} = \begin{Bmatrix} u_{xI}^{P} \\ u_{yI}^{P} \end{Bmatrix} \tag{2.241}$$

The system can then be written as

$$\begin{bmatrix} \mathbf{A}_{11} & \mathbf{A}_{12} & \mathbf{L}^{FE^T} \\ \mathbf{A}_{21} & \mathbf{A}_{22} & \mathbf{L}^{P^T} \\ \mathbf{L}^{FE} & \mathbf{L}^{P} & 0 \end{bmatrix} \begin{Bmatrix} \Delta \mathbf{d}^{FE} \\ \Delta \mathbf{d}^{P} \\ \Delta \overline{\lambda} \end{Bmatrix} = \begin{Bmatrix} -\mathbf{r}^{FE} \\ -\mathbf{r}^{P} \\ -\overline{\mathbf{g}} \end{Bmatrix} \tag{2.242}$$

If we let d_i denote u_{kP} and d_j denote u_{lQ}, the ingredients of eq. (2.242) can be

expressed as:

$$\mathbf{r}^{FE} = \mathbf{F}^{int} - \mathbf{F}^{ext} + \lambda^T \mathbf{G}^{FE} + p\mathbf{g}^T \mathbf{G}^{FE} \tag{2.243}$$

$$\mathbf{r}^{P} = \mathbf{f}^{int} - \mathbf{f}^{ext} + \lambda^T \mathbf{G}^{P} + p\mathbf{g}^T \mathbf{G}^{P} \tag{2.244}$$

$$\overline{\mathbf{g}} = \{\overline{g}_{iI}\} = \left\{ \sum_K \Lambda_{IK} g_{iK} \right\} \tag{2.245}$$

$$\mathbf{A}_{11} = \mathbf{K}^{FE} + p\mathbf{G}^{FE^T} \mathbf{G}^{FE} \tag{2.246}$$

$$\mathbf{A}_{12} = p\mathbf{G}^{FE^T} \mathbf{G}^{P} \tag{2.247}$$

$$\mathbf{A}_{21} = p\mathbf{G}^{P^T} \mathbf{G}^{FE} \tag{2.248}$$

$$\mathbf{A}_{22} = \mathbf{K}^{P} + p\mathbf{G}^{P^T} \mathbf{G}^{P} \tag{2.249}$$

$$\lambda_{iI} = \sum_K \Lambda_K(\mathbf{X}_I) \overline{\lambda}_{iK} \tag{2.250}$$

$$\mathbf{K}^{FE} = \left[\frac{\partial \mathbf{F}^{\mathbf{int}}}{\partial \mathbf{d}^{FE}}\right] = \left[\frac{\partial F_{iI}^{int}}{\partial u_{lQ}^{FE}}\right] = \left[\int_{\Omega_0^{FE}} \beta^{FE} N_{I,j} \overline{C}_{jilk} N_{Q,k} d\Omega_0^{FE}\right] \tag{2.251}$$

$$\mathbf{K}^{P} = \left[\frac{\partial \mathbf{f}^{\mathbf{int}}}{\partial \mathbf{d}^{P}}\right] = \left[\frac{\partial f_{iI}^{int}}{\partial u_{lQ}^{P}}\right] = \left[\int_{\Omega_0^{P}} \beta^{P} w_{I,j} \overline{C}_{jilk} w_{Q,k} d\Omega_0^{P}\right] \tag{2.252}$$

$$\begin{aligned} \mathbf{L}^{FE} &= \left[\sum_L \Lambda_{IL} \frac{\partial \mathbf{g}_L}{\partial d_i^{FE}}\right] = \left[\sum_L \Lambda_{IL} \frac{\partial g_{jL}}{\partial d_i^{FE}}\right] \\ &= \left[\sum_L \Lambda_{IL} \frac{\partial g_L}{\partial u_{kP}^{FE}}\right] = \left[\sum_L \Lambda_{IL} N_{PI} \delta_{jk}\right] \end{aligned} \tag{2.253}$$

$$\begin{aligned} \mathbf{L}^{P} &= \left[\sum_L \Lambda_{IL} \frac{\partial \mathbf{g}_L}{\partial d_i^{P}}\right] = \left[\sum_L \Lambda_{IL} \frac{\partial g_{jL}}{\partial d_i^{P}}\right] = \left[\sum_L \Lambda_{IL} \frac{\partial g_L}{\partial u_{kP}^{P}}\right] \\ &= \left[-\sum_L \Lambda_{IL} w_{PI} \delta_{jk}\right] \end{aligned} \tag{2.254}$$

$$\mathbf{G}^{FE} = \left[\frac{\partial \mathbf{g}_I}{\partial d_i^{FE}}\right] = \left[\frac{\partial g_{jI}}{\partial u_{kP}^{FE}}\right] = [N_{PI}\delta_{jk}] \tag{2.255}$$

$$\mathbf{G}^{P} = \left[\frac{\partial \mathbf{g}_I}{\partial d_i^{P}}\right] = \left[\frac{\partial g_{jI}}{\partial u_{kP}^{P}}\right] = [-w_{PI}\delta_{jk}]$$

Chapter 3

Kinematics of strong and weak discontinuities

A jump in the displacement field is referred to as strong discontinuity. A typical strong discontinuity is a crack. Let us consider an infinite bar with a crack in one dimension, figure 3.1. A linear displacement field adjacent to the crack is assumed. Hence, the strain field will be constant.

Let us consider now the two dimensional case as shown in figure 3.2a. The strong discontinuity is denoted by c and shown in the initial configuration. The discontinuity in the displacement is often considered in the initial configuration where the two opposite crack surfaces coincide in one line. In the current configuration, the two crack surfaces won't coincide. The displacement field of the one side of the crack can be completely different as the displacement field on the opposite side of the crack, even in slope and orientation. The kinematics of the strong discontinuity is given by

$$\dot{\mathbf{u}}(\mathbf{x},t) = \dot{\tilde{\mathbf{u}}} + H_S[\![\dot{\mathbf{u}}]\!](\mathbf{x},\mathbf{t}) \tag{3.1}$$

where $\mathbf{u}$ is the displacement field, the superimposed dot denotes time derivative, ∇ spatial derivatives with respect to spatial coordinates $\mathbf{x}$, t is the time, r and s are local coordinates, H_S is the Heaviside function acting on the discontinuity interface and δ_S is the Dirac delta function also acting on S. With the compatibility condition and eq. (3.1), the strain rate field can be expressed by

$$\dot{\boldsymbol{\epsilon}}(\mathbf{x},t) = \nabla^S \dot{\mathbf{u}} = \nabla^S \dot{\tilde{\mathbf{u}}} + H_S \nabla^S [\![\dot{\mathbf{u}}]\!] + \delta_S \left([\![\dot{\mathbf{u}}]\!] \otimes \mathbf{n} \right)^S \tag{3.2}$$

A *weak* discontinuity is a jump in the strain field as shown in figure 3.2b. It occurs e.g. at material interfaces. It is not well suited to describe the kinematics of a crack. The domain Ω is split by a discontinuity interface S into Ω^+ and Ω^-. The kinematics of the weak discontinuity can then be described by

$$\dot{\mathbf{u}}(\mathbf{x},t) = \dot{\tilde{\mathbf{u}}} + H_{\Omega^h}(r,t)[\![\dot{\hat{\mathbf{u}}}]\!](s,t) \tag{3.3}$$

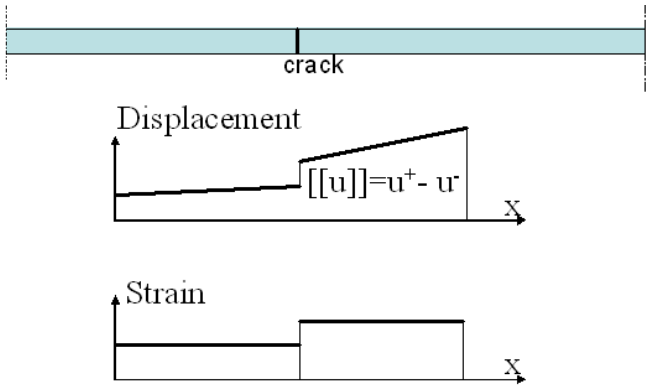

Figure 3.1: Cracking of a one-dimensional bar with corresponding crack kinematics

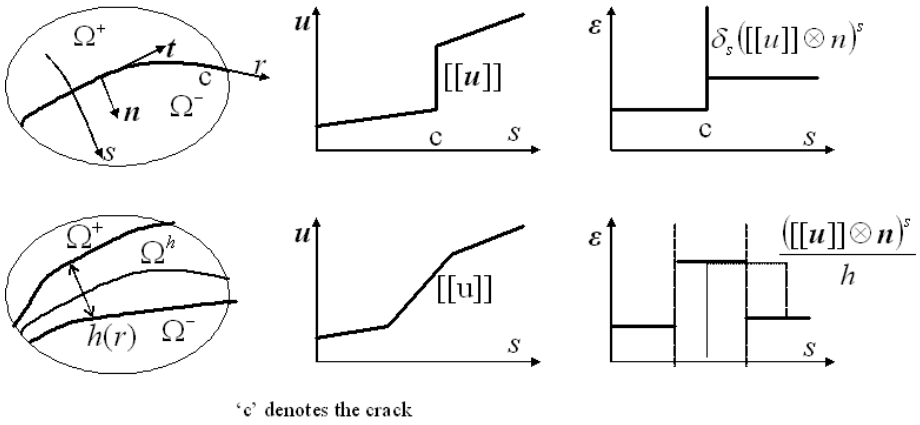

Figure 3.2: Kinematics for a) weak discontinuity, b) strong discontinuity

where H_{Ω^h} denotes the ramp function defined by

$$H_{\Omega^h} = \begin{cases} 0 \ \mathbf{x} \in \Omega^- \setminus \Omega^h \\ 1 \ \mathbf{x} \in \Omega^+ \setminus \Omega^h \\ \frac{s-s^-}{s^+-s^-} \ \mathbf{x} \in \Omega^h \end{cases} \tag{3.4}$$

Formal differentiation gives:

$$\dot{\boldsymbol{\epsilon}}(\mathbf{x},t) = \nabla^S \dot{\mathbf{u}} = \nabla^S \dot{\tilde{\mathbf{u}}} + H_{\Omega^h} \nabla^S [\![\dot{\hat{\mathbf{u}}}]\!] + \nabla H_{\Omega^h} [\![\dot{\hat{\mathbf{u}}}]\!] \tag{3.5}$$

where ∇ denotes spatial derivatives with respect to the local coordinate s. The derivatives of H_{Ω^h} with respect to the local coordinate system (in s-direction) are:

$$\nabla H_{\Omega^h} = \frac{\mathbf{n}}{h(r)} \tag{3.6}$$

where $h(r)$ is the thickness of the localization band and $\mathbf{n}$ is the (unit) normal to the discontinuity interface; note that $h = s^+ - s^-$ is the width of the localization band. Defining the collocation function a that is 1 if $\mathbf{X} \in \Omega^h$ and 0 otherwise, we obtain:

$$\dot{\boldsymbol{\epsilon}}(\mathbf{x},t) = \nabla^S \dot{\mathbf{u}} = \nabla^S \dot{\tilde{\mathbf{u}}} + H_{\Omega^h} \nabla^S [\![\dot{\hat{\mathbf{u}}}]\!] + \frac{a}{h} \left([\![\dot{\hat{\mathbf{u}}}]\!] \otimes \mathbf{n} \right)^S \tag{3.7}$$

Note, that the kinematics described by eqs. (3.3) and (3.1) are independent of the discretization.

Chapter 4

Strong discontinuities in meshfree methods

4.1 A historical overview

4.1.1 The visibility criterion

The visibility method was the first approach that introduced a strong discontinuity into a meshfree discretization. In the visibility method, the crack boundary is considered to be opaque. Thus, the displacement discontinuity is modeled by excluding the particles on the opposite side of the crack in the approximation of the displacement field, see figure 4.1.

Difficulties arise for particles close to the crack tip since undesired interior discontinuities occur (figure 4.2a) since the shape function is cut abruptly, see figure 4.1. Nevertheless, Krysl and Belytschko [14] showed convergence for the visibility method. For the practical important case of linear complete EFG shape functions, they even showed that the convergence rate is not affected by the discontinuity.

It should also be noted that the visibility criterion leads to discontinuities in shape functions near non-convex boundaries such as kinks, crack edges and holes, as shown in figure 4.2b in two dimensions.

4.1.2 The diffraction criterion

The diffraction method is an improvement of the visibility method. It removes the *undesired* interior discontinuities, see figure 4.3 (see also figure 4.1) and the diffraction method is also suitable for non-convex crack boundaries. The method is motivated by the way light diffracts around a sharp corner but the equations used in constructing the domain of influence and the weight function bear almost no relationship to the equation of diffraction. The method is only applicable to radial kernel functions with a single parameter h_{I0}.

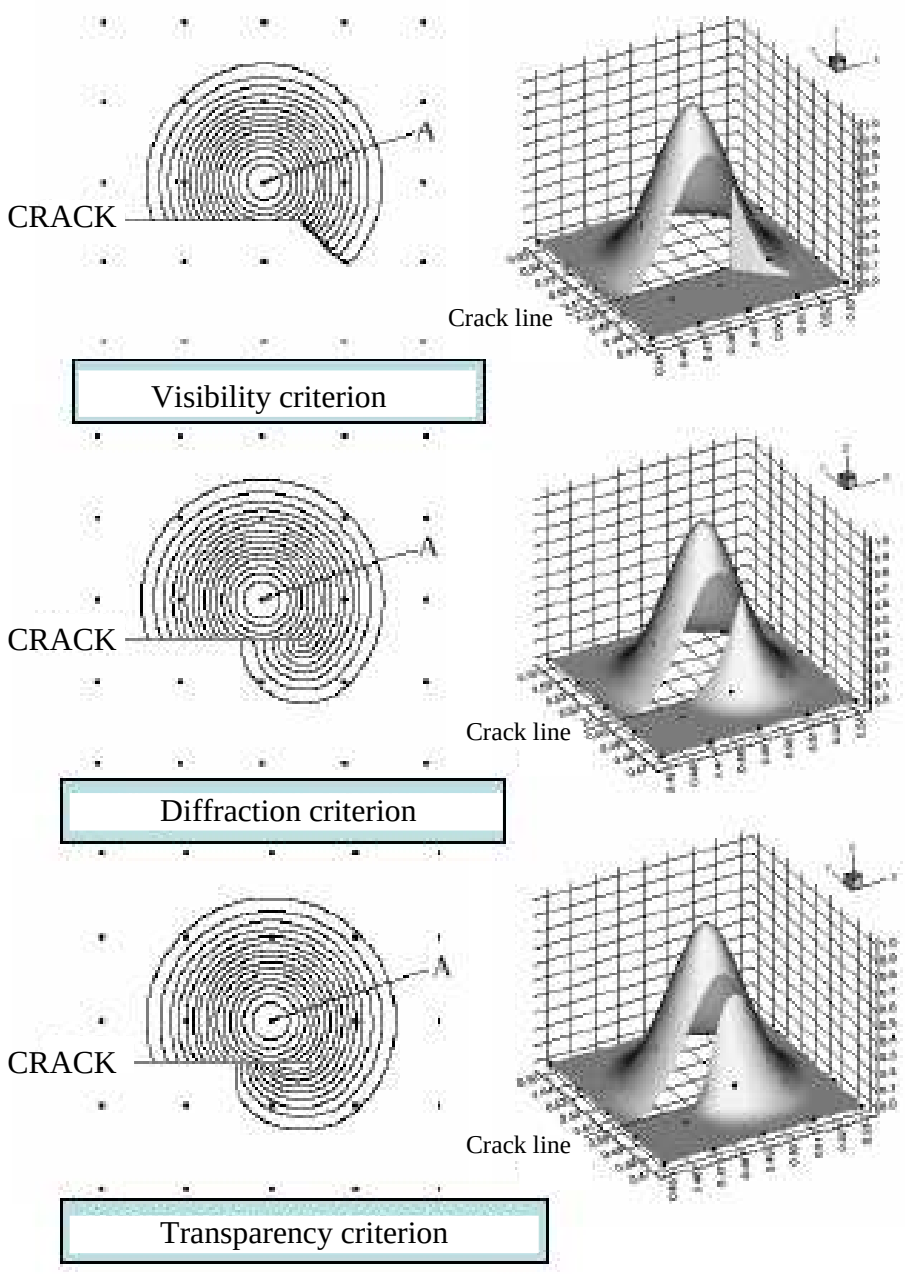

Figure 4.1: Principle of the visibilty, diffraction and transparency method with corresponding shape functions, from Belytschko et al. [2]

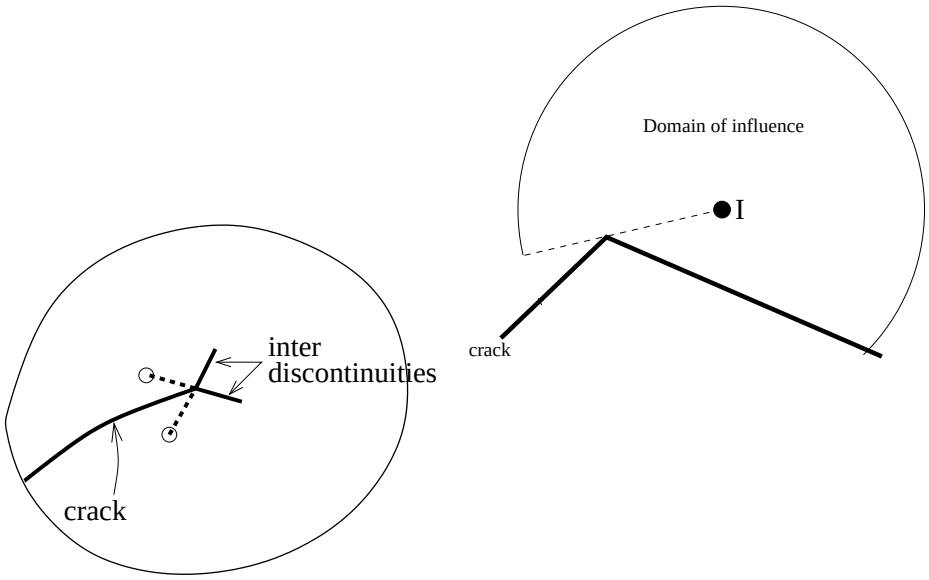

Figure 4.2: a) Undesired introduced discontinuities by the visibility method, b) Difficulties with the visibility method for concave boundaries and kinks

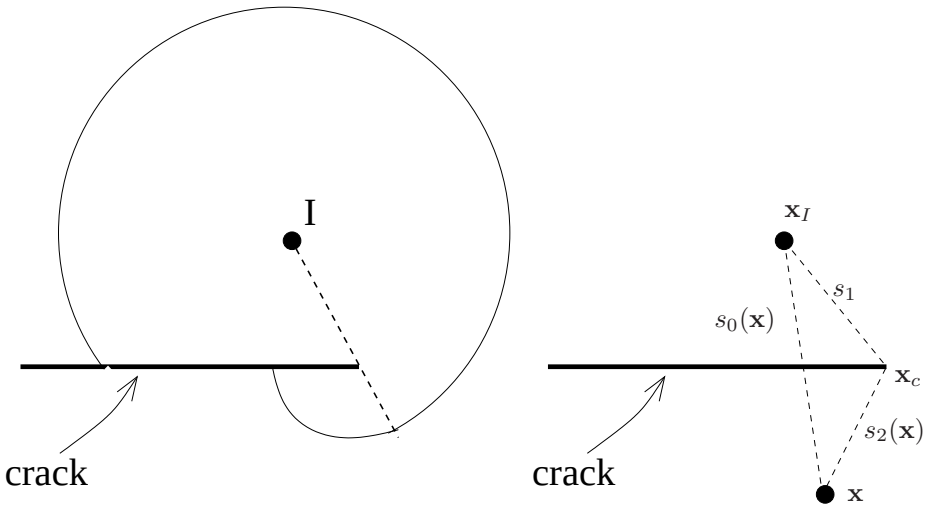

Figure 4.3: The diffraction method

The idea of the diffraction method is to treat the crack as opaque but to evaluate the length of the ray h_0 by a path which passes around the corner of the discontinuity. This removes the abrupt cut of the shape function to zero across the *undesired* interior discontinuity. A typical weight function is shown in figure 4.1. The weight parameter h_{I0} is computed by

$$h_{I0}(\mathbf{X}) = \left(\frac{s_1 + s_2(\mathbf{X})}{s_0(\mathbf{X})} \right)^{\lambda} s_0(\mathbf{X}) \tag{4.1}$$

where

$$\begin{aligned} s_0(\mathbf{X}) &= \|\mathbf{X} - \mathbf{X}_I\| \\ s_1 &= \|\mathbf{X}_c - \mathbf{X}_I\| \\ s_2(\mathbf{X}) &= \|\mathbf{X} - \mathbf{X}_c\| \end{aligned} \tag{4.2}$$

The parameter λ is usually set between one and two and adjusts the distance of the support on the opposite side of the crack. For a better illustration, see also figure 4.3. It should be noted that the shape function of the diffraction method is quite complex with several areas of rapidly varying derivatives that complicates quadrature of the discrete Galerkin form. Moreover, the extension of the diffraction method into three dimensions is complex. The corrected shape functions are obtained by substituting the modified dilation parameter h_{I0} into the corresponding kernel function. For the use in a Galerkin formulation, the spatial derivatives of the shape functions are needed. This requires the derivatives of the kernel function:

$$\frac{\partial W}{\partial X_i} = \frac{\partial W}{\partial h_{0I}} \frac{\partial h_{0I}}{\partial X_i} \tag{4.3}$$

The first term on the right hand side is unchanged and the second term is

$$\frac{\partial h_{0I}}{\partial X_i} = \lambda \left(\frac{s_1 + s_2(\mathbf{X})}{s_0(\mathbf{X})} \right)^{\lambda - 1} \frac{\partial s_2}{\partial X_i} + (1 - \lambda) \left(\frac{s_1 + s_2(\mathbf{X})}{s_0(\mathbf{X})} \right)^{\lambda} \frac{\partial s_0}{\partial X_i} \tag{4.4}$$

with

$$\begin{aligned} \frac{\partial s_2}{\partial \mathbf{X}} &= \frac{\mathbf{X} - \mathbf{X}_c}{s_2(\mathbf{X})} \\ \frac{\partial s_0}{\partial \mathbf{X}} &= \frac{\mathbf{X} - \mathbf{X}_I}{s_0(\mathbf{X})} \end{aligned} \tag{4.5}$$

4.1.3 The transparency criterion

The transparency method was developed as an alternative to the diffraction method by Organ et al. [15]. The transparency method is easier extendable into three dimensions than the diffraction method. In the transparency method, the crack is made transparent near the crack tip. The degree of transparency is

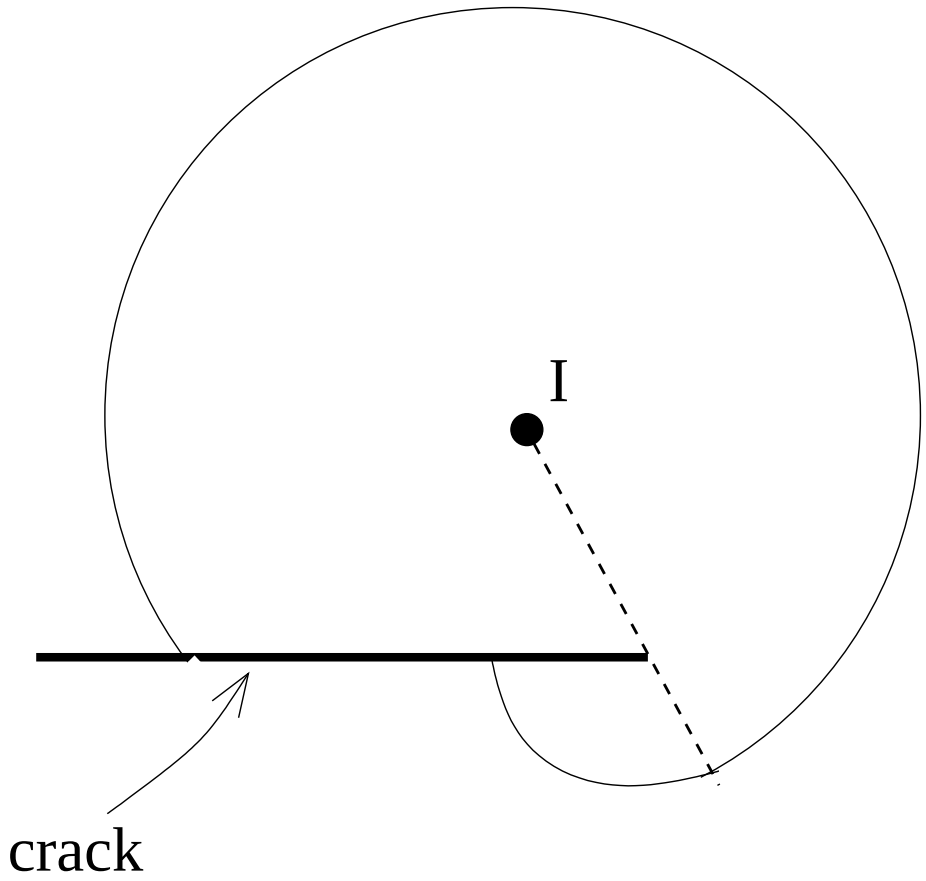

Figure 4.4: The transparency method

related to the distance from the crack tip to the point of intersection, see figure 4.4.

Consider a ray from the evaluation point $\mathbf{X}$ to the node $\mathbf{X}_I$, figure 4.4. The dilation parameter h_{0I} is modified as follows when the ray intersects the crack:

$$h_{0I} = s_0(\mathbf{X}) + h_{mI}\left(\frac{s_c(\mathbf{X})}{\bar{s}_c}\right)^{\lambda}, \quad \lambda \geq 2 \tag{4.6}$$

where $s_0(\mathbf{X})$ is defined in eq. (4.2), h_{mI} is the radius of the nodal support $\mathcal{S}_I$ and $s_c(\mathbf{X})$ is the distance from the crack tip to the intersection point, figure 4.4. The parameter $\bar{s}_c = \kappa h$ sets the intersection distance at which the crack segment is completely opaque where κ is used to vary the opacity and h is a measure of nodal spacing. Note that the additional term in eq. (4.6) is at least quadratic so that the weight function derivatives will be continuous.

An additional requirement is usually imposed for particles close to the crack. Since the angle between the crack and the ray from the node to the crack tip is small, a sharp gradient in the weight function across the line ahead of the crack is introduced. In order to reduce this effect, Organ et al. [15] imposed that all nodes have a minimum distance from the crack surface. The spatial derivatives are obtained by formal differentiation:

$$\frac{\partial h_{0I}}{\partial \mathbf{X}} = \frac{\partial s_0}{\mathbf{X}} + \lambda h_{mI}\frac{s_c^{\lambda-1}}{\bar{s}_c^{\lambda}}\frac{\partial s_c}{\partial \mathbf{X}} \tag{4.7}$$

where we can write

$$\begin{aligned}
\frac{\partial s_0}{\partial \mathbf{X}} &= \frac{\mathbf{X} - \mathbf{X}_I}{s_0(\mathbf{X})} \\
\frac{\partial s_c}{\partial X_1} &= -\cos(\theta) = \frac{X_b - X_c}{s_c(\mathbf{X})} \\
\frac{\partial s_c}{\partial X_2} &= -\sin(\theta) = \frac{Y_b - Y_c}{s_2(\mathbf{X})}
\end{aligned} \tag{4.8}$$

where θ is the angle between the crack and the x-axis. The weight function of the transparency method looks similar to the one of the diffraction method and is illustrated in figure 4.1.

4.1.4 The see-through and continuous line criterion

The "see-through" method was proposed by Terry [16] for constructing continuous approximations near non-convex boundaries. Therefore, the boundary was considered as completely transparent such that the discontinuity is removed. Though the "see-through" method works well for capturing features such as interior holes, it is not well suited to model strong discontinuities.

In the continuous line method from Krysl and Belytschko [14] and Duarte and Oden [9], the crack is completely transparent at the crack tip. In other words, particles whose domain of influence are partially cut by the crack, can see

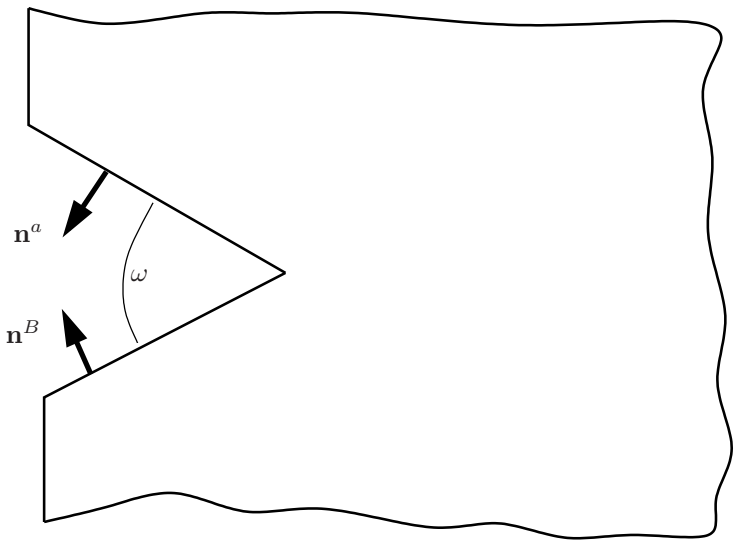

Figure 4.5: Domain of influence near a wedge-shaped non-convex boundary. The boundaryis enforced if $\mathbf{n}^A \cdot \mathbf{n}^B \leq \beta$

through the crack. This drastically shortens the crack. If no special techniques are introduced, the crack also does not close at the crack tip that leads to inaccurate solutions.

4.1.5 Mixed criteria

Belytschko and Fleming [17] suggested to combine different methods depending on the convexity of the crack boundary e.g. to use the visibility for convex boundaries and other methods for non-convex crack boundaries. They suggest a criterion based on the angle of the wedge that can be written in terms of the surface normal, see figure 4.5. When $\mathbf{n}^A \cdot \mathbf{n}^B \leq \beta$ with $\beta = 0^o$ as cutoff value, the boundary can be considered as convex, otherwise non-convex. The cutoff value of $\beta = 0^o$ corresponds to the wedge angle of $\omega = 90^o$ in figure 4.5.

4.2 The concept of enrichment

There are basically two ways of enriching an approximation: an intrinsic enrichment and an extrinsic enrichment. The principal is basically equivalent to the principal of increasing the order of completeness that can be achieved also intrinsically or extrinsically. However, the *enrichment* is aimed to increase the accuracy of the approximation by including information of the analytical solution. The concept of enrichment will be outlined for a strong discontinuity in two dimensions, i.e. for a crack in linear elastic fracture mechanics (LEFM).

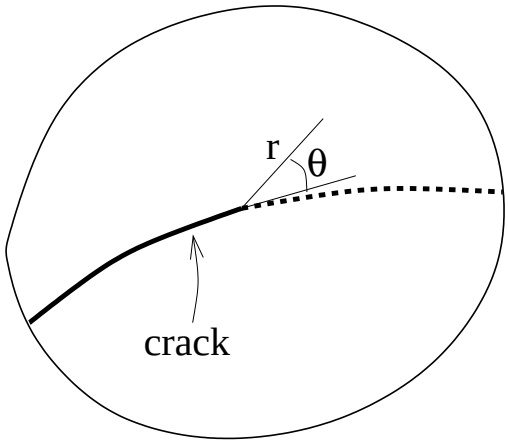

Figure 4.6: Definitions for the crack tip enrichment

Therefore, we will briefly describe the analytical solution of the near crack tip field in LEFM in the next section. In the following section, we will discuss the different enrichments.

4.2.1 Introduction into LEFM

In LEFM, the asymptotic near crack tip displacement field in two dimensions is given by

$$\begin{aligned} u_1 &= \frac{1}{G}\sqrt{\frac{r}{2G}}\left(K_I Q_I^1(\theta) + K_{II} Q_{II}^1(\theta)\right) \\ u_2 &= \frac{1}{G}\sqrt{\frac{r}{2G}}\left(K_I Q_I^2(\theta) + K_{II} Q_{II}^2(\theta)\right) \end{aligned} \tag{4.9}$$

where G is the shear modulus, r and θ are explained in figure 4.6 and

$$\begin{aligned} Q_I^1(\theta) &= \kappa - \cos\frac{\theta}{2} + \sin\theta\,\sin\frac{\theta}{2} \\ Q_I^2(\theta) &= \kappa + \sin\frac{\theta}{2} + \sin\theta\,\cos\frac{\theta}{2} \\ Q_{II}^1(\theta) &= \kappa + \sin\frac{\theta}{2} + \sin\theta\,\cos\frac{\theta}{2} \\ Q_{II}^2(\theta) &= \kappa - \cos\frac{\theta}{2} - \sin\theta\,\sin\frac{\theta}{2} \end{aligned} \tag{4.10}$$

are the angular functions for LEFM, K_I and K_{II} are the mode-I and mode-II stress intensity factors (SIF) where $\kappa = (3-\nu)/(1+\nu)$ for plane stress and $\kappa = (3-4\nu)$ for plane strain is the kolosov constant. Using trigonometric

identities, it can be shown that the basis, given by

$$\mathbf{p}^T(\mathbf{X}) = \left[\sqrt{r}\,\sin(\theta/2), \sqrt{r}\,\cos(\theta/2), \sqrt{r}\,\sin(\theta/2)\sin(\theta), \sqrt{r}\,\cos(\theta/2)\sin(\theta)\right] \tag{4.11}$$

spans the LEFM crack-tip displacement field in eq. (4.9). The angular functions $\mathbf{p} = [B_1, B_2, B_3, B_4]$ are illustrated in figure 4.7

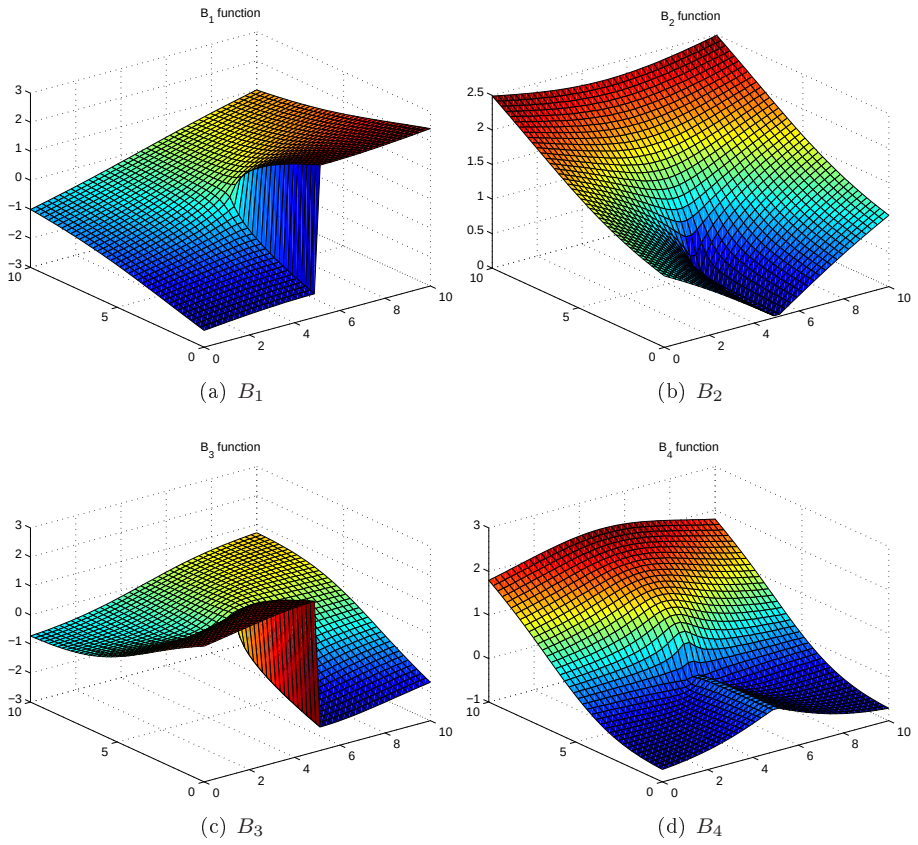

(a) B_1 (b) B_2

(c) B_3 (d) B_4

Figure 4.7: Branch enrichment functions

4.2.2 Intrinsic enrichment

Let us consider the EFG method with MLS basis function $\mathbf{p}$. The intrinsic enrichment is realized by introducing the asymptotic near-tip displacement field of the Westergaard solution into $\mathbf{p}$:

$$\mathbf{p}^T(\mathbf{X}) = \left[1, X, Y, \sqrt{r}\,\sin\frac{\theta}{2}, \sqrt{r}\,\cos\frac{\theta}{2}, \sqrt{r}\,\sin\frac{\theta}{2}\sin(\theta), \sqrt{r}\,\cos\frac{\theta}{2}\sin(\theta)\right] \tag{4.12}$$

where r is the radial distance to the crack tip and θ the angle to the crack (or its virtual extension), see figure 4.6. Note that the linear terms are not related to the asymptotic near crack tip displacement field and can be replaced by higher order polynomials.

Recalling the EFG shape functions

$$\Phi_J(\mathbf{X}) = \mathbf{p}(\mathbf{X})^T \cdot \mathbf{A}(\mathbf{X})^{-1} \cdot \mathbf{p}_J(\mathbf{X})\, W(\mathbf{X} - \mathbf{X}_J, h)$$

$$\mathbf{A}(\mathbf{X}) = \sum_{J \in S} \mathbf{p}_J(\mathbf{X})\ \mathbf{p}_J^T(\mathbf{X})\, W(\mathbf{X} - \mathbf{X}_J, h)$$

the additional computational cost introduced by the intrinsic enrichment becomes obvious. Moreover, the moment matrix $\mathbf{A}$ becomes ill conditioned. The size of the domain of influence has to be enlarged to guarantee the regularity of $\mathbf{A}$. Though this ill-conditioning does not affect the final solution, it is quite troublesome. By diagonalizing $\mathbf{A}$ with a Gram-Schmidt orthogonalization, the regularity of the moment matrix can be drastically improved but leads to more complex shape functions. Moreover, interior discontinuities will be introduced if the intrinsic basis is not employed in the entire body of consideration. Therefore, Fleming et al. [18] proposed a procedure to blend nodes with different basis in a certain transition region, see figure 4.8. The approximation is written by

$$\mathbf{u}^h(\mathbf{X}) = R\ \mathbf{u}^{enr}(\mathbf{X}) + (1 - R)\ \mathbf{u}^{lin}(\mathbf{X}) \tag{4.13}$$

where $\mathbf{u}^{enr}(\mathbf{X})$ is the enriched approximation, $\mathbf{u}$ is the linear approximation and R is a ramp function that is 1 on the enriched boundary of the coupling domain and 0 on the linear boundary of the coupling domain. This is the only requirement imposed on R. Belytschko and Fleming [17] suggested to choose $R = 1 - \xi$ or $R = 1 - 10\xi^3 + 15\xi^4 - 6\xi^5$ with $\xi = (r - r_1)(r_2 - r_1)$ (see figure 4.8). The final approximation then reads

$$\mathbf{u}^h(\mathbf{X}, t) = \sum_{J \in S} u_J(t)\ \bar{\Phi}_J(\mathbf{X}) \tag{4.14}$$

with

$$\bar{\Phi}_J(\mathbf{X}) = R\ \Phi_J^{enr}(\mathbf{X}) + (1 - R)\Phi_J^{lin}(\mathbf{X}) \tag{4.15}$$

where the shape functions $\Phi_J^{enr}(\mathbf{X})$ and $\Phi_J^{lin}(\mathbf{X})$ are formed by the enriched and linear basis, respectively. This blending ensures continuity in the displacement field. However, in case for linear blending, i.e. $R = 1 - \xi$, discontinuities in the strain field occur.

4.2.3 Extrinsic enrichment

Extrinsic MLS-enrichment

In the MLS extrinsic enrichment, the near crack tip asymptotic field of LEFM is as follows:

$$\mathbf{u}^h(\mathbf{X}, t) = \sum_{J \in S} \mathbf{p}(\mathbf{X}_J)^T\ \mathbf{a}(\mathbf{X}, t) + \sum_{K=1}^{n_c} \left(k_I^K\ \mathbf{Q}_I^K(\mathbf{X}_I) + k_{II}^K\ \mathbf{Q}_{II}^K(\mathbf{X}_I) \right) \tag{4.16}$$

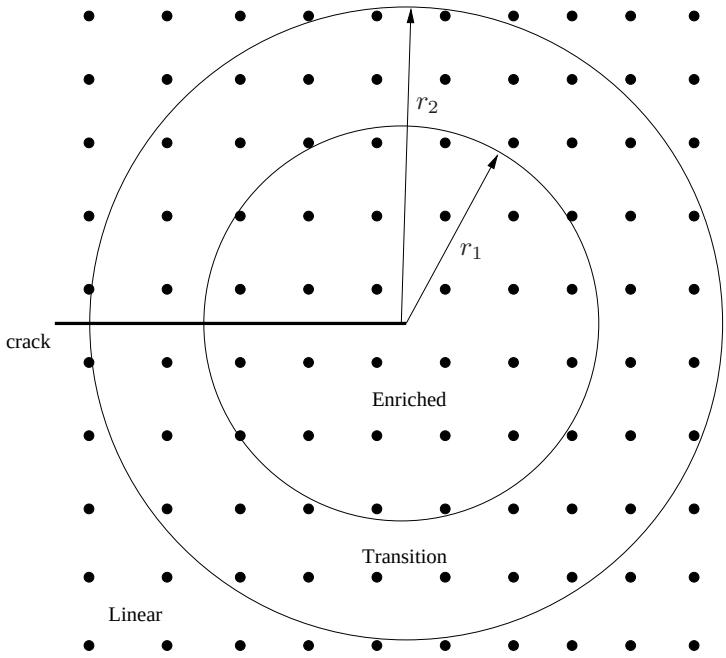

Figure 4.8: Coupling between enriched and linear approximations

where n_c is the number of cracks in the model, $\mathbf{u}^h$ is the approximation of $\mathbf{u}$, $\mathbf{p}$ is the usual polynomial basis of $n-th$ order completeness and k_I and k_{II} are additional degrees of freedom associated with mode-I fracture and mode-II fracture. Note that k_I and k_{II} physically indicate the stress intensity factors (SIF). They can be used as approximate SIFs that can be obtained by directly solving the system of equations without considering the J-integral.

As for the standard MLS approximation, the coefficients $\mathbf{a}$ are determined by minimizing the weighted discrete L_2 error norm

$$\mathcal{J} = \sum_{J\in S} \frac{1}{2} \left(\mathbf{p}(\mathbf{X}_J)^T \mathbf{a}(\mathbf{X},t) + \sum_{K=1}^{n_c} \left[k_I^K \mathbf{Q}_I^K + k_{II}^K \mathbf{Q}_{II}^K \right] - \mathbf{u}_J(t) \right)^2 W(\mathbf{X}-\mathbf{X}_J, h_0) \tag{4.17}$$

that leads with the stationarity of $\mathcal{J}$ to

$$\mathbf{A}(\mathbf{X})\mathbf{a}(\mathbf{X}) = \sum_{J\in\mathcal{S}} \mathbf{P}_J(\mathbf{X}) \left(\mathbf{u}_J - \sum_{K=1}^{n_c} \left[k_I^K \mathbf{Q}_I^K + k_{II}^K \mathbf{Q}_{II}^K \right] \right) \tag{4.18}$$

with

$$\mathbf{A}(\mathbf{X}) = \sum_{J\in S} \mathbf{p}(\mathbf{X}_J)\ \mathbf{p}^T(\mathbf{X}_J)\, W(\mathbf{X}-\mathbf{X}_J, h_0) \tag{4.19}$$

and

$$\mathbf{P}_J(\mathbf{X}) = [W(\mathbf{X}-\mathbf{X}_1, h_0)\mathbf{p}(\mathbf{X}_1), ..., W(\mathbf{X}-\mathbf{X}_n, h_0)\mathbf{p}(\mathbf{X}_n)] \tag{4.20}$$

with n numbers of nodes. Solving eq. (4.18) with respect to $\mathbf{a}$ gives

$$\mathbf{a}(\mathbf{X}) = \sum_{J\in\mathcal{S}} \mathbf{A}^{-1}(\mathbf{X})\mathbf{P}_J(\mathbf{X}) \left(\mathbf{u}_J - \sum_{K=1}^{n_c} \left[k_I^K \mathbf{Q}_I^K + k_{II}^K \mathbf{Q}_{II}^K \right] \right) \tag{4.21}$$

After some algebra, the final approximation in terms of the nodal parameters is obtained:

$$\begin{aligned} \mathbf{u}^h(\mathbf{X}) &= \sum_{J\in\mathcal{S}} \mathbf{p}^T(\mathbf{X})\mathbf{A}^{-1}(\mathbf{X})\mathbf{P}_J(\mathbf{X}) \left(\mathbf{u}_J - \sum_{K=1}^{n_c} \left[k_I^K \mathbf{Q}_I^K + k_{II}^K \mathbf{Q}_{II}^K \right] \right) \\ &+ \sum_{K=1}^{n_c} \left[k_I^K \mathbf{Q}_I^K + k_{II}^K \mathbf{Q}_{II}^K \right] \end{aligned} \tag{4.22}$$

with the shape functions

$$\Phi_J(\mathbf{X}) = \mathbf{p}^T(\mathbf{X})\mathbf{A}^{-1}(\mathbf{X})\mathbf{P}_J(\mathbf{X}) \tag{4.23}$$

that can be written as

$$\mathbf{u}^h(\mathbf{X}) = \sum_{J\in\mathcal{S}} \Phi_J(\mathbf{X})\ \tilde{\mathbf{u}}_J + \sum_{K=1}^{n_c} \left[k_I^K \mathbf{Q}_I^K + k_{II}^K \mathbf{Q}_{II}^K \right] \tag{4.24}$$

with

$$\tilde{\mathbf{u}}_J = \mathbf{u}_J - \sum_{K=1}^{n_c} \left[k_I^K \mathbf{Q}_I^K + k_{II}^K \mathbf{Q}_{II}^K \right] \tag{4.25}$$

Note that the parameters k_I and k_{II} are global parameters and no spatial derivatives are taken with respect to them.

Extrinsic PU enrichment

In the PU-extrinsic enrichment, the asymptotic near-tip displacement field of the Westergaard solution, eq. (4.12) is added externally to the approximation:

$$\mathbf{u}^h(\mathbf{X}) = \sum_{I \in \mathcal{S}} \Phi_I(\mathbf{X}) \left(\mathbf{u}_I + \sum_{J \in \mathcal{S}_c} \mathbf{b}_{IJ} \mathbf{p}_J(\mathbf{X}) \right) \tag{4.26}$$

where $\mathbf{b}_{IJ}$ are additional unknowns introduced into the variational formulation and $\mathcal{S}_c$ is the set of nodes whose domain of influence is cut by the crack tip. The approximation (4.26) is clearly a partition of unity. Note the similarity between this approximation and the approximations described in sections 2.5.4 to 2.5.5.

As might be noted, a compatible approximation is even guaranteed by a *local* partition of unity, meaning only nodes close to the crack tip are enriched. This is a huge advantage from a computational point of view.

Chapter 5

The eXtended finite element method (XFEM)

5.1 Introduction

"Standard" finite element approximations are approximations with piecewise differentiable polynomials that are obviously not well suited for problems with strong and weak discontinuities. The only opportunity to accurately model these kind of discontinuities is to conform the finite element mesh with the line of discontinuity. This becomes a major difficulty for moving discontinuities[1] as already mentioned at the very beginning of this manuscript.

The XFEM is a finite element approximation that is able to handle arbitrary strong and weak discontinuities. XFEM is based on a local[2] extrinsic PU enrichment that idea was used before for strong discontinuities, i.e. cracks, in meshfree methods, see section 4.2.3. Hence, it is not surprising that the first XFEM approximations were developed for cracks. The XFEM concept was later extended to interface problems and weak discontinuities. The basic idea is the same as described in section 4.2.3: To enrich the approximation space such that it is able to reproduce certain features of the problem of interest, e.g. cracks or interfaces.

One important aspect of problems with moving interfaces is the tracking of these interfaces. A powerful tool for tracking interfaces is the level set method that will be explained in the next section. Though it is not mandatory to use level sets in XFEM, most XFEM formulations take advantage of the level set method.

[1] That can occur for moving interfaces in two phase-flow problems or evolving cracks for exemaple

[2] local means that the enrichment is only employed in a certain *local* subdomain. Note that the methods in sections 2.5.4 to 2.5.5 were proposed as *global* PU

5.2 Level sets

5.2.1 Definition

Let us consider a domain Ω that is divided into 2 domains Ω_A and Ω_B. The interface between these two domains is denoted by Γ, see fig. 5.1.

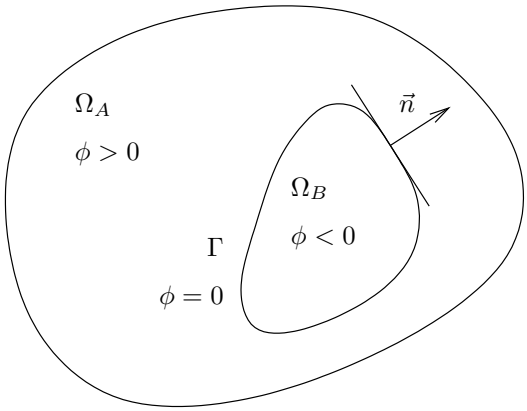

$\Omega = \Omega_A \cup \Omega_B$

$\Omega_A \cap \Omega_B = \varnothing$

Γ : surface of discontinuity (or interface) between Ω_A and Ω_B

Figure 5.1: Description of a two-domain problem by using level sets

Let us define the level set function $\phi(\mathbf{x})$ as

$$\begin{aligned} \phi(\mathbf{x}) > 0 \ \forall \ \mathbf{x} \in \Omega_A \\ \phi(\mathbf{x}) < 0 \ \forall \ \mathbf{x} \in \Omega_B \\ \phi(\mathbf{x}) = 0 \ \forall \ \mathbf{x} \in \Gamma \end{aligned} \tag{5.1}$$

The interface Γ is the zero iso contour of $\phi(\mathbf{x})$. Note that the position of the interface can change with time. Hence, $\phi(\mathbf{x}, t)$ will be time dependent as well.

5.2.2 Normal and curvature

The normal $\mathbf{n}$ to the interface Γ at the point $\mathbf{x} \in \Gamma$ is defined by

$$\mathbf{n} = \frac{\nabla \phi}{\parallel \nabla \phi \parallel} \tag{5.2}$$

If $\parallel \nabla \phi \parallel = 1$, then $\mathbf{n} = \nabla \phi$. The normal $\mathbf{n}$ is oriented from Ω_B to Ω_A if Ω_B is the ϕ-negative domain and Ω_A is the ϕ-positve domain.

The curvature of Γ at a point $\mathbf{x} \in \Gamma$ is defined by

$$\mathcal{K} = n_{i,i} \tag{5.3}$$

If $\parallel \nabla \phi \parallel = 1$ then

$$\mathcal{K} = n_{i,i} = \phi_{,ii} \tag{5.4}$$

5.2.3 Level set for weak form integration

Integration of a function over Ω

Let us suppose that we need to integrate a function $f(\mathbf{x})$ in the domain Ω. This integral can be decomposed into 2 terms on Ω_A and Ω_B:

$$\int_{\Omega} f(\mathbf{x}) = \int_{\Omega_A} f(\mathbf{x}) + \int_{\Omega_B} f(\mathbf{x}) \tag{5.5}$$

With the Heaviside function $H(\xi)$

$$H(\xi) = \begin{cases} 1 & \forall \xi > 0 \\ 0 & \forall \xi < 0 \end{cases} \tag{5.6}$$

the 2 domains Ω_A and Ω_B can be defined by

$$\Omega_A = \{\mathbf{x} \in \Omega / H(\phi(\mathbf{x})) = 1\}$$

$$\Omega_B = \{\mathbf{x} \in \Omega / H(-\phi(\mathbf{x})) = 1\}$$

The previous integral can obviously be re-written as

$$\int_{\Omega} f(\mathbf{x}) = \int_{\Omega} f(\mathbf{x}) H(\phi(\mathbf{x})) + \int_{\Omega} f(\mathbf{x}) H(-\phi(\mathbf{x})) \tag{5.7}$$

Integration of the derivative of a function over Ω_A

Let us consider the integral of the derivative of a function in Ω_A:

$$\int_{\Omega_A} f_{,i}(\mathbf{x}) = \int_{\Omega} f_{,i}(\mathbf{x}) H(\phi(\mathbf{x})) \tag{5.8}$$

The domain integral on the LHS can be transformed into a surface integral by the divergence theorem:

$$\int_{\Omega_A} f_{,i}(\mathbf{x}) = \int_{\partial\Omega_A} f(\mathbf{x}) n_i \tag{5.9}$$

where n_i is the exterior normal to Ω_A. Integration by parts on the RHS of eq. (5.46) gives

$$\int_{\Omega_A} f_{,i}(\mathbf{x}) = \int_{\Omega} \left[\left(f(\mathbf{x}) H(\phi(\mathbf{x})) \right)_{,i} - f(\mathbf{x}) \left(H(\phi(\mathbf{x})) \right)_{,i} \right] \tag{5.10}$$

In order to compute the right hand side, the derivative of $H(\phi(\mathbf{x})$ is needed:

$$\Big(H(\phi(\mathbf{x})) \Big)_{,i} = \phi_{,i}(\mathbf{x}) H_{,i}(\phi(\mathbf{x})) = \phi_{,i}(\mathbf{x}) \delta(\phi(\mathbf{x})) \tag{5.11}$$

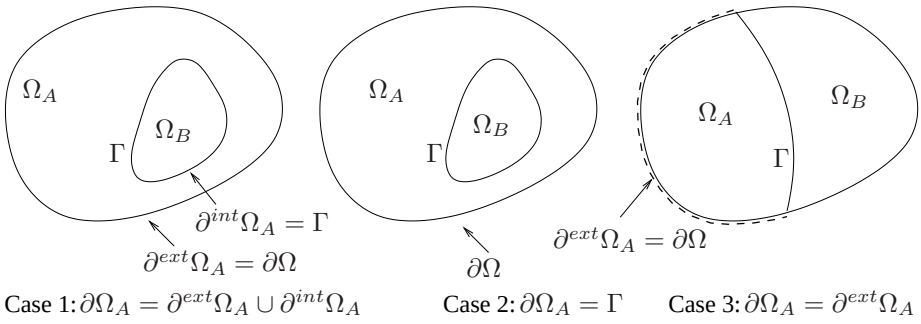

Figure 5.2: Description of a two-domain problem by using level sets

where $\delta(\eta)$ is the dirac delta function. By assuming that the norm of the gradient of ϕ is 1, it has been shown that $\phi_{,i}(\mathbf{x})$ is then equal to the normal $\mathbf{n}^{B\to A}$ to the interface if evaluating on the interface. Finally,

$$\begin{aligned} \Big(H(\phi(\mathbf{x}))\Big)_{,i} &= n_i^{B\to A} \quad \text{on } \Gamma \\ &= 0 \quad \text{otherwise.} \end{aligned} \tag{5.12}$$

The right hand side of the proposed expression leads to:

$$\begin{aligned} \int_\Omega f_{,i}(\mathbf{x})H(\phi(\mathbf{x})) &= \int_\Omega \Big(f(\mathbf{x})H(\phi(\mathbf{x}))\Big)_{,i} - \int_\Omega f(\mathbf{x})\Big(H(\phi(\mathbf{x}))\Big)_{,i} \\ &= \int_{\partial\Omega} f(\mathbf{x})H(\phi(\mathbf{x}))n_i - \int_\Gamma f(\mathbf{x})n_i^{B\to A} \\ &= \int_{\partial\Omega} f(\mathbf{x})H(\phi(\mathbf{x}))n_i + \int_\Gamma f(\mathbf{x})n_i^{A\to B} \end{aligned} \tag{5.13}$$

From the last expression, 3 cases can be examined (fig. 5.2):

Case 1:

$$\begin{aligned} \int_\Omega f_{,i}(\mathbf{x})H(\phi(\mathbf{x})) &= \underbrace{\int_{\partial\Omega}}_{=\partial^{ext}\Omega_A} f(\mathbf{x})\underbrace{H(\phi(\mathbf{x}))}_{=1}n_i + \underbrace{\int_\Gamma}_{=\partial^{int}\Omega_A} f(\mathbf{x})n_i^{A\to B} \\ &= \int_{\partial\Omega_A} f(\mathbf{x})n_i \end{aligned} \tag{5.14}$$

Case 2:

$$\begin{aligned} \int_\Omega f_{,i}(\mathbf{x})H(\phi(\mathbf{x})) &= \int_{\partial\Omega} f(\mathbf{x})\underbrace{H(\phi(\mathbf{x}))}_{=0}n_i + \underbrace{\int_\Gamma}_{=\partial\Omega_A} f(\mathbf{x})n_i^{A\to B} \\ &= \int_{\partial\Omega_A} f(\mathbf{x})n_i \end{aligned} \tag{5.15}$$

Case 3:

$$\begin{aligned}\int_\Omega f_{,i}(\mathbf{x})H(\phi(\mathbf{x})) &= \int_{\partial\Omega} f(\mathbf{x}) \underbrace{H(\phi(\mathbf{x}))}_{=1 \quad \text{onlyif } \mathbf{x}\in\Omega_A} n_i + \int_\Gamma f(\mathbf{x}) n_i^{A\to B} \\ &= \int_{\partial\Omega_A} f(\mathbf{x}) n_i \end{aligned} \tag{5.16}$$

5.2.4 Smoothed Heaviside and Dirac function

It can be necessary to use smoothed functions to avoid numerical problems such as instabilities in the numerical version. For instance, one can use for the Heaviside function:

$$H(\phi) = \begin{cases} 0 & \text{for } \phi < -\epsilon \\ \frac{1}{2} + \frac{\phi}{2\epsilon} + \frac{1}{2\pi}\sin\frac{\pi\phi}{\epsilon} & \text{for } -\epsilon < \phi < \epsilon \\ 1 & \text{for } \epsilon < \phi \end{cases}$$

or

$$H(\phi) = \begin{cases} 0 & \text{for } \phi < -\epsilon \\ \frac{1}{2} + \frac{1}{8}\left(9\frac{\phi}{\epsilon} - 5(\frac{\phi}{\epsilon})^3\right) & \text{for } -\epsilon < \phi < \epsilon \\ 1 & \text{for } \epsilon < \phi \end{cases}$$

Note that ϵ shall be smaller than the element size. A possible smoothed Dirac delta function is

$$\delta(\phi) = \begin{cases} 0 & \text{for } \phi < -\epsilon \\ \frac{1}{2\epsilon} + \frac{1}{2\epsilon}\sin\frac{\pi\phi}{\epsilon} & \text{for } -\epsilon < \phi < \epsilon \\ 0 & \text{for } \epsilon < \phi \end{cases}$$

5.2.5 Signed distance function

A usual level set function is the signed distance function (fig. 5.3). This function reaches the property of beeing zero on the surface of discontinuity. The distance d from a point $\mathbf{x}$ to the interface Γ is

$$d = \| \mathbf{x} - \mathbf{x}_\Gamma \| \tag{5.17}$$

where $\mathbf{x}_\Gamma$ is the normal projection of $\mathbf{x}$ on Γ. The level-set function $\phi(\mathbf{x})$ is set to

$\phi(\mathbf{x}) = d$ in Ω_A,

$\phi(\mathbf{x}) = -d$ in Ω_B.

This can be written as

$$\phi(\mathbf{x}) = \underbrace{\min}_{\tilde{\mathbf{x}}\in\Gamma} \| \mathbf{x} - \tilde{\mathbf{x}} \| \operatorname{sign}\Big(\mathbf{n}\cdot(\mathbf{x} - \tilde{\mathbf{x}})\Big) \tag{5.18}$$

Note that the signed distance function has the following property:

$$\| \nabla\phi \| = 1 \tag{5.19}$$

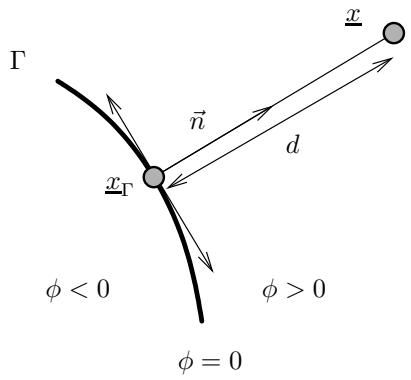

Figure 5.3: Signed distance function

5.2.6 Discretization of the level set

In the general case, the signed distance to the interface is not known analytically. The level set is usually discretized. The discretization is based on a finite element mesh where $N_I(\mathbf{x})$ is the shape function associated to the node I. The set of nodes which belong to the mesh is denoted by $\mathcal{S}$. Note that the same finite element shape functions as for the mechanical properties can be used that facilitates implementation though this is not mandatory, **?**]. The discretized level set is

$$\phi(\mathbf{x}) = \sum_{I \in \mathcal{S}} N_I(\mathbf{x}) \phi_I \tag{5.20}$$

where ϕ_I is the value of the level set on node I. This discretization becomes usefull when the value of the level set is needed at the element level. It can be evaluated by interpolation. Moreover, the derivative of the level set involves only the well known derivatives of the shape functions:

$$\phi(\mathbf{x})_{,i} = \sum_{I \in \mathcal{S}} N_{I,i}(\mathbf{x}) \phi_I \tag{5.21}$$

5.2.7 Updating the level set of the interface

When the discontinuity evolves in time, the level set has to be updated. Note that there are subtle differences between cracks and phase-interfaces. While phase-interfaces generally evolve perpendicular to the interface and the phase-interfaces are close curves, cracks are open curves and the crack propagates perpendicular to its normal from its crack tip. Since a crack is an open curve, one level set is not sufficient to describe the crack. Another level set $\tilde{\phi}$ at the crack tip, generally perpendicular to the level set that describes the crack, has to be introduced. Hence, after updating the level set of the moving discontinuity, i.e. the crack, the level set at the crack tip has to be updated as well. Usually, it is required that these two level sets fulfill the orthogonality condition $\phi_{,i}\, \tilde{\phi}_{,i} = 0$.

Updating of the interface in its normal direction

In general, the position of the discontinuity is not known *a priori*. The level set has to be zero on the interface. Hence, the material time derivative of ϕ has to be zero:

$$\frac{D\phi(\mathbf{x},t)}{Dt} = 0 \tag{5.22}$$

By assuming that the discontinuity moves with a velocity field $\mathbf{v}$, the previous equation can be written as

$$\frac{\partial\phi(\mathbf{x},t)}{\partial t} + \nabla\phi(\mathbf{x},t)\cdot\mathbf{v}(\mathbf{x},t) = 0 \tag{5.23}$$

or

$$\dot{\phi} + \phi_{,i}v_i = 0 \tag{5.24}$$

This equation is known as the Hamilton-Jacobi equation. Using a first-order time scheme leads to

$$\frac{\phi^{n+1}-\phi^n}{\Delta t} = -\phi^n_{,i}v^n_i \tag{5.25}$$

and to

$$\phi^{n+1} = \phi^n - \Delta t\ \phi^n_{,i}v^n_i \tag{5.26}$$

where Δt is the time step. For a phase-interface problem such as in bi-phasic fluid flow or in fluid-structure interaction (FSI) problems, the velocity field is given by the flow or by the structure that moves in the fluid field, respectively. However, in case of a propagating crack, the crack speed is generally unknown. Hence, to update (meaning propagate) the crack surface, other criteria have to be found.

Reinitialization

After evolving ϕ under a general speed v_i, it generally does not remain a signed distance function. Therefore, ϕ can be reinitialized by finding a new ϕ with the same zero level set but with $|\nabla\phi| = 1$. If the position of the discontinuity is known at each time step, the signed distance function can be re-computed in order to build the level-set.

5.2.8 Level set for solid shape description

Computational model

Let us consider a body which is initially in the domain Ω_0 with boundary Γ_0. We will first describe the procedure for the case when the object is enclosed by a single surface. It may be convex or concave. The procedure consists of the following steps:

- an implicit function is constructed such that $\phi(\mathbf{X}) = 0$ defines the surface of the body and $\phi(\mathbf{X}) > 0$ inside the body.

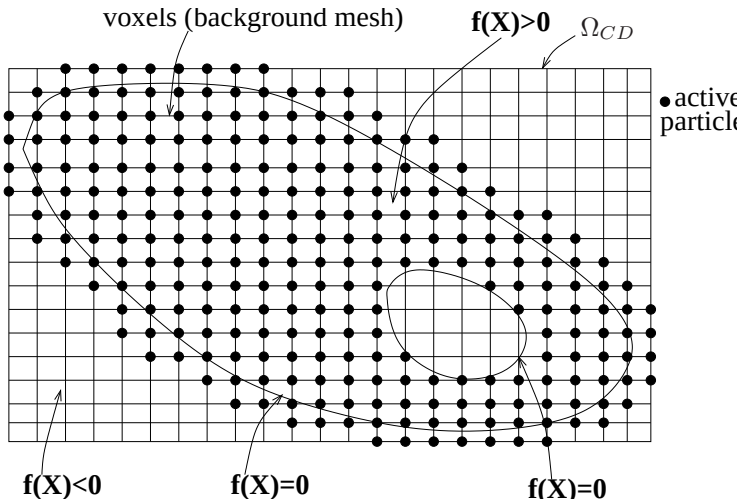

Figure 5.4: Computational scheme: the implicit function $\phi(\mathbf{X})$, particle arrangement and pixels, which also serve as background quadrature cells

- a set of pixels that encompass the entire domain for which $\phi(\mathbf{X}) \geq 0$ is constructed; at the corners of the pixels, nodes $\mathbf{X}_I$ are defined. They do not necessarily need to be connected to a finite element discretization. The procedure is also applicable to meshfree methods.

- a set of active nodes is defined by $I \ni N_{act}$ if $\phi(\mathbf{X}_I) \geq 0$ or if $\phi(\mathbf{X}_I) = 0$ for any pixel containing $\mathbf{X}_I$.

We start with the set of points that define the object. The points can be taken either directly from the object by a scanner when an existing component is to be analyzed, or they may be based on a CAD model. The first step is to construct the implicit function description of the body. The surfaces are described by fitting an approximant to a set of points on the surface $\bar{\mathbf{X}}_I$, I=1 to n_{sp}. A set of off-surface points $\bar{\mathbf{X}}_I$, I=1 to n_{ip} is also needed; these are generated by moving away from the surface by an approximate surface normal. The surface of the body is described by

$$\phi(\mathbf{X}) = 0 \tag{5.27}$$

i.e. the surface is the zero isobar of the function $\phi(\mathbf{X})$. The expression for $\phi(\mathbf{X})$ in terms of the approximating functions $N_I(\mathbf{X})$ is

$$\phi(\mathbf{X}) = \sum_{I \in S} N_I(\mathbf{X})\ \mathbf{X}_I \tag{5.28}$$

The outcome of these steps are illustrated in figure 5.4.

Background mesh (voxels) and active pixels

The implicit function is enclosed by a bounding box $\mathcal{B}$ that includes all points $\mathbf{X}$ such that $\phi(\mathbf{X}) > 0$; this bounding box is called the computational domain Ω_{CD}. The bounding box refers to the reference domain (i.e. the initial configuration of the body), so its size does not change as the body deforms. Note that the bounding box does not necessarily have to be rectangular. The bounding box could also consist of unions of rectangular boxes.

An array of pixels is then constructed. The selection of the pixel size is a crucial step in the procedure, since it is necessary to determine a pixel size that leads to reasonably economical computations, yet corresponds closely enough with the details of the object so that the boundaries of the object in each pixel are simple. Note that in the initial selection of pixel size, resolution of the geometry is more important than accuracy of the solution. The selection of active pixels is then made by the criterion $\phi(\mathbf{X}_I) \leq \alpha\ h_p$, where h_p is the pixel dimension and α is a constant between zero and one.

5.3 Standard XFEM

XFEM is based on a local partition of unity. It uses an extrinsic enrichment to model the weak or strong discontinuity within a finite element. The XFEM approximation can be decomposed into a usual part and into an enriched part

$$\mathbf{u}^h(\mathbf{X}) = \sum_{J \in \mathcal{S}} N_J(\mathbf{X})\ \mathbf{u}_J + \sum_{K \in \mathcal{E}} \sum_{J \in \mathcal{S}_c} \tilde{N}_J^K(\mathbf{X})\ \psi^K(\mathbf{X})\ \mathbf{a}_J^K \tag{5.29}$$

where the first term on the RHS of eq. (5.29) is the usual approximation and the second term on the RHS of eq. (5.29) is the enrichment. $\mathcal{S}$ is the set of nodes in the entire discretization and $\mathcal{S}_c$ is the set of enriched nodes that are influenced by the interface; N_J and $\tilde{N}_J$ are the shape functions[3]. $\psi(\mathbf{X})$ is an enrichment function that is chosen according to the problem of interest[4] and a_J are additional degrees of freedom introduced into the variational formulation. The set $\mathcal{E}$ is the number of interfaces[5]. If we have only a single interface, then the first sum of the second term of the right hand side of equation (5.29) can be omitted (as well as the superimposed K).

5.3.1 Application to strong discontinuities

Let us use the XFEM enrichment with $N_J(X) = \tilde{N}_J(X)$ to be able to model one single strong discontinuity in one dimension. Therefore, the enrichment function ψ is chosen to be the step function S:

$$S(\xi) = \begin{cases} 1 & \forall \xi > 0 \\ -1 & \forall \xi < 0 \end{cases} \tag{5.30}$$

[3] Note that generally different shape functions can be used for the standard part and for the enrichment

[4] $\psi(\mathbf{X})$ will differ for a strong and weak discontinuity

[5] e.g. cracks

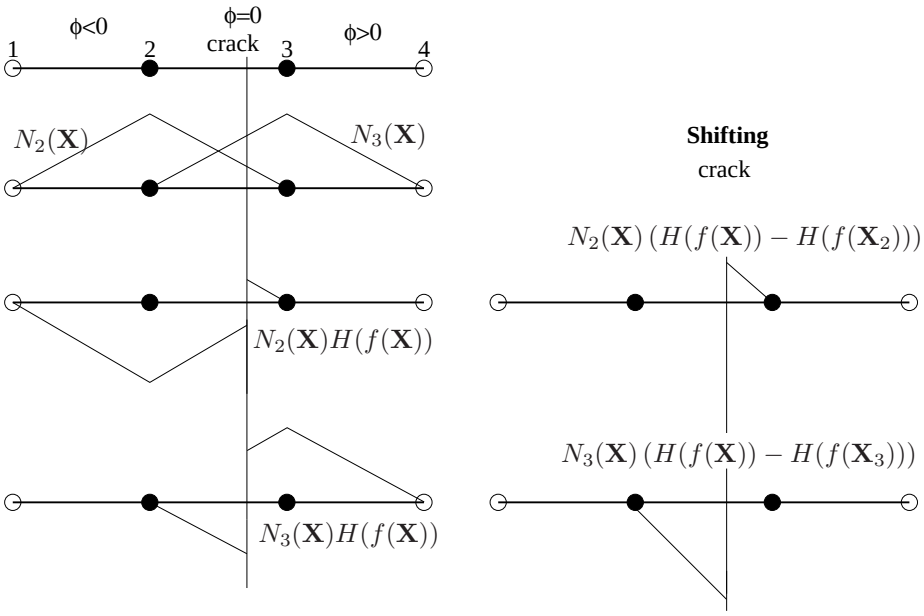

Figure 5.5: Principle of XFEM in 1D for a strong discontinuity

The approximation (5.29) then reads:

$$u^h(X) = \sum_{J \in \mathcal{S}} N_J(X)\ u_J + \sum_{J \in \mathcal{S}_c} N_J(X)\ S(\phi(X))\ a_J \tag{5.31}$$

Moreover, we assume linear shape functions $N_1 = 0.5(1-r)$, $N_2 = 0.5(1+r)$, where r is a local scaled element coordinate. Let us consider three finite elements as shown in figure 5.5. The shape functions $N_2(X)$ of node 2 and $N_3(X)$ of node 3 are shown in figure 5.5 as well. The nodes are numbered in ascending order from 1 to 4. The element in the middle supposed to have a strong discontinuity, i.e. a crack, at an arbitrary location X_c between node 2 and node 3. Therefore, the nodes 2 and 3 will be enriched. The nodes 1 and 4 will not be enriched since they are not influenced by the crack.

The crack is defined with the level set $\phi(X_c) = 0$ where X_c is the global position of the crack and $\phi(X) < 0$ when $X < X_c$ and $\phi(X) > 0$ when $X > X_c$. Since for the coordinate of node 2, $X_2 < X_c$, it follows that $S(\phi(X_2)) = -1$. Accordingly, $S(\phi(X_3)) = 1$ since it lies on the opposite side of the crack with $X_3 > X_c$. The resulting enriched shape functions $N_J(X)\ S(X)$ for nodes 2 and 3 are shown on the LHS of figure 5.5 as well. From (5.31), it is obvious that the value of $u(X)$ on an enriched node $K \in \mathcal{S}_c$ is

$$u(X_K) = u_K + S(\phi(X_K))\ a_J \tag{5.32}$$

Thus, the nodal parameter u_K is not the real displacement value on the node.

In order to satisfy this relation, the enriched shape functions are shifted around the node of interest:

$$u^h(X) = \sum_{J\in\mathcal{S}} N_J(X)\ u_J + \sum_{J\in\mathcal{S}_c} N_J(X)\ \left(S(\phi(X)) - S(\phi(X_J))\right)\ a_J \tag{5.33}$$

such that $u(X_K) = u_K$. The result of this shifting is illustrated on the RHS of figure 5.5. We note that the enriched region is getting narrower. This shifting is standard in XFEM. The jump in the displacement field is given by

$$\begin{aligned}
[\![u^h(X)]\!] &= u(X^+) - u(X^-) \\
&= \sum_{J\in\mathcal{S}} N_J(X^+)\ u_J + \sum_{J\in\mathcal{S}_c} N_J(X^+)\ \left(S(\phi(X^+))\right)\ a_J \\
&- \sum_{J\in\mathcal{S}} N_J(X^-)\ u_J + \sum_{J\in\mathcal{S}_c} N_J(X^-)\ \left(S(\phi(X^-))\right)\ a_J \\
&= \sum_{J\in\mathcal{S}_c} N_J(X)\left(\left[S(\phi(X^+)) - S(\phi(X^-))\right]\right)\ a_J \\
&= 2\sum_{J\in\mathcal{S}_c} N_J(X)\ a_J
\end{aligned} \tag{5.34}$$

Here, we have used the continuity of the shape functions across the crack, i.e. $N_J(X^-) = N_J(X^+)$. Several authors prefer to use the Heaviside function instead of the step function to model the jump in the displacement field. In that case, eq. (5.34) becomes:

$$\begin{aligned}
[\![u^h(X)]\!] &= \sum_{J\in\mathcal{S}_c} N_J(X)\left(\left[H(\phi(X^+)) - H(\phi(X^-))\right]\right)\ a_J \\
&= \sum_{J\in\mathcal{S}_c} N_J(X)\ a_J
\end{aligned} \tag{5.35}$$

and hence the jump is $\sum_{J\in\mathcal{S}_c} N_J(X)\ a_J$ instead of $2\sum_{J\in\mathcal{S}_c} N_J(X)\ a_J$. Note that the choice of the jump in the enrichment function does not matter. The nodal parameters will adjust automatically.

5.3.2 Application to weak discontinuities

For a weak discontinuity, the enrichment function ψ is chosen to be the signed distance function ϕ:

$$\psi_J(\mathbf{x}, t) = |\phi(\mathbf{x}, t)| - |\phi(\mathbf{x}_J, t)| \tag{5.36}$$

The approximation (5.29) then reads:

$$v^h(x) = \sum_{J\in\mathcal{S}} N_J(x)\ v_J(t) + \sum_{J\in\mathcal{S}_c} N_J(x)\ \psi_J(\phi(x), t)\ a_J(t) \tag{5.37}$$

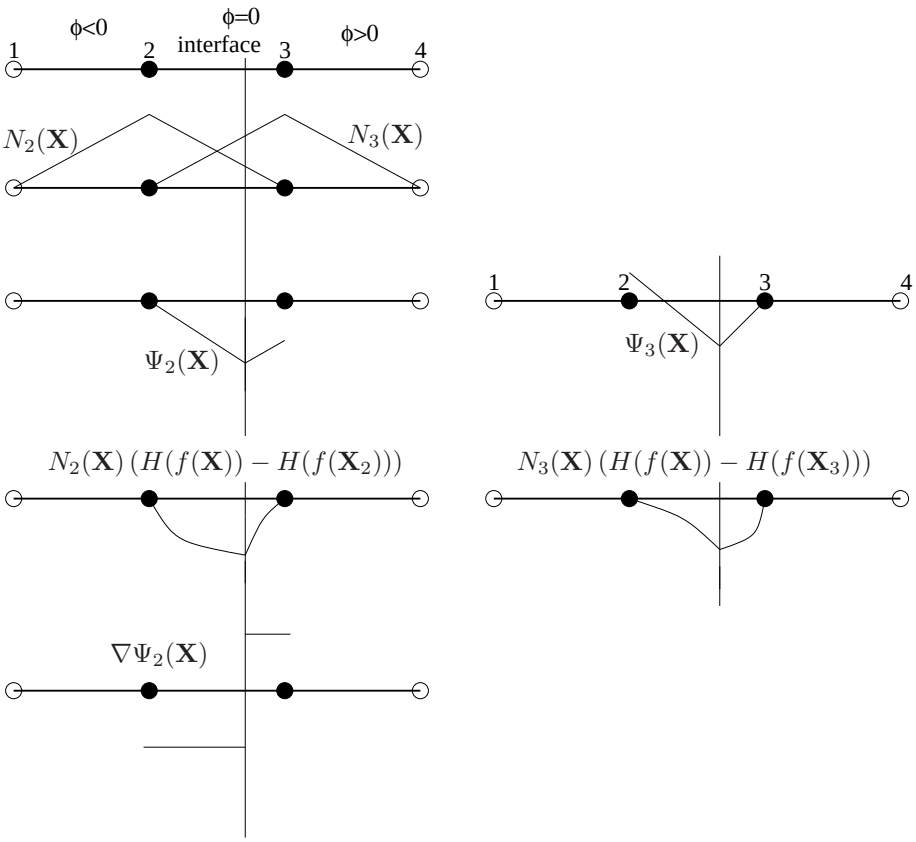

Figure 5.6: Principle of XFEM in 1D for a weak discontinuity

where $\mathcal{S}_c$ denotes the inferfacen. Note that we have written the approximation in terms of spatial coordinates since weak discontinuities are often associated in fluid mechanics (two-phase flow). Hence, we have also used the letter v instead of u that should indicate velocity instead of displacement. We consider again 3 elements in one dimension that are numbered from 1 to 4 in ascending order and with the interface between node 2 and node 3, see figure 5.6. The enrichment function ψ for node 2 and node 3 is illustrated as well. As can be seen, a kink is introduced that will cause the jump in the gradient of the function since the jump occurs in the derivatives of ψ, see the bottom on the LHS of figure 5.6. The resulting shape function $N_2(\mathbf{x},t)\ \psi_2(\mathbf{x},t)$ for node 2 and $N_3(\mathbf{x},t)\ \psi_3(\mathbf{x},t)$ for node 3 are shown in figure 5.6, too. The velocity gradient is obtained by formal differentiation of eq. (5.37):

$$\begin{aligned} \nabla v^h(x) &= \sum_{J\in\mathcal{S}} \nabla N_J(x) v_J(t) \\ &+ \sum_{J\in\mathcal{S}_c} \left(\nabla N_J(x)\ \psi_J(\phi(x),t) + N_J(x)\ \nabla\psi_J(\phi(x),t)\right)\ a_J(t) \end{aligned} \tag{5.38}$$

with

$$\nabla\psi_J(\mathbf{x},t) = \text{sign}(\phi)\ \nabla\phi = \text{sign}(\phi)\mathbf{n}_{int} \tag{5.39}$$

where $\mathbf{n}_{int}$ denotes the normal to the interface. The only term that can cause the jump is $\nabla\psi_J(\mathbf{x},t)$. Similar to the jump in the displacement field, we obtain the jump in the strain field

$$[\![\nabla v^h(X)]\!] = 2\sum_{J\in\mathcal{S}_c} N_J(X)\ a_J\ \mathbf{n}_{int} \tag{5.40}$$

or the jump normal to the inferface:

$$[\![\nabla v^h(X)\mathbf{n}_{int}]\!] = 2\sum_{J\in\mathcal{S}_c} N_J(X)\ a_J \tag{5.41}$$

where the factor 2 results from the step size from -1 to 1, see figure 5.6.

5.4 Hansbo-Hansbo XFEM

An alternative to the standard XFEM for strong discontinuities was proposed by Hansbo and Hansbo [19]. They do not model the crack kinematics with additional degrees of freedom but by overlapping elements, see figure 5.7. The Hansbo and Hansbo [19] XFEM-version can be derived from standard XFEM. Therefore, let us consider the approximation of the discontinuous displacement field for a linear finite element in one dimension:

$$\begin{aligned} u^h(X) &= \sum_{I=1}^{2} N_I(X)\left[u_I + a_I\left(H(X-X_c) - H(X_I - X_c)\right)\right] \\ &= u_1\ N_1 + u_2\ N_2 + a_1\ N_1\ H(X-X_c) \\ &+ a_2\ N_2\ \left[H(X-X_c) - 1\right] \end{aligned} \tag{5.42}$$

where H is the Heaviside function. With $N_I = N_I\,H(X-X_c)+N_I\,(1-H(X-X_c))$, $I=1,2$, we can rewrite eq. (5.42)

$$\begin{aligned} u^h(X) &= (u_1+a_1)\,N_1\,H(X-X_c) + u_1\,N_1\,(1-H(X-X_c)) \\ &+ (u_2-a_2)\,N_2\,(1-H(X-X_c)) + u_2\,N_2\,H(X-X_c) \end{aligned} \tag{5.43}$$

Let us define

$$\text{element1}\left\{\begin{array}{c} u_1^1 = u_1 \\ u_2^1 = u_2 - a_2 \end{array}\right. \tag{5.44}$$

$$\text{element2}\left\{\begin{array}{c} u_1^2 = u_1 + a_1 \\ u_2^2 = u_2 \end{array}\right. \tag{5.45}$$

where superscripts and subscripts denote the element and node numbers, respectively. Eq. (5.43) can then be rewritten as

$$\begin{aligned} u^h(X) &= u_1^1\,N_1\,(1-H(X-X_c)) + u_2^1 N_2\,(1-H(X-X_c)) \\ &+ u_1^2\,N_1\,H(X-X_c) + u_2^2\,N_2\,H(X-X_c) \end{aligned} \tag{5.46}$$

Thus, we can consider the displacement field to consist of the displacement fields of two elements: element 1, which is only active for $X < X_c$ due to $(1-H(X-X_c))$ and element 2, which is only active for $X > X_c$ due to $H(X-X_c)$. The displacement jump across the crack is then:

$$\begin{aligned} [\![u^h(X)]\!]_{X=X_c} &= \underbrace{\lim_{\epsilon\to 0}}_{\epsilon\to 0}\,[u(X+\epsilon)-u(X-\epsilon)]_{X=X_c} \\ &= N_1(X_c)\,\left(u_1^2-u_1^1\right) + N_2(X_c)\,\left(u_2^2-u_2^1\right) \\ &= a_1\,N_1(X_c) + a_2\,N_2(X_c) \end{aligned} \tag{5.47}$$

From eq. (5.46), we can see that the discontinuous field can be constructed by adding an extra element, element 2 in that case, as shown in figure 5.7. Then, two additional nodes are added (u_2^1 and u_1^2). The two parts of the model are completely disjoint.

5.5 Blending elements

Around the enriched domain Ω^{PU} which is the support of the partition of unity, there is a partial enriched area where the elements do not have all their nodes enriched. These elements are called blending (or partial enriched) elements (fig. 5.8). The approximation in a 4-node element which has less than 4 enriched nodes, 3 for instance, is

$$u_i^h(\mathbf{x}) = \sum_{I=1}^{4} N_I(\mathbf{x})u_{Ii} + \sum_{J=1}^{3} N_J(\mathbf{x})\psi(\mathbf{x})a_{Ji} \tag{5.48}$$

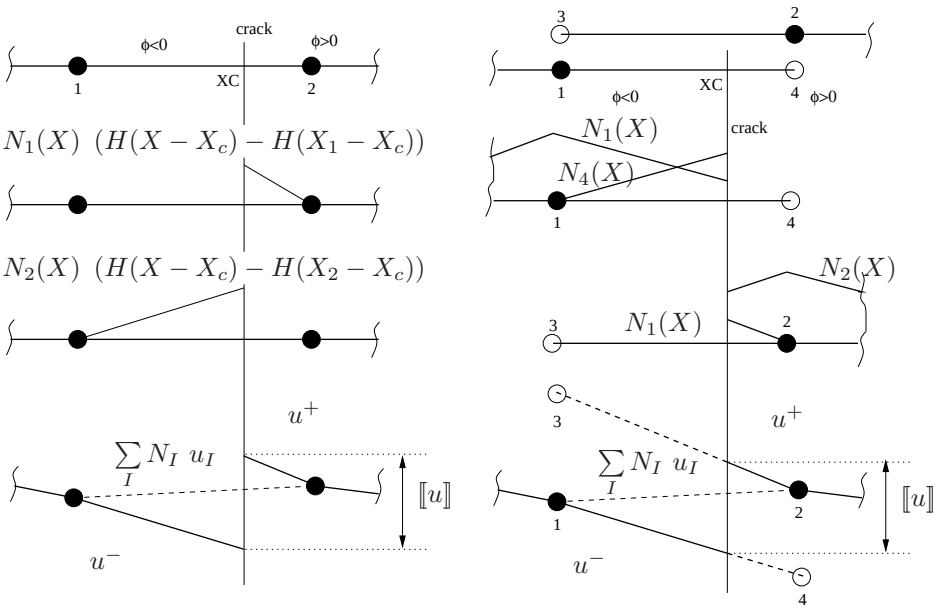

Figure 5.7: Standard XFEM vs. Hansbo XFEM

In this element the function $\psi(\mathbf{x})$ can not be recovered by taking $u_{Ii} = 0$ and $a_{Ji} = 1$ because (N_1, N_2, N_3) is not anymore a partition of unity, in other terms,

$$\sum_{J=1}^{3} N_J(\mathbf{x}) \neq 1. \tag{5.49}$$

The fact that the additional function can not be recovered in these elements is not important since these elements do not contain the discontinuity. The main point is that it may introduce spurious terms in the approximation which produce an error in the solution. The spurious terms can be automatically corrected by the standard part of the approximation if the order of the standard part is more or equal than the order of the partition of unity times the enrichment. Table 5.1 shows a few possible combinations.

The spurious terms can be corrected by an assumed strain method [20]. The finite element shape functions form a partition of unity

$$\sum_{I \in N} N_I(\mathbf{x}) = 1 \tag{5.50}$$

It follows from the above that for an arbitrary function $\Psi(\mathbf{x})$, the following satisfies

$$\sum_{I \in N} N_I(\mathbf{x})\Psi(\mathbf{x}) = \Psi(\mathbf{x}) \tag{5.51}$$

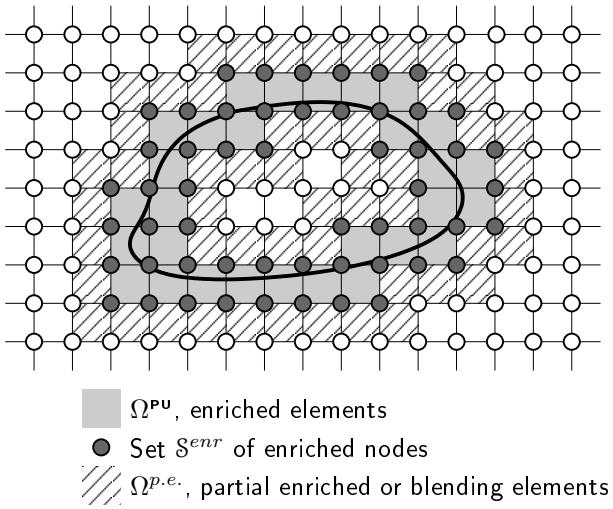

Figure 5.8: Partial enriched around the enriched area.

Standard shape functions $N_I(\mathbf{x})$	Partition of unity $f_i(\mathbf{x})$	Enrichment $\psi(\mathbf{x})$	order of $f_i(\mathbf{x})\times$ $\psi(\mathbf{x})$	Spurious terms
4-node element 1^{st} order	4-node element 1^{st} order	Heaviside zero order	1	No
4-node element 1^{st} order	4-node element 1^{st} order	Ramp 1^{st} order	2	Yes
9-node element 2^{st} order	4-node element 1^{st} order	Ramp 1^{st} order	2	No

Tableau 5.1: A few standard combinations for shape functions, partition of unity and enrichment

Therefore any function Ψ can be reproduced by a set of functions $N_I\Psi$. This is the key property of enriched finite element methods based on a partition of unity. Although one could enrich the entire domain, only a sub-domain is usually enriched since the features need to be modeled local – for instance, a crack compared to the plate containing it. Moreover, keeping enrichment local permits keeping the matrix banded. This is why X-FEM can be considered as *a local partition of unity enriched finite element method*. A partitioning of a typical domain into its non-enriched sub-domains and enriched sub-domains is shown in Figure 5.9. In this local enrichment scheme, three types of elements are distinguished. The first types are the classical finite elements, those in which none of its nodes are enriched, these elements are grouped in Ω^{std}. The second type are fully enriched elements, i.e. all of its nodes are enriched. These

elements are denoted as Ω^{enr}. The third type of elements, called partially-enriched elements, are those for which only some –but not all– of the nodes are enriched. These elements form the blending sub-domain Ω^{blnd} .

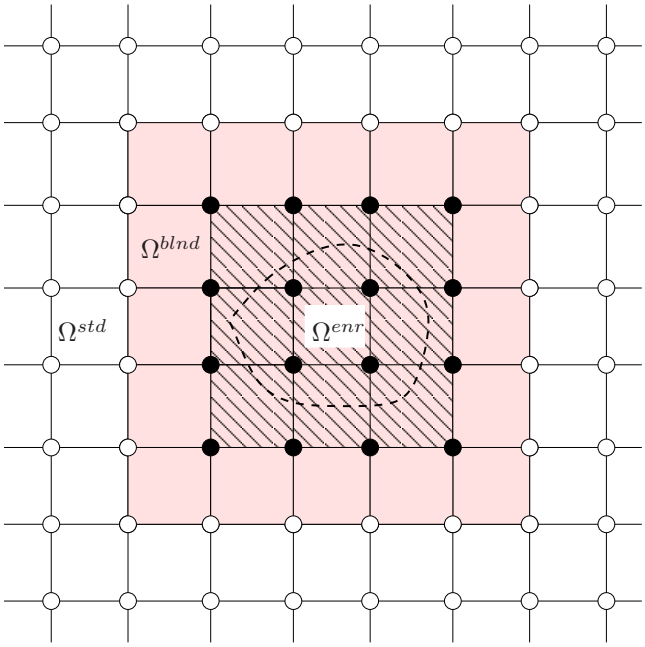

Figure 5.9: Typical discretization illustrating enriched domain Ω^{enr}, transition domain Ω^{blnd} and standard domain Ω^{std}; filled nodes are enriched

Let $\mathbf{u}_I = 0$ and $\mathbf{a}_J = 1$ in the enriched finite element approximation, then we have

$$\mathbf{u}^h(\mathbf{x}) = \sum_{J \in N^{enr}} \begin{cases} \widetilde{N}_J(\mathbf{x})\Psi(\mathbf{x}) = \Psi(\mathbf{x}) & \forall \mathbf{x} \in \Omega^{enr} \\ \widetilde{N}_J(\mathbf{x})\Psi(\mathbf{x}) \neq \Psi(\mathbf{x}) & \forall \mathbf{x} \in \Omega^{blnd} \\ \widetilde{N}_J(\mathbf{x})\Psi(\mathbf{x}) = 0 & \forall \mathbf{x} \in \Omega^{std} \end{cases} \tag{5.52}$$

Therefore the approximation can reproduce the enrichment in Ω^{enr} and it vanishes in Ω^{std}. However, in the blending domain, it consists of the product of a subset of the enriched shape functions $\widetilde{N}_J$ and the enrichment function Ψ so this enrichment function cannot be reproduced. The *blending elements* or *transition elements* lead to a lower convergence rate for enriched finite element methods compared to standard finite element methods. The following example, extracted from [20], shows the reason. Consider a one dimensional mesh as illustrated in Figure 5.10 with a discontinuity in the derivative in element 0. The enrichment function is the ramp function

$$\Psi(\mathrm{x}) = xH(x) \tag{5.53}$$

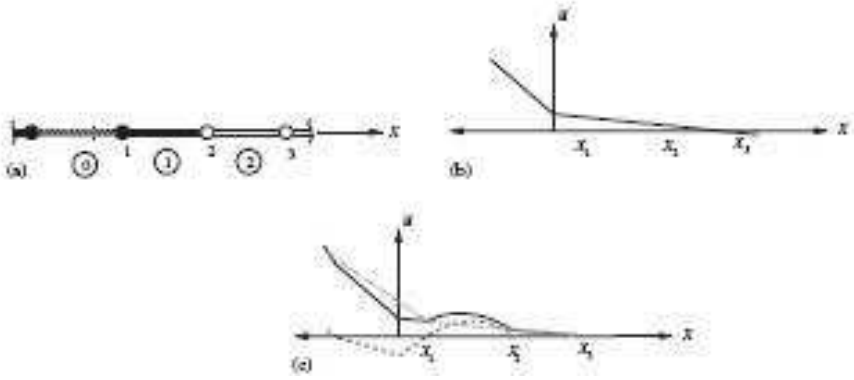

Figure 5.10: A 1D example of how a locally enriched finite element method fails to be able to reproduce a linear field. The desired piecewise linear field is shown in (b) and the enriched part (*dotted line*), standard part (*dashed line*), and the total (*solid line*) approximation are shown in (c). The discretization is shown in (a), where the enriched nodes denoted by filled circles, the two blending elements are filled and the fully enriched element is hashed [20].

where H is the Heaviside step function. This enrichment adds a discontinuity in the gradient of the approximation at $x = 0$. Linear shape functions are used for both the standard approximation and the partition of unity. Let element 0 be the fully enriched element and element 1 be the blending element to the right. The approximation of element 1 is given by

$$\mathbf{u}^h(\mathrm{x}) = \sum_{I=1}^{2} N_I(\mathrm{x}) + N_1(\mathrm{x})(\mathrm{x}H(x) - \mathrm{x}_1 H(x_1))a_1 \tag{5.54}$$

$$\mathbf{u}^h(\xi) = u_1(1-\xi) + u_2\xi + a_1\xi h(1-\xi) \tag{5.55}$$

where

$$\xi = \frac{x - x_1}{h} \tag{5.56}$$

and h is the length of element 1. Let the finite element interpolation to the solution be given by u^h and denote the error in the interpolation by e, we have

$$e \equiv u - u^{int} \tag{5.57}$$

The maximum error occurs at the point $\overline{x}$ where

$$e_{,x|\overline{x}} \equiv \frac{d}{dx} e(\overline{x}) = 0 \tag{5.58}$$

Then a Taylor expansion about $\overline{x}$ gives

$$e(x) = e(\overline{x}) + e_{,x|\overline{x}}(x - \overline{x}) + \frac{1}{2}e_{,xx|\overline{x}}(x - \overline{x})^2 + O(h^3) \tag{5.59}$$

or

$$e(x) = e(\overline{x}) + \frac{1}{2}e_{,xx|\overline{x}}(x - \overline{x})^2 \tag{5.60}$$

If we let $x = x_1$, then $e(x_1) = 0$ since u^h is the finite element interpolation of u, i.e. $u^h(x_I) = u(x_I)$. Therefore, we obtain

$$e(x) = -\frac{1}{2}e_{,xx|\overline{x}}(x - \overline{x})^2 \tag{5.61}$$

Since

$$e(x) = u_{,xx} + \frac{2a_1}{h} \tag{5.62}$$

and since

$$\frac{1}{2}(x - x_1)^2 \leq \frac{1}{8}h^2 \tag{5.63}$$

it follows that

$$e(\overline{x}) \leq \frac{1}{8}h^2 \max(u_{,xx} + \frac{2a_1}{h}) \tag{5.64}$$

The last term, $2a_1/h$, does not appear for standard finite elements. It increases the interpolation error in the blending elements from order h^2 to h. Although this occurs only in few elements, it reduces the rate of convergence of the entire approximation. The reason for this is that the partition of unity property (completeness) of the approximation is not verified in the whole domain. Therefore, the theoretical rate of convergence cannot be attained. When the enrichment is a polynomial of order n, i.e. ξ^n, then for $n > 1$ the interpolation error in the blending elements is increased even further. If we go through the same steps as before, we find that

$$e(\overline{x}) \leq \frac{1}{8}h^2 \max(u_{,xx} + \frac{2a_1}{h^n}) \tag{5.65}$$

At this time, we can understand why in the quadratic XFEM formulation, the partition of unity shape functions have been chosen as linear. To get improved rate of convergence, Chessa proposed the enhanced strain formulation for the blending elements. By properly choosing an enhanced strain field, the undesired terms in the enriched approximation can be eliminated.

5.6 Implementation

The implementation of XFEM will be explained for a 4-node quadrilateral element with linear shape functions, see figure 5.11.

5.6.1 Shape functions

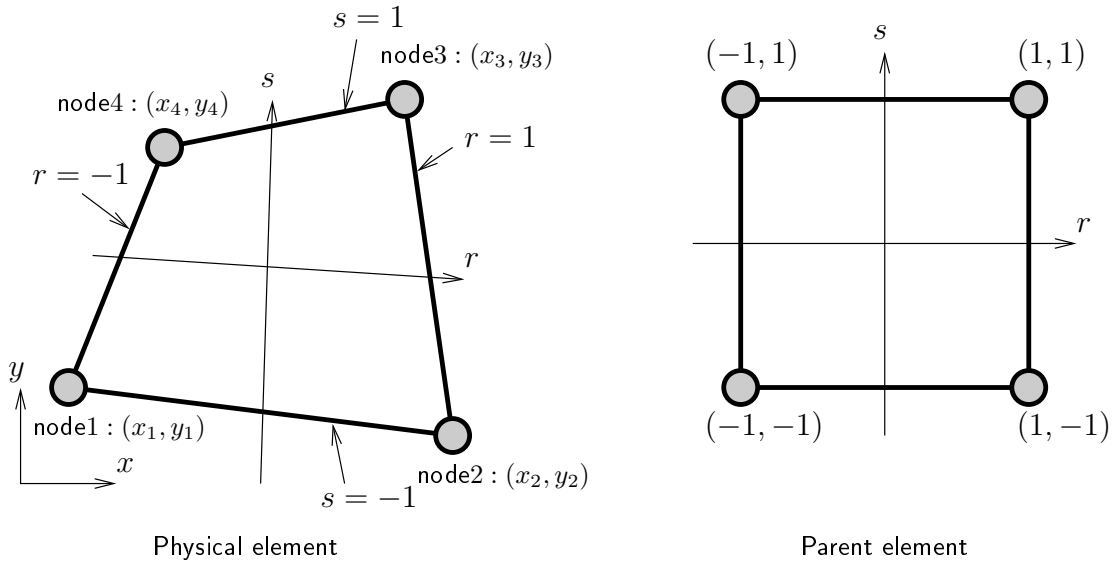

Figure 5.11: Physical and parent 4-node elements

The shape functions $N_I,\ I = 1...4$ are given by:

$$
\begin{aligned}
N_1(r,s) &= \frac{1}{4}(1-r)(1-s) \\
N_2(r,s) &= \frac{1}{4}(1+r)(1-s) \\
N_3(r,s) &= \frac{1}{4}(1+r)(1+s) \\
N_4(r,s) &= \frac{1}{4}(1-r)(1+s)
\end{aligned}
$$

where r and s are scaled coordinates in the parent element, see figure 5.11. The standard finite element approximation of the displacement is

$$
\mathbf{u}^e(M) = \begin{bmatrix} u_x \\ u_y \end{bmatrix} = \begin{bmatrix} N_1 & N_2 & N_3 & N_4 & 0 & 0 & 0 & 0 \\ 0 & 0 & 0 & 0 & N_1 & N_2 & N_3 & N_4 \end{bmatrix} \begin{bmatrix} u_{x_1} \\ u_{x_2} \\ u_{x_3} \\ u_{x_4} \\ u_{y_1} \\ u_{y_2} \\ u_{y_3} \\ u_{y_4} \end{bmatrix} = \mathbf{N}^e_{std}(M)\ \mathbf{q}^e
$$

The enriched finite element approximation of the displacement is

$$\mathbf{u}^e(M) = \begin{bmatrix} u_x \\ u_y \end{bmatrix} = \begin{bmatrix} N_1 & N_2 & N_3 & N_4 & 0 & 0 & 0 & 0 & \cdots \\ 0 & 0 & 0 & 0 & N_1 & N_2 & N_3 & N_4 & \end{bmatrix}$$

$$\cdots \quad \begin{matrix} N_1\psi_1 & N_2\psi_2 & N_3\psi_3 & N_4\psi_4 & 0 & 0 & 0 & 0 \\ 0 & 0 & 0 & 0 & N_1\psi_1 & N_2\psi_2 & N_3\psi_3 & N_4\psi_4 \end{matrix} \begin{bmatrix} u_{x_1} \\ u_{x_2} \\ u_{x_3} \\ u_{x_4} \\ u_{y_1} \\ u_{y_2} \\ u_{y_3} \\ u_{y_4} \\ a_{x_1} \\ a_{x_2} \\ a_{x_3} \\ a_{x_4} \\ a_{y_1} \\ a_{y_2} \\ a_{y_3} \\ a_{y_4} \end{bmatrix}$$

$$\mathbf{u}^e(M) = [\, \mathbf{N}^e_{std}(M) \;\; \mathbf{N}^e_{enr}(M) \,]\, \mathbf{q}^e$$

In other terms, this leads to

$$\mathbf{u}^e(M) = \mathbf{N}^e(M)\, \mathbf{q}^e$$

where $\mathbf{N}^e(M) = [\mathbf{N}^e_{std}(M)\ \mathbf{N}^e_{enr}(M)]$. In this last expression, it is assumed that the 4 nodes of the element are enriched by a single additional function $\psi(\mathbf{x})$ where ψ_I denotes the shifted function:

$$\psi_I(\mathbf{x}) = \psi(\mathbf{x}) - \psi(\mathbf{x}_I)$$

5.6.2 The B-Operator

The strain tensor components in Voigt notation are

$$\boldsymbol{\epsilon} = \begin{bmatrix} \epsilon_{xx} \\ \epsilon_{yy} \\ 2\epsilon_{xy} \end{bmatrix} = \mathbf{D}\mathbf{u}^e(M)$$

with

$$\mathbf{D} = \begin{bmatrix} \dfrac{\partial}{\partial x} & 0 \\ 0 & \dfrac{\partial}{\partial y} \\ \dfrac{\partial}{\partial y} & \dfrac{\partial}{\partial x} \end{bmatrix}$$

By replacing $\mathbf{u}^e(M)$ by its approximated form, it gives

$$\boldsymbol{\epsilon} = \mathbf{D}\mathbf{N}^e(M)\, \mathbf{q}^e = \mathbf{B}^e(M)\, \mathbf{q}^e$$

where $\mathbf{B}^e(M)$ is the discretized gradient operator. It contains both the standard part and the enriched part and it can be written as

$$\mathbf{B}^e(M) = [\mathbf{B}^e_{std}(M)\ \mathbf{B}^e_{enr}(M)]$$

In the last expression, the discretized gradient operator $\mathbf{B}^e_{std}(M)$ is equal to:

$$\mathbf{B}^e_{std} = \begin{bmatrix} N_{1,x} & N_{2,x} & N_{3,x} & N_{4,x} & 0 & 0 & 0 & 0 \\ 0 & 0 & 0 & 0 & N_{1,y} & N_{2,y} & N_{3,y} & N_{4,y} \\ N_{1,y} & N_{2,y} & N_{3,y} & N_{4,y} & N_{1,x} & N_{2,x} & N_{3,x} & N_{4,x} \end{bmatrix}$$

and the enriched discretized gradient operator $\mathbf{B}^e_{enr}(M)$ is equal to

$$\mathbf{B}^e_{enr} = \begin{bmatrix} (N_1\psi_1)_{,x} & (N_2\psi_2)_{,x} & (N_3\psi_3)_{,x} & (N_4\psi_4)_{,x} & 0 & 0 & 0 & 0 \\ 0 & 0 & 0 & 0 & (N_1\psi_1)_{,y} & (N_2\psi_2)_{,y} & (N_3\psi_3)_{,y} & (N_4\psi_4)_{,y} \\ (N_1\psi_1)_{,y} & (N_2\psi_2)_{,y} & (N_3\psi_3)_{,y} & (N_4\psi_4)_{,y} & (N_1\psi_1)_{,x} & (N_2\psi_2)_{,x} & (N_3\psi_3)_{,x} & (N_4\psi_4)_{,x} \end{bmatrix}$$

In the case of an **Heaviside enrichment**, the derivative of the approximation can be written as

$$\begin{aligned} \mathbf{u}^h_{i,j} &= \sum_{I\in\mathcal{S}} N_{J,i}(\mathbf{x})\ u_{jJ} + \sum_{I\in\mathcal{S}} \left(N_J(\mathbf{x})H(\phi(\mathbf{x}))\right)_{,i} a_{jJ} \\ &= \sum_{I\in\mathcal{S}} N_{J,i}(\mathbf{x})\ u_{jJ} + \sum_{I\in\mathcal{S}} \left(N_{J,i}(\mathbf{x})H(\phi(\mathbf{x})) + N_J(\mathbf{x})H_{,i}(\phi(\mathbf{x}))\right) a_{jJ} \end{aligned}$$

The derivatives of the Heaviside is the dirac delta function $H_{,i}(\phi(\mathbf{x})) = \boldsymbol{\delta}$. That means that $H_{,i} = 1$ at the crack interface and $H_{,i} = 0$ otherwise. If we assume the crack to be traction-free, we can omit the derivatives of the Heaviside function and can give the enriched B-operator as

$$\mathbf{B}^e_{enr} = \begin{bmatrix} N_{1,x}\psi_1 & N_{2,x}\psi_2 & N_{3,x}\psi_3 & N_{4,x}\psi_4 & 0 & 0 & 0 & 0 \\ 0 & 0 & 0 & 0 & N_{1,y}\psi_1 & N_{2,y}\psi_2 & N_{3,y}\psi_3 & N_{4,y}\psi_4 \\ N_{1,x}\psi_1 & N_{2,x}\psi_2 & N_{3,x}\psi_3 & N_{4,x}\psi_4 & N_{1,y}\psi_1 & N_{2,y}\psi_2 & N_{3,y}\psi_3 & N_{4,y}\psi_4 \end{bmatrix}$$

In the case of a **ramp enrichment**, $\psi(\mathbf{x}) = |\phi(\mathbf{x})|$, the computation of the derivative of $\psi(\mathbf{x})$ is needed:

$$\Big(\psi(\mathbf{x})\Big)_{,i} = \text{sign}(\phi(\mathbf{x}))\ \phi_{,i}(\mathbf{x})$$

The derivative of $\phi(\mathbf{x})$ is then needed. Since

$$\phi(\mathbf{x}) = [\ N_1\ \ N_2\ \ N_3\ \ N_4\ ] \begin{bmatrix} \phi_1 \\ \phi_2 \\ \phi_3 \\ \phi_4 \end{bmatrix}$$

the derivative according to x is

$$\phi(\mathbf{x})_{,x} = [\ N_{1,x}\ \ N_{2,x}\ \ N_{3,x}\ \ N_{4,x}\ ] \begin{bmatrix} \phi_1 \\ \phi_2 \\ \phi_3 \\ \phi_4 \end{bmatrix}$$

and the derivative according to y is

$$\phi(\mathbf{x})_{,y} = \begin{bmatrix} N_{1,y} & N_{2,y} & N_{3,y} & N_{4,y} \end{bmatrix} \begin{bmatrix} \phi_1 \\ \phi_2 \\ \phi_3 \\ \phi_4 \end{bmatrix}$$

5.6.3 The element stiffness matrix

The previous computations involve the derivative of the shape functions in terms of the physical coordinates. The relations between the derivative in the parent and in the physical coordinates are

$$\begin{aligned} \frac{\partial N_I}{\partial x} &= \frac{\partial N_I}{\partial r}\frac{\partial r}{\partial x} + \frac{\partial N_I}{\partial s}\frac{\partial s}{\partial x} \\ \frac{\partial N_I}{\partial y} &= \frac{\partial N_I}{\partial r}\frac{\partial r}{\partial y} + \frac{\partial N_I}{\partial s}\frac{\partial s}{\partial y} \end{aligned}$$

which can be written, for each function N_I:

$$\begin{bmatrix} N_{,x} & N_{,y} \end{bmatrix} = \begin{bmatrix} N_{,r} & N_{,s} \end{bmatrix} \underbrace{\begin{bmatrix} \dfrac{\partial r}{\partial x} & \dfrac{\partial r}{\partial y} \\ \dfrac{\partial s}{\partial x} & \dfrac{\partial s}{\partial y} \end{bmatrix}}_{= \mathbf{J^{-1}}}$$

where $\mathbf{J}$ is the Jacobian. The derivatives of the functions $N_I(r,s)$ in terms of the parent coordinates r and s are:

$$\begin{aligned} N_{1,r} &= -\frac{1}{4}(1-s) & N_{1,s} &= -\frac{1}{4}(1-r) \\ N_{2,r} &= \frac{1}{4}(1-s) & N_{2,s} &= -\frac{1}{4}(1+r) \\ N_{3,r} &= \frac{1}{4}(1+s) & N_{3,s} &= \frac{1}{4}(1+r) \\ N_{4,r} &= -\frac{1}{4}(1+s) & N_{4,s} &= \frac{1}{4}(1-r) \end{aligned}$$

The expression of the Jacobian is

$$\mathbf{J} = \begin{bmatrix} \dfrac{\partial x}{\partial r} & \dfrac{\partial x}{\partial s} \\ \dfrac{\partial y}{\partial r} & \dfrac{\partial y}{\partial s} \end{bmatrix}$$

with

$$x = \sum_{I=1}^{4} N_I x_I \quad , \quad \frac{\partial x}{\partial r} = \sum_{I=1}^{4} \frac{\partial N_I}{\partial r} x_I \quad , \quad \frac{\partial x}{\partial s} = \sum_{I=1}^{4} \frac{\partial N_I}{\partial s} x_I$$

which is also

$$\frac{\partial x}{\partial r} = \left[\begin{array}{cccc} N_{1,r} & N_{2,r} & N_{3,r} & N_{4,r} \end{array} \right] \left[\begin{array}{c} x_1 \\ x_2 \\ x_3 \\ x_4 \end{array} \right]$$

$$\frac{\partial x}{\partial s} = \left[\begin{array}{cccc} N_{1,s} & N_{2,s} & N_{3,s} & N_{4,s} \end{array} \right] \left[\begin{array}{c} x_1 \\ x_2 \\ x_3 \\ x_4 \end{array} \right]$$

and

$$y = \sum_{I=1}^{4} N_I y_I \quad , \quad \frac{\partial y}{\partial r} = \sum_{I=1}^{4} \frac{\partial N_I}{\partial r} y_I \quad , \quad \frac{\partial y}{\partial s} = \sum_{I=1}^{4} \frac{\partial N_I}{\partial s} y_I$$

which is also

$$\frac{\partial y}{\partial r} = \left[\begin{array}{cccc} N_{1,r} & N_{2,r} & N_{3,r} & N_{4,r} \end{array} \right] \left[\begin{array}{c} y_1 \\ y_2 \\ y_3 \\ y_4 \end{array} \right]$$

$$\frac{\partial y}{\partial s} = \left[\begin{array}{cccc} N_{1,s} & N_{2,s} & N_{3,s} & N_{4,s} \end{array} \right] \left[\begin{array}{c} y_1 \\ y_2 \\ y_3 \\ y_4 \end{array} \right]$$

The expression of the stiffness matrix for an enriched element is

$$\mathbf{K}^e = \int_{\Omega^e} \mathbf{B}^{e^T}(M)\ \mathbf{C}^e\ \mathbf{B}^e(M)\ \mathrm{d}\Omega = \int_{-1}^{1}\int_{-1}^{1} \mathbf{B}^{e^T}(r,s)\ \mathbf{C}^e\ \mathbf{B}^e(r,s)\ \det \mathbf{J}\ \mathrm{d}r\ \mathrm{d}s$$

where $\mathbf{C}^e$ is the constitutive tangent operator. The stiffness matrix can be decomposed into four 8×8 blocks:

$$\mathbf{K}_l^e = \left[\begin{array}{cc} \displaystyle\int_{\Omega^e} \mathbf{B}_{std}^{e^T}(M)\mathbf{C}^e\mathbf{B}_{std}^e(M) & \displaystyle\int_{\Omega^e} \mathbf{B}_{std}^{e^T}(M)\mathbf{C}^e\mathbf{B}_{enr}^e(M) \\ \displaystyle\int_{\Omega^e} \mathbf{B}_{enr}^{e^T}(M)\mathbf{C}^e\mathbf{B}_{std}^e(M) & \displaystyle\int_{\Omega^e} \mathbf{B}_{enr}^{e^T}(M)\mathbf{C}^e\mathbf{B}_{enr}^e(M) \end{array} \right]$$

The up-left block corresponds to the standard stiffness matrix. The elemental enriched stiffness matrix has a 16×16 size.

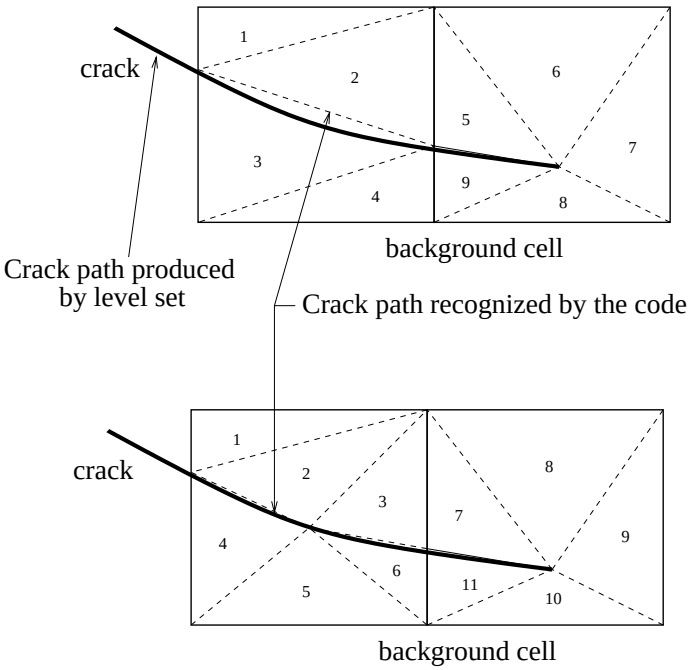

Figure 5.12: Sub-triangulation of finite elements

5.7 Integration

Numerical integration is the last step to obtain the discrete equations. In FEM, Gauss quadrature is usually applied. However, standard Gauss quadrature cannot be used if the element is crossed by a discontinuity. One integration strategy is based on sub-dividing an existing elements into several smaller triangular elements as shown in figure 5.12 for the 2D case. Difficulties occur for high curvatures of interface ϕ. For example: Consider linear finite elements. If an interface severely curves as shown for the two dimensional case in figure 5.12 and the interface is discretized with level sets where for the discretization of the level set, the linear FE shape functions are used, then the level set cannot capture the curvature of the crack correctly. Therefore, an additional node is introduced to maintain the accuracy of the integration. Adding one more point, the error is reduced second order small.

After the element with the interface is sub-triangulated, the integration of a function $\mathcal{F}$ can be done as follows:

$$\begin{aligned} \mathcal{F} &= \int_{\Omega^-} \mathcal{F}(\mathbf{X}) d\Omega + \int_{\Omega^+} \mathcal{F}(\mathbf{X}) d\Omega \\ &= \int_{\bar{\Omega}^-} \mathcal{F}(\mathbf{X}(\boldsymbol{\xi}))\ \mathrm{det}\mathbf{J}^-(\boldsymbol{\xi}) d\Omega + \int_{\bar{\Omega}^+} \mathcal{F}(\mathbf{X}(\boldsymbol{\xi}))\ \mathrm{det}\mathbf{J}^+(\boldsymbol{\xi})\ d\Omega \end{aligned} \quad (5.66)$$

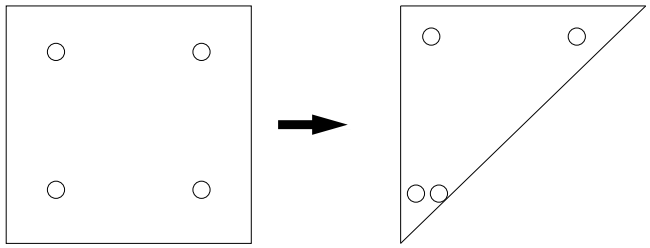

Figure 5.13: Transformation of an integration method on a square into an integration method on a triangle for crack tip functions

where the Jacobian maps the domains $\bar{\Omega}^{\pm}$ onto $\Omega^{\pm}$. With the mapping $\tilde{\Omega}^{\pm} \rightarrow \bar{\Omega}^{\pm}$, we finally obtain:

$$\begin{aligned} \mathcal{F} &= \int_{\tilde{\Omega}^-} \mathcal{F}(\mathbf{X}(\boldsymbol{\xi})(\boldsymbol{\eta}))\ \mathrm{det}\mathbf{J}^-(\boldsymbol{\xi}(\boldsymbol{\eta}))\ \mathrm{det}\bar{\mathbf{J}}^-(\boldsymbol{\eta})d\Omega \\ &+ \int_{\tilde{\Omega}^+} \mathcal{F}(\mathbf{X}(\boldsymbol{\xi})(\boldsymbol{\eta}))\ \mathrm{det}\mathbf{J}^+(\boldsymbol{\xi}(\boldsymbol{\eta}))\ \mathrm{det}\bar{\mathbf{J}}^+(\boldsymbol{\eta})d\Omega \end{aligned} \tag{5.67}$$

and in its discrete form using Gauss quadrature:

$$\mathcal{F} = \sum_{I=1}^{n_{GP}^-} \mathcal{F}(\boldsymbol{\eta}_I)\ \mathrm{det}\mathbf{J}^-(\boldsymbol{\eta})\ \mathrm{det}\bar{\mathbf{J}}^-(\boldsymbol{\eta})w_I + \sum_{I=1}^{n_{GP}^+} \mathcal{F}(\boldsymbol{\eta}_I)\ \mathrm{det}\mathbf{J}^+(\boldsymbol{\eta})\ \mathrm{det}\bar{\mathbf{J}}^+(\boldsymbol{\eta})w_I \tag{5.68}$$

where n_{GP}^- and n_{GP}^+ are the Gauss points in Ω^- and Ω^+, respectively, and $\boldsymbol{\eta}$ are the local coordinates of the Gauss points and w_I are their quadrature weights.

An alternative approach is the modification of the quadrature weights, that is illustrated in figure 5.14. In that method, the quadrature weights crossed by the crack are computed according to their areas A^+ and A^-:

$$\begin{aligned} w_I^+ &= w\frac{A_I^+}{A_I} \\ w_I^- &= w\frac{A_I^-}{A_I} \end{aligned} \tag{5.69}$$

The method requires subdivision of the element; we note that a certain number of Gauss points are needed in order to obtain accurate results.

In crack problems, it is preferable to have an accurate stress field around the crack tip in order to model the propagation of the crack as accurate as possible. In a sub-triangulation procedure, state variables have to be mapped from the original Gauss points to the new Gauss points generated by the sub-triangulation procedure *at the time* the crack enters the element. Therefore, it is preferable to use the second approach with higher numbers of Gauss points adjacent to crack-tip elements. The mapping is then done *before* the crack approaches the element that will be cracked.

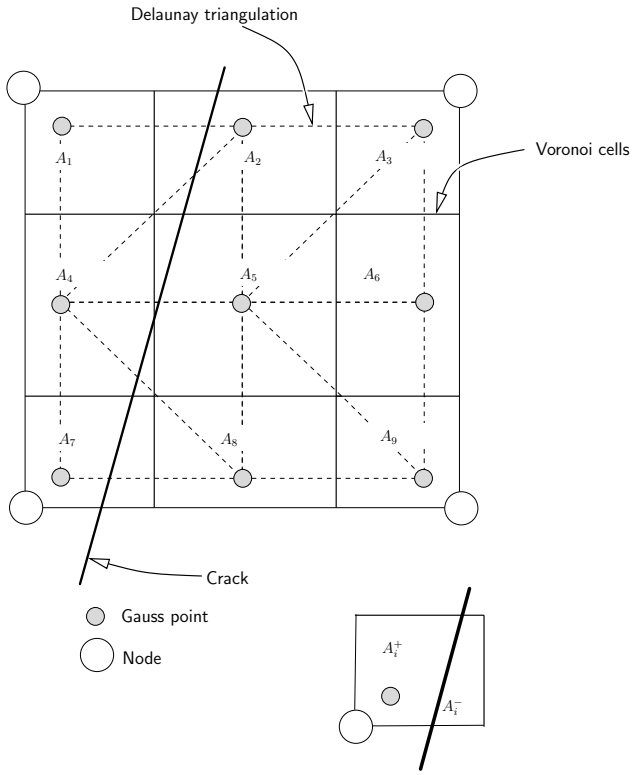

Figure 5.14: Integration with modified quadrature weights

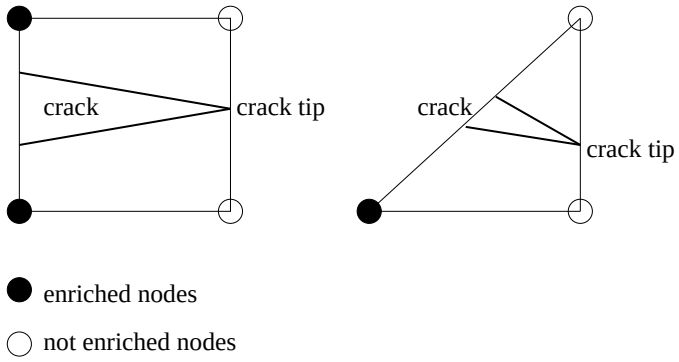

Figure 5.15: One opportunity to close the crack in XFEM

Remark: In LEFM, the elements that contain the crack tip do not only have a discontinuity but also a singularity at the crack tip. Hence, a sub-triangulation procedure might not be accurate enough if Gauss points of the sub-triangles are close to the stress singularity. This drawback can be circumvented by expressing the elementary integrals of the type

$$\int \nabla \left(F_j \psi_i\right) \cdot \nabla \left(F_l \psi_k\right) \, dx \tag{5.70}$$

in polar coordinates that will remove the $r^{-0.5}$ singularity of ∇F_i. The geometric transformation

$$\mathcal{G} : \left\{ \begin{array}{c} x \\ y \end{array} \right\} \leftarrow \left\{ \begin{array}{c} x \; y \\ y \end{array} \right\} \tag{5.71}$$

maps the unit square onto a triangle, see figure 5.13. With this transformation, it is possible to build a quadrature rule on the triangle from a quadrature rule on the unit square. The new integration points $\bar{\xi}$ and their weights $\bar{w}$ are obtained from those of the original quadrature rule with

$$\bar{\xi} = \mathcal{G}(\xi) \quad , \bar{w} = w \, \det(\nabla \mathcal{G}) \tag{5.72}$$

5.8 Application of XFEM to LEFM

5.8.1 Governing equations

The governing equation is the equation of equilibrium:

$$\nabla_0 \cdot \mathbf{P} - \mathbf{b} = \emptyset \;\; \forall \mathbf{X} \in \Omega_0 \setminus \Gamma_0^c \tag{5.73}$$

The boundary conditions are

$$\mathbf{u}(\mathbf{X}, t) = \bar{\mathbf{u}}(\mathbf{X}, t) \quad \text{on} \quad \Gamma_0^u \tag{5.74}$$

$$\mathbf{n}_0 \cdot \mathbf{P}(\mathbf{X}, t) = \bar{\mathbf{t}}_0(\mathbf{X}, t) \quad \text{on} \quad \Gamma_0^t \tag{5.75}$$

$$\mathbf{n}_0 \cdot \mathbf{P}(\mathbf{X}, t) = 0 \quad \text{on} \quad \Gamma_0^c \tag{5.76}$$

where $\bar{\mathbf{u}}$ and $\bar{\mathbf{t}}_0$ are the prescribed displacements and tractions, respectively and Γ_0^c is the crack surface with $\Gamma_0^u \bigcup \Gamma_0^t \bigcup \Gamma_0^c = \Gamma_0$, $(\Gamma_0^u \bigcap \Gamma_0^t) \bigcup (\Gamma_0^t \bigcap \Gamma_0^c) \bigcup (\Gamma_0^u \bigcap \Gamma_0^c) = \emptyset$. We assume that the crack surfaces are traction-free, see eq. (5.76).

5.8.2 Weak form

The weak form of the equilibrium equation is given by: find $\mathbf{u} \in \mathcal{V}$ such that

$$\delta W = \delta W_{int} - \delta W_{ext} = 0 \ \ \forall \delta \mathbf{u} \tag{5.77}$$

where

$$\delta W_{int} = \int_{\Omega_0} (\nabla \otimes \delta \mathbf{u})^T : \mathbf{P} \ d\Omega_0 \tag{5.78}$$

$$\delta W_{ext} = \int_{\Omega_0} \delta \mathbf{u} \cdot \mathbf{b} \ d\Omega_0 + \int_{\Gamma_0^t} \delta \mathbf{u} \cdot \bar{\mathbf{t}}_0 \ d\Gamma_0 \tag{5.79}$$

where

$$\begin{aligned} \mathcal{V} &= \left\{ \mathbf{u}(\cdot, t) | \mathbf{u}(\cdot, t) \in \mathcal{H}^1, \ \ \mathbf{u}(\cdot, t) = \bar{\mathbf{u}}(t) \text{ on } \Gamma_0^u, \ \ \mathbf{u} \text{ discontinuous on } \Gamma_0^c \right\} \\ \mathcal{V}_0 &= \left\{ \delta \mathbf{u} | \delta \mathbf{u} \in \mathcal{H}^1, \ \ \delta \mathbf{u} = 0 \text{ on } \Gamma_0^u, \ \ \delta \mathbf{u} \text{ discontinuous on } \Gamma_0^c \right\} \end{aligned} \tag{5.80}$$

In the static case, the solution of a boundary value problem (BVP) with internal boundaries is to be sought in the so-called *Space of Bounded Deformations*.

5.8.3 XFEM approximation for cracks

The application of XFEM to cracks poses additional challenges onto the method:

- It has to be ensured that the crack closes at its crack tip.
- During a loading cycle, a crack can open and close. It has to be ensured that the two crack surfaces do not overlap.
- While in fluid-fluid or fluid-structure interaction problems, the interface is given at the beginning of the computation, cracks can be initiated at any time during a loading cycle. Hence, we need also a criterion that tells us when a crack is initiated, how the crack will be oriented and how the shape of the crack looks like, e.g. how long is the crack?
- Crack path tracking algorithms are more complex than interface tracking algorithms in two-phase flow or fluid-structure interaction problems.

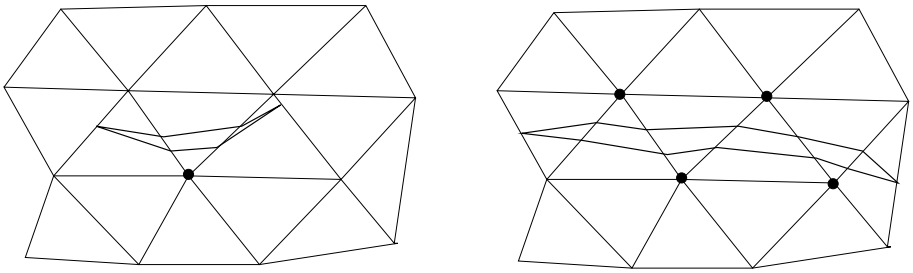

Figure 5.16: Example of enriched nodes when crack closure is realized by closing the crack tip at the element sides

We will discuss these aspects only for a single crack. Moreover, we consider two dimensional triangular and quadrilateral finite elements with linear shape functions. The crack line is approximated with level sets where the level set is discretized with the same shape functions as the mechanical properties. Hence, the curvature of the crack can be maximal bi-linear for the quadrilateral element and linear for the triangular element. We don't consider geometrical and material non-linearities. For now, we assume that the crack does not propagate and study only the crack kinematics. The subsequent issues will be discussed in the following sections.

The Heaviside enrichment is able to capture the jump in the displacement field. However, it does not necessarily guarantee the closure of the crack at its crack tip. The simplest possibility to ensure crack closure at the crack tip is to locate the crack tip at one of the element edges and not to enrich the adjacent nodes, see figure 5.15. Two potential crack pathes including the enriched nodes are illustrated in figure 5.16. The black dots denote the enriched nodes. The standard nodes are not shown. This kind of crack closure has the drawbacks that the crack length is governed by the element size since it is required to grow the crack through the entire element. Another opportunity is to close the crack within an element. However, the enrichment procedure has to be modified. Therefore, let us consider a triangular element as shown on the RHS in figure 5.17. The crack is assumed to pass through the side $\overline{23}$ and intersect side $\overline{12}$. Other relationships can be obtained by permuting the node numbers. Due to compatibility, the enrichment has to vanish on the sides $\overline{12}$ and $\overline{13}$ and is continuous across $\overline{23}$ with the field in the adjacent element. To meet this condition, only node 3 is enriched and the discontinuous displacement field in the tip element is

$$\mathbf{u}_{disc} = \boldsymbol{\xi}_3^* \; \Psi_3(\boldsymbol{\xi}^*) \; \mathbf{a}_3 \tag{5.81}$$

where $\boldsymbol{\xi}^* = [\xi_1^* \; \xi_2^* \; \xi_3^*]$ are the parent coordinates of the sub-triangle $\overline{23P}$ in figure 5.17. The shaded parent area coordinates are related by $\xi_3^* = 1 - \xi_1^* - \xi_2^*$ and $\Psi_3(\boldsymbol{\xi}^*) = \text{sign}\,(\phi(\boldsymbol{\xi}^*)) - \text{sign}\,(\phi_3)$. The relation between $\boldsymbol{\xi}^*$ and $\boldsymbol{\xi}$ is given

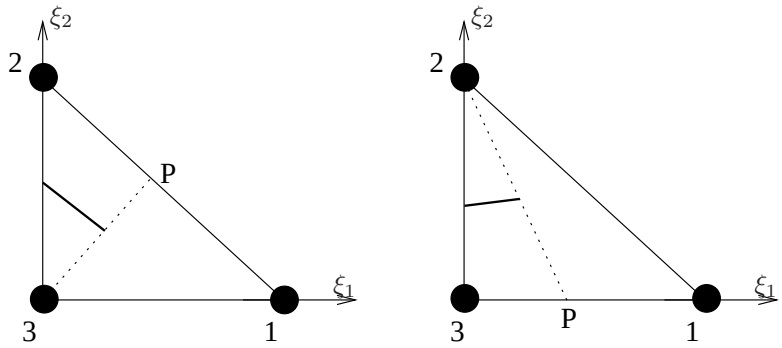

$$N_3(\boldsymbol{\xi}) = 1 - \xi_1 - \xi_2$$
$$N_1(\boldsymbol{\xi}) = \xi_1$$
$$N_2(\boldsymbol{\xi}) = \xi_2$$

Figure 5.17: XFEM enrichment for a crack tip that ends in an element

by

$$\xi_1^* = \frac{\xi_1}{\xi_{1P}}, \quad \xi_2^* = \xi_2 \tag{5.82}$$

where ξ_{1P} is the area coordinate of point P. When the direction of the crack intersects side $\overline{31}$, see the LHS of figure 5.17, then the discontinuous part of the displacement field is

$$\mathbf{u}_{disc} = \boldsymbol{\xi}_2^* \; \Psi_2(\boldsymbol{\xi}^*) \; \mathbf{a}_2 \tag{5.83}$$

with

$$\xi_1^* = \xi_1 - \frac{\xi_{1P}}{\xi_{2P}}\xi_2, \quad \xi_2^* = \frac{\xi_2}{\xi_{2P}} \tag{5.84}$$

and $\Psi_2(\boldsymbol{\xi}^*) = \text{sign}\,(\phi(\boldsymbol{\xi}^*)) - \text{sign}\,(\phi_2)$ and $\mathbf{a}_3 = \mathbf{a}_P = 0$. The enrichment can be implemented easier by letting

$$\mathbf{u}_{disc} = \sum_I \boldsymbol{\xi}_I^* \; \Psi_I(\boldsymbol{\xi}^*) \; \mathbf{a}_I \tag{5.85}$$

and constructing $\mathbf{a}_I$ to vanish for the nodes on the edge towards which the crack is heading. These enrichment displacements $\mathbf{u}_{disc}$ vanish on the boundary of Ω_{enr}. Hence, only the elements in Ω_{enr} need a special treatment of the same type. This is a partition of unity in Ω_{enr} and there is no inner blending between different enrichments. Moreover, since the enrichment vanishes on the boundary of Ω_{enr}, blending outside the enriched subdomain does not occur. Thus, although it is a local partition of unity, it is indistinguishable from a global partition of unity.

Another opportunity to close the crack is by use of branch functions $\mathbf{B}$. In fact, the branch functions were already introduced in section 4.2 where the

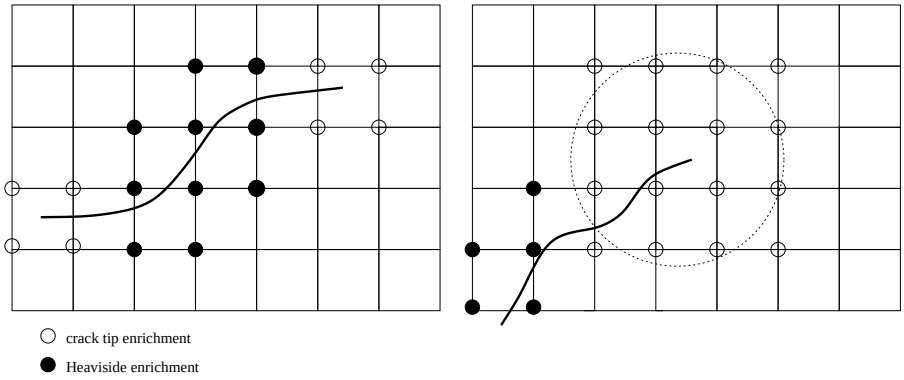

Figure 5.18: Crack with enriched elements

concept of enrichment was discussed:

$$\begin{aligned} \mathbf{B} &= [B_1\ B_2\ B_3\ B_4] \\ &= \left[\sqrt{r}\,\sin\frac{\theta}{2}, \sqrt{r}\,\cos\frac{\theta}{2}, \sqrt{r}\,\sin\frac{\theta}{2}\sin(\theta), \sqrt{r}\,\cos\frac{\theta}{2}\sin(\theta)\right] \end{aligned} \tag{5.86}$$

Here, we will denote the branch functions[6] with $\mathbf{B}$ according to the LEFM literature. It is obvious that for $r = 0$, the crack closes at the crack tip. Moreover, the solution will be more accurate since we put the information of the analytical solution into our approximation. The approximation of the displacement field is now given by:

$$\begin{aligned} \mathbf{u}^h(\mathbf{X}) &= \sum_{I\in\mathcal{S}} N_I(\mathbf{X})\ \mathbf{u}_I + \sum_{I\in\mathcal{S}_c(\mathbf{X})} N_I(\mathbf{X})\ \bar{H}(f_I(\mathbf{X}))\ \mathbf{a}_I \\ &+ \sum_{I\in\mathcal{S}_t(\mathbf{X})} N_I(\mathbf{X})\ \sum_K \bar{\mathbf{B}}_K(\mathbf{X})\ \mathbf{b}_{KI} \end{aligned} \tag{5.87}$$

where $\mathcal{S}_t$ are the set of nodes that are influenced by the crack tip and the superimposed bar denotes a shifting as described in section 5.3.1. The first term on the RHS of eq. (5.87) is the standard approximation, the second term and the third term is the enrichment, see also figure 5.18. Generally, only the element containing the crack tip is enriched with the branch functions $\mathbf{B}$. However, this is not mandatory. It is also possible to enrich adjacent elements as shown on the RHS of figure 5.18.

Finally, we would like to mention the special case, where a crack is located close to a node[7] as shown in figure 5.19. Therefore, let us consider the element spanned by the nodes a, b, c, d. The support of the node is defined by its adjacent neighbor elements. Node a for example has four neighboring elements.

[6] In section 4.2, the branch functions were denoted with $\mathbf{p}$

[7] The node cannot be enriched with a crack tip enrichment

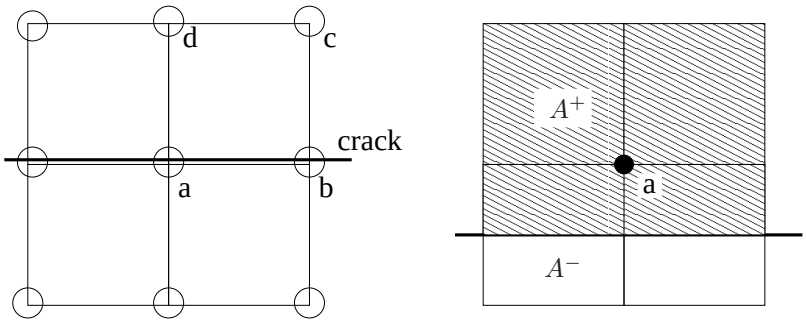

Figure 5.19: Enrichment criteria for cracks that are close to a node

Hence, the support size is equal to the area of these four neighboring finite elements. Let us define the parameters r^+ and r^- between the area on both sides of the crack and the total area of the support:

$$r^+ = \frac{A^+}{A^+ + A^-}, \quad r^- = \frac{A^-}{A^+ + A^-} \tag{5.88}$$

If one of these ratios is smaller than a given threshold, the support node is no longer enriched. In the case of our element a, b, c, d, only nodes a and b will be enriched.

5.8.4 Discrete equations

To obtain the discrete equations, the test and trial functions have to be substituted into the weak form of the equilibrium equation (5.77). We will consider the approximation with crack tip enrichment as defined in eq. (5.87). The approximation of the test functions look identical. Then we obtain the final system of equations:

$$\begin{bmatrix} \mathbf{K}_{IJ}^{uu} & \mathbf{K}_{IJ}^{ua} & \mathbf{K}_{IJK}^{ub} \\ \mathbf{K}_{IJ}^{au} & \mathbf{K}_{IJ}^{aa} & \mathbf{K}_{IJK}^{ab} \\ \mathbf{K}_{IJK}^{bu} & \mathbf{K}_{IJK}^{ba} & \mathbf{K}_{IJK}^{bb} \end{bmatrix} \begin{Bmatrix} \mathbf{u}_J \\ \mathbf{a}_J \\ \mathbf{b}_{JK} \end{Bmatrix} = \begin{Bmatrix} \mathbf{f}_I^{ext} \\ \mathbf{f}_I^{ext} \\ \mathbf{f}_{IK}^{ext} \end{Bmatrix} \tag{5.89}$$

or

$$\mathbf{K}\ \mathbf{d} = \mathbf{f}^{ext} \tag{5.90}$$

where $\mathbf{K}$ is the stiffness matrix, $\mathbf{d} = \{\mathbf{u}\ \mathbf{a}\ \mathbf{b}\}^T$ is the vector with the nodal parameters, $\mathbf{f}^{ext} = \left\{\mathbf{f}^u\ \mathbf{f}^a\ \mathbf{f}^b\right\}^T$ is the external force vector with $\mathbf{f}^b = \left\{\mathbf{f}^{b1}\ \mathbf{f}^{b2}\ \mathbf{f}^{b3}\ \mathbf{f}^{b4}\right\}$ and

$$\mathbf{f}_I^u = \int_\Omega N_I\ \mathbf{b}\ d\Omega + \int_{\Gamma^t} N_I\ \bar{\mathbf{t}}\ d\Gamma \tag{5.91}$$

$$\mathbf{f}_I^a = \int_\Omega N_I\ (H(\phi(\mathbf{X})) - H(\phi(\mathbf{X}_I)))\ \mathbf{b}\ d\Omega + \int_{\Gamma^t} N_I\ (H(\phi(\mathbf{X})) - H(\phi(\mathbf{X}_I)))\ \bar{\mathbf{t}}\ d\Gamma \tag{5.92}$$

$$\mathbf{f}_I^{bl} = \int_\Omega N_I \ \left(B_I^l(\mathbf{X}) - B_I^l(\mathbf{X}_I)\right) \ \mathbf{b} \ d\Omega + \int_{\Gamma^t} N_I \ \left(B_I^l(\mathbf{X}) - B_I^l(\mathbf{X}_I)\right) \ \bar{\mathbf{t}} \ d\Gamma \quad (5.93)$$

The stiffness matrix is

$$\mathbf{K} = \int_\Omega \bar{\mathbf{B}}^T \ \mathbf{C} \ \bar{\mathbf{B}} \ d\Omega \quad (5.94)$$

where $\bar{\mathbf{B}}$ is the B-operator defined by:

$$\mathbf{B}_I^u = \begin{bmatrix} N_{I,X} & 0 \\ 0 & N_{I,Y} \\ N_{I,Y} & N_{I,X} \end{bmatrix} \quad (5.95)$$

$$\mathbf{B}_I^a = \begin{bmatrix} N_{I,X} \ (H(\phi(\mathbf{X})) - H(\phi(\mathbf{X}_I))) & 0 \\ 0 & N_{I,Y} \ (H(\phi(\mathbf{X})) - H(\phi(\mathbf{X}_I))) \\ N_{I,Y} \ (H(\phi(\mathbf{X})) - H(\phi(\mathbf{X}_I))) & N_{I,X} \ (H(\phi(\mathbf{X})) - H(\phi(\mathbf{X}_I))) \end{bmatrix} \quad (5.96)$$

$$\mathbf{B}_I^{bl}|_{l=1,2,3,4} = \begin{bmatrix} \left[N_I \ \left(B_K^l(\mathbf{X}) - B_K^l(\mathbf{X}_I)\right)\right]_{,X} & 0 \\ 0 & \left[N_I \ \left(B_K^l(\mathbf{X}) - B_K^l(\mathbf{X}_I)\right)\right]_{,Y} \\ \left[N_I \ \left(B_K^l(\mathbf{X}) - B_K^l(\mathbf{X}_I)\right)\right]_{,Y} & \left[N_I \ \left(B_K^l(\mathbf{X}) - B_K^l(\mathbf{X}_I)\right)\right]_{,X} \end{bmatrix} \quad (5.97)$$

In eq. (5.96), we have already omitted the derivatives of the Heaviside function, see section 5.6.2. The partial derivatives for the branch function are

$$\left[N_I \ B_K^l(\mathbf{X})\right]_{,i} = N_{I,i} \ B_K^l(\mathbf{X}) + N_I \ B_K^l(\mathbf{X})_{,i} \quad (5.98)$$

To obtain the derivatives of the branch functions, let us define a local crack coordinate system, see figure 5.20. The angle α denotes the slope of the local crack coordinate system with respect to the global coordinate system. The derivatives of the branch functions in the local crack coordinate system are

$$B_{,\bar{i}}^l = B_{,r}^l \ r_{,\bar{i}} + B_{,\theta}^l \ \theta_{,\bar{i}} \quad (5.99)$$

where θ and r are defined in figure 4.6 and the subscript "$,\bar{i}$" denotes derivatives with respect to the local crack coordinate system. The terms $B_{,r}^l$ and $B_{,\theta}^l$ are obtained by formal differentiation:

$$B_{,r}^1 = \frac{\sin(\theta/2)}{2\sqrt{2}} \quad B_{,\theta}^1 = \frac{\sqrt{2}\cos(\theta/2)}{2}$$

$$B_{,r}^2 = \frac{\cos(\theta/2)}{2\sqrt{2}} \quad B_{,\theta}^2 = -\frac{\sqrt{2}\sin(\theta/2)}{2}$$

$$B_{,r}^3 = \frac{\sin(\theta/2) \ \sin(\theta)}{2\sqrt{2}} \quad B_{,\theta}^3 = \sqrt{r}\left(\frac{\cos(\theta/2) \ \sin(\theta)}{2} + \sin(\theta/2) \ \cos(\theta)\right)$$

$$B_{,r}^4 = \frac{\cos(\theta/2) \ \sin(\theta)}{2\sqrt{2}} \quad B_{,\theta}^4 = \sqrt{r}\left(\frac{\sin(\theta/2) \ \sin(\theta)}{2} + \cos(\theta/2) \ \cos(\theta)\right) \quad (5.100)$$

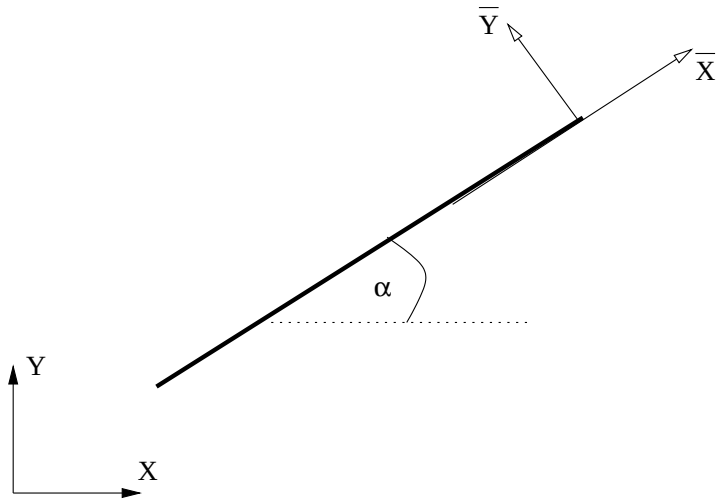

Figure 5.20: Definition of a local crack coordinate system

The derivatives of r and θ with respect to the local crack coordinate system are

$$\begin{aligned} r_{,\bar{X}} &= \cos(\theta) \quad \theta_{,\bar{X}} = -\sin/r \\ r_{,\bar{Y}} &= \sin(\theta) \quad \theta_{,\bar{Y}} = \cos/r \end{aligned} \tag{5.101}$$

With (5.100) and (5.101) in (5.99), we have the derivatives of the branch functions in the local crack coordinate system:

$$\begin{aligned} B^1_{,\bar{X}} &= \frac{\sin(\theta/2)}{2\sqrt{2}} \quad B^1_{,\bar{Y}} = \frac{\cos(\theta/2)}{2\sqrt{2}} \\ B^2_{,\bar{X}} &= \frac{\cos(\theta/2)}{2\sqrt{2}} \quad B^2_{,\bar{Y}} = \frac{\sin(\theta/2)}{2\sqrt{2}} \\ B^3_{,\bar{X}} &= -\frac{\sin(3\theta/2)\,\sin(\theta)}{2\sqrt{2}} \quad B^3_{,\bar{Y}} = \frac{\sin(\theta/2)+\sin(3\theta/2)\,\cos(\theta)}{2\sqrt{2}} \\ B^4_{,\bar{X}} &= -\frac{\cos(3\theta/2)\,\sin(\theta)}{2\sqrt{2}} \quad B^4_{,\bar{Y}} = \frac{\cos(\theta/2)+\cos(3\theta/2)\,\cos(\theta)}{2\sqrt{2}} \end{aligned} \tag{5.102}$$

Finally, the derivatives in the global coordinate system are obtained by:

$$\begin{aligned} \mathbf{B}_{,X} &= \mathbf{B}_{,\bar{X}}\cos(\alpha) + \mathbf{B}_{,\bar{Y}}\sin(\alpha) \\ \mathbf{B}_{,Y} &= \mathbf{B}_{,\bar{X}}\sin(\alpha) + \mathbf{B}_{,\bar{Y}}\cos(\alpha) \end{aligned} \tag{5.103}$$

where α is the inclination angle of the local crack coordinate system versus the global coordinate system.

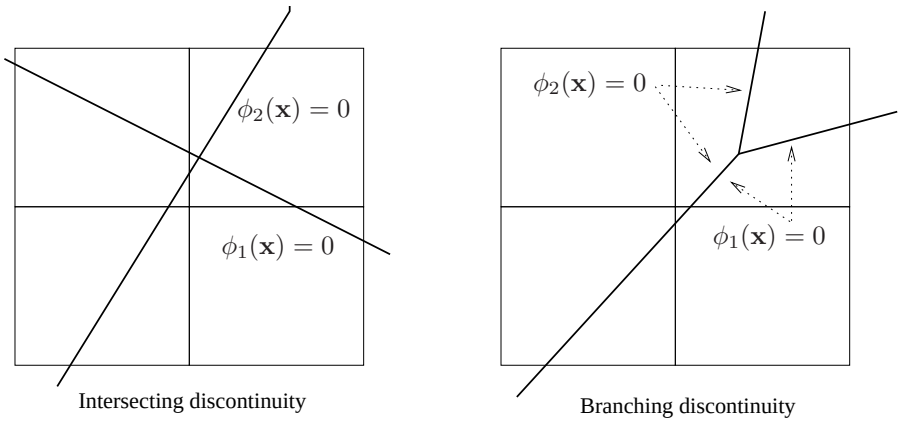

Figure 5.21: XFEM element with intersecting discontinuities and branching discontinuities

5.8.5 Advanced XFEM in LEFM

Crack branching and crack junction

Let us consider the case of crack branching and crack intersection in a single finite element as shown in figure 5.21. Let $\mathcal{S}_c^1$ be the set of nodes whose domain of influence is completely cut by the discontinuity described with the signed distance function $\phi_1(\mathbf{X}) = 0$ and $\mathcal{S}_c^2$ the corresponding set for $\phi_2(\mathbf{X}) = 0$; $\mathcal{S}_c^3 = \mathcal{S}_c^1 \bigcap \mathcal{S}_c^2$. The same applies accordingly for nodes whose domain of influence is cut by the crack tip enrichment. We will denote this set of nodes with $\mathcal{S}_t^1$ and $\mathcal{S}_t^2$. Then the approximation of the displacement may be given by

$$\begin{aligned}
\mathbf{u}^h(\mathbf{X}) &= \sum_{I \in \mathcal{S}(\mathbf{X})} N_I(\mathbf{X})\ \mathbf{u}_I + \sum_{I \in \mathcal{S}_c^1(\mathbf{X})} N_I(\mathbf{X})\ H(\phi_1(\mathbf{X}))\ \mathbf{a}_I^{(1)} \\
&+ \sum_{I \in \mathcal{S}_c^2(\mathbf{X})} N_I(\mathbf{X})\ H(\phi_2(\mathbf{X}))\ \mathbf{a}_I^{(2)} \\
&+ \sum_{I \in \mathcal{S}_c^3(\mathbf{X})} N_I(\mathbf{X})\ H(\phi_1(\mathbf{X}))\ H(\phi_2(\mathbf{X}))\ \mathbf{a}_I^{(3)} \\
&+ \sum_{I \in \mathcal{S}_t^1(\mathbf{X})} N_I(\mathbf{X})\ \sum_K \mathbf{B}_K^{(1)}(\mathbf{X})\ \mathbf{b}_{KI}^{(1)} \\
&+ \sum_{I \in \mathcal{S}_t^2(\mathbf{X})} N_I(\mathbf{X})\ \sum_K \mathbf{B}_K^{(2)}(\mathbf{X})\ \mathbf{b}_{KI}^{(2)}
\end{aligned} \tag{5.104}$$

Note, that crack branching requires the introduction of another level set. Crack junction can be treated similarly. A computationally more efficient approach was proposed by Zi et al. [21] by modifying the signed distance functions so that no cross terms are needed for junction or branch problems.

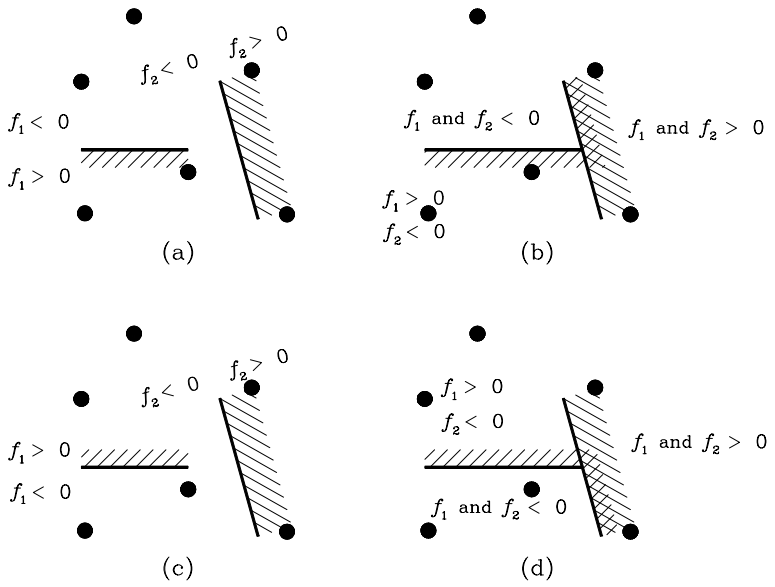

Figure 5.22: Sign functions for crack junction

When two cracks are joining, the crack tip enrichment is removed. By using the signed distance functions of the pre-existing and approaching crack, the signed distance function of the approaching crack is modified, see figure 5.22. Three different subdomains have to be considered: $(\phi_1 < 0, \phi_2 < 0)$, $(\phi_1 > 0, \phi_2 > 0)$, $(\phi_1 > 0, \phi_2 < 0)$ as in figure 5.22b or $(\phi_1 > 0, \phi_2 < 0)$, $(\phi_1 > 0, \phi_2 > 0)$, $(\phi_1 < 0, \phi_2 < 0)$ as in figure 5.22d. The signed distance function of crack 1 of a point $\mathbf{X}$ is then obtained by:

$$\phi_1(\mathbf{X}) = \begin{cases} \phi_1^0(\mathbf{X}), & \text{if } \phi_2^0(\mathbf{X_1})\,\phi_2^0(\mathbf{X}) > 0 \\ \phi_2^0(\mathbf{X}), & \text{if } \phi_2^0(\mathbf{X_1})\,\phi_2^0(\mathbf{X}) < 0 \end{cases} \tag{5.105}$$

where the superimposed 0 denotes the sign distance function before crack junction. Therefore, the final approximation without the cross term reads:

$$\begin{aligned} \mathbf{u}^h(\mathbf{X}) &= \sum_{I \in \mathcal{S}(\mathbf{X})} N_I(\mathbf{X})\ \mathbf{u}_I + \sum_{n=1}^{n_c} \sum_{I \in \mathcal{S}_c(\mathbf{X})} N_I(\mathbf{X})\ H(\phi_I^{(n)}(\mathbf{X}))\ \mathbf{a}_I^{(n)} \\ &+ \sum_{m=1}^{m_t} \sum_{I \in \mathcal{S}_t(\mathbf{X})} N_I(\mathbf{X})\ \sum_K \mathbf{B}_K^{(m)}(\mathbf{X})\ \mathbf{b}_{KI}^{(m)} \end{aligned} \tag{5.106}$$

where n_c and m_t are the number of cracks that completely cross the element or contain the crack tip, respectively.

Crack opening and crack closure

The governing equations in section 5.8 were formulated for a traction-free crack problem. To be more precise, the problem was stated only for the case of crack opening. The case of crack closure that can arise for example under cyclic loading conditions was not considered in that formulation. To generalize the crack problem in elastostatics, let us rephrase the problem:

$$\nabla_0 \cdot \mathbf{P} - \mathbf{b} = \emptyset \quad \forall \mathbf{X} \in \Omega_0 \setminus \Gamma_0^c \tag{5.107}$$

with boundary conditions

$$\mathbf{u}(\mathbf{X}, t) = \bar{\mathbf{u}}(\mathbf{X}, t) \quad \text{on} \quad \Gamma_0^u \tag{5.108}$$

$$\mathbf{n}_0 \cdot \mathbf{P}(\mathbf{X}, t) = \bar{\mathbf{t}}_0(\mathbf{X}, t) \quad \text{on} \quad \Gamma_0^t \tag{5.109}$$

$$\mathbf{n}_0 \cdot \mathbf{P}(\mathbf{X}, t) = 0 \quad \text{on} \quad \Gamma_0^c \quad \text{if not in contact} \tag{5.110}$$

$$t_{0t}^+ = t_{0t}^- = 0, \quad t_{0N}^+ = -t_{0N}^- \quad \text{on} \quad \Gamma_0^c \quad \text{if in contact} \tag{5.111}$$

$$[\![\mathbf{u}_N]\!] \leq 0 \quad \text{on} \quad \Gamma_0^c \tag{5.112}$$

$$[\![\mathbf{n} \cdot \mathbf{P}]\!] = 0 \quad \text{on} \quad \Gamma_0^c \tag{5.113}$$

where eqs. (5.107) to (5.110) were already formulated in section 5.8 and eqs. (5.111) to (5.113) guarantee no interpenetration where $t_{0N} = \mathbf{n} \cdot \mathbf{P} \cdot \mathbf{n}$ is the normal traction and t_{0t} is the traction acting in tangential direction of the crack. The inequality (5.112) with $[\![\mathbf{u}_N]\!] = \mathbf{u}^+ \cdot \mathbf{n}^+ = \mathbf{u}^- \cdot \mathbf{n}^- \leq 0$ guarantees that the crack surfaces do not interpenetrate in the case of crack closure and eq. (5.113) ensures traction continuity. The superimposed plus and minus sign indicates the different sides of the crack surfaces. Note that it is often assumed that $\mathbf{n}^+ = \mathbf{n}^-$ though this assumption is not mandatory.

If the Lagrange multiplier method is used to enforce no-interpenetration conditions of the adjacent crack surfaces, the weak form of the equilibrium equation reads:

$$\int_{\Omega_0} (\nabla \otimes \delta\mathbf{u})^T : \mathbf{P} \, d\Omega_0 - \int_{\Omega_0} \delta\mathbf{u} \cdot \mathbf{b} \, d\Omega_0 - \int_{\Gamma_0^t} \delta\mathbf{u} \cdot \bar{\mathbf{t}}_0 \, d\Gamma_0 + \delta \int_{\Gamma_0^c} \boldsymbol{\lambda} \, [\![\mathbf{u}_N]\!] \, d\Gamma_0 \geq 0 \tag{5.114}$$

where it is sufficient to chose $\mathcal{C}^{-1}$ approximation functions for the Lagrange multiplier field if the approximating functions for the test and trial function are $\mathcal{C}^0$.

Cracking criteria in LEFM

Let us consider a specimen that has a pre-crack or a notch and we are interested if the pre-crack will propagate (or not) under a certain stress state. There are basically four major cracking or crack propagation[8] criteria in LEFM:

- Maximum hoop stress criterion or maximum principal stress criterion
- Minimum strain energy density criterion, Shih [22]
- Maximum energy release rate criterion, Wu [23]
- The zero K_{II} criterion (Vanishing in-plane SIF (K_{II}) in shear mode for infinitesimally small crack extension), Goldstein and Salganik [24]

The first two criteria predict the direction of the crack trajectory from the stress state prior to the crack extension. The last two criteria require stress analysis for virtually extended cracks in various directions to find the appropriate crack-growth direction. Note, that these criteria will give only the orientation of the crack but not its length. To determine the crack length, these criteria have to be checked in different distances around the crack tip. Often a constant crack propagation speed is assumed. In computational LEFM, the first of the above mentioned criteria is mostly used. The crack is propagated in an angle of θ_c from the crack tip.

In the maximum hoop stress or maximum principal stress criterion, a crack is oriented perpendicular to the direction of the maximum principal stress. The maximum circumferential stress $\sigma_{\theta\theta}$, often called hoop stress, in the polar coordinate system around the crack tip corresponds to the maximum principal stress and is given for a crack propagating with constant velocity v_c by:

$$\sigma_{\theta\theta} = \frac{K_I}{\sqrt{2\pi r}} f_h^I(\theta, v_c) + \frac{K_{II}}{\sqrt{2\pi r}} f_h^{II}(\theta, v_c) \tag{5.115}$$

where the functions f_h^I and f_h^{II} represent the angular variation of stress for different values of crack-tip speed v_c. When the maximum hoop stress is larger equal a critical hoop stress $\sigma_{\theta\theta}^c$, then the crack is propagated in the direction perpendicular to the maximum hoop stress. For pure mode I fracture, $\sigma_{\theta\theta}^c$ is given by

$$\sigma_{\theta\theta}^c = \frac{K_I^c}{\sqrt{2\pi r}} \tag{5.116}$$

with the fracture toughness K_I^c that is obtained from experiments. The local direction of the crack growth is determined by the condition that the local shear stress is zero that leads to the condition:

$$K_I \sin\theta_c + K_{II}\,(3\cos\theta_c - 1) = 0 \tag{5.117}$$

[8] Note that crack initiation cannot be modeled with the criteria mentioned here

that results in the crack propagation angle

$$\theta_c = 2\arctan\left(\frac{K_I - \sqrt{K_I^2 + 8K_{II}^2}}{4K_{II}}\right) \tag{5.118}$$

Diagonalized mass matrix

Methods that are based on an explicit time integration generally use a diagonalized mass matrix that is obtained by a simple row-sum technique. A diagonalized mass matrix facilitates the solution of the system of equations enormously. However, if additional degrees of freedom are introduced as in XFEM, it can be shown that a standard row-sum technique will lead to an erroneous lumped mass matrix[9]. A row-sum technique for standard XFEM can be obtained based on the assumption that for a rigid body motion, the discrete kinetic energy has to be exact. A lumped mass matrix can then be obtained by:

$$m_{diag} = \frac{m}{n_{nodes}} \frac{1}{mes(\Omega_{el})} \int_{\Omega_{el}} \psi^2 \, d\Omega_{el} \tag{5.119}$$

where Ω_{el} is the element being considered, m is its mass, $mes(\Omega)_{el}$ its length, n_{nodes} the number of nodes in Ω and ψ is the enrichment function. If the step function is used, the mass matrix can be diagonalized by one of these two procedures:

$$\mathbf{M}_{II}^{lumped} = \sum_J \mathbf{M}_{IJ}^{consistent}, \quad \text{or}$$

$$\mathbf{M}_{II}^{lumped} = m \frac{\mathbf{M}_{II}^{consistent}}{\sum_J \mathbf{M}_{IJ}^{consistent}} \tag{5.120}$$

One difficulty with a diagonalized mass matrix in an XFEM formulation is that the critical time step $\Delta t \leq \Delta t_c = 2/\omega_{max}$ is reduced drastically when a crack is located close to a node[10]. Within the approach proposed above, the critical time step is not diminished so drastically when the discontinuity is close to a node; drastically means by a factor around 2 (compared to the CFL criterion of the element without discontinuity). Note that the lumping procedure is slightly different when the Heaviside function is used as enrichment.

Example Let us consider a one-dimensional element with two nodes. The approximation is given by

$$\mathbf{u}^h(\mathbf{X}) = N_1 \, \mathbf{u}_1 + N_1 \, \phi_1 \, \mathbf{a}_1 + N_2 \, \mathbf{u}_2 + N_2 \, \phi_2 \mathbf{a}_2 \tag{5.121}$$

and the lumped mass matrix of the element by

$$\mathrm{M}_{lumped} = \begin{bmatrix} m_1 & 0 & 0 & 0 \\ 0 & m_2 & 0 & 0 \\ 0 & 0 & m_3 & 0 \\ 0 & 0 & 0 & m_4 \end{bmatrix} \tag{5.122}$$

[9] Note that for the Hansbo-Hansbo XFEM, a standard row sum technique is sufficient

[10] Note that ω_{max} is the largest solution of $\det(\mathbf{K} - \omega \, \mathbf{M})$ where $\mathbf{K}$ is the stiffness matrix and $\mathbf{M}$ the mass matrix

The coefficients m_i have to be determined such that $E^h_{kin} = 0.5\dot{\mathbf{u}}^T\ \mathbf{M}_{lumped}\ \dot{\mathbf{u}}$ equals $E_{kin} = 0.5 \int_{\Omega_{el}} \varrho\ \mathbf{v}^2\ d\Omega$. Let us consider that the element moves with a constant velocity $\bar{\dot{\mathbf{u}}}$ in the same direction. Hence, we set $\dot{\mathbf{a}}$ equal zero and obtain

$$E^h_{kin} = 0.5\left(m_1\ \dot{\mathbf{u}}_1^2 + m_2\ \dot{\mathbf{u}}_2^2\right) = 0.5\ \bar{\dot{\mathbf{u}}}^2\ (m_1 + m_2) \tag{5.123}$$

and obtain with $E_{kin} = 0.5\ m\ \bar{\dot{\mathbf{u}}}^2 = E^h_{kin}$ that $m_1 = m_2 = 0.5\ m$ where m is the mass of the element. Next let us consider the separation of the element into two parts, i.e. $\dot{\tilde{\mathbf{u}}} = \bar{\mathbf{a}}\phi_1(\mathbf{x})$. Thus, we set $\dot{\mathbf{u}}$ equal zero and obtain

$$E^h_{kin} = 0.5\left(m_3\ \dot{\mathbf{a}}_1^2 + m_4\ \dot{\mathbf{a}}_2^2\right) = 0.5\ \bar{\mathbf{a}}^2\ (m_3 + m_4) \tag{5.124}$$

and

$$E_{kin} = 0.5\ \varrho\ \bar{\mathbf{a}}^2 \int_{\Omega_{el}} \psi_1^2\ d\Omega_{el} \tag{5.125}$$

so that finally the mass m_3 and m_4 are

$$m_3 = m_4 = \frac{m}{2\ mes(\Omega)_{el}} \int_{\Omega_{el}} \psi_1^2\ d\Omega_{el} \tag{5.126}$$

Let us now determine the minimal critical time step for the one-dimensional XFEM element and compare it to the critical time step of a standard element. If the length of the element is denoted by l, the linear shape function can be given by

$$\begin{aligned} N_1(x) &= 1 - \frac{x}{l} \\ N_2(x) &= \frac{x}{l} \end{aligned} \tag{5.127}$$

The consistent mass matrix and the stiffness matrix of the standard element is given by

$$\mathrm{M}_{FE} = \varrho\ A\ l \begin{bmatrix} 1/3 & 1/6 \\ 1/6 & 1/3 \end{bmatrix}\ ,\ \mathrm{K}_{FE} = \frac{E\ A}{l} \begin{bmatrix} 1 & -1 \\ -1 & 1 \end{bmatrix} \tag{5.128}$$

where E is the Young's modulus and A the cross section. The critical time step is easily computed by

$$\Delta t_{c,FE} = \frac{2}{\omega_{max}} = l\sqrt{\frac{\varrho}{3E}} \tag{5.129}$$

With the lumped mass matrix

$$\mathrm{M}^{lumped}_{FE} = \varrho\ A\ l \begin{bmatrix} 1/2 & 0 \\ 0 & 1/2 \end{bmatrix} \tag{5.130}$$

the critical time step is

$$\Delta t^{lumped}_{c,FE} = l\sqrt{\frac{\varrho}{E}} = \sqrt{3}\Delta t_{c,FE} \tag{5.131}$$

Now, let us study the critical time step for the XFEM approximation. The discontinuity is located at position s and with the generalized step function centered in s, the approximation of the displacement field is

$$\begin{aligned} \mathbf{u}^h(x) &= N_1(x)\ \mathbf{u}_1 + N_1(x)\ S(x-s)\ \mathbf{a}_1 \\ &+ N_2(x)\ \mathbf{u}_2 + N_2(x)\ S(x-s)\mathbf{a}_2 \end{aligned} \tag{5.132}$$

and the consistent mass matrix and stiffness matrix

$$\begin{aligned} \mathrm{M}_{XFEM} = \varrho\ A\ l \Bigg[& \begin{array}{cc} 1/3 & 1/6 \\ 1/6 & 1/3 \\ 2s^2-2s+1/3-2/3s^3 & 1/6-s^2+2/3s^3 \\ 1/6-s^2+2/3s^3 & 1/3-21 \end{array} \cdots \\ \cdots & \begin{array}{cc} 2s^2-2s+1/3-2/3s^3 & 1/6-s^2+2/3s^3 \\ 1/6-s^2+2/3s^3 & 1/3-2/3s^3 \\ 1/3 & 1/6 \\ 1-2s & 2s-1 \\ 1/6 & 1/3 \end{array} \Bigg] \end{aligned} \tag{5.133}$$

$$\mathrm{K}_{XFEM} = \frac{E\ A}{l} \begin{bmatrix} 1 & -1 & 1-2s & 2s-1 \\ -1 & 1 & 2s-1 & 1-2s \\ 1-2s & 2s-1 & 1 & -1 \\ 2s-1 & 1-2s & -1 & 1 \end{bmatrix} \tag{5.134}$$

The lumped mass matrix for the XFEM approximation is

$$\mathrm{M}^{lumped}_{XFEM} = 0.5\ \varrho\ A\ l \begin{bmatrix} 1 & 0 & 0 & 0 \\ 0 & 1 & 0 & 0 \\ 0 & 0 & 1 & 0 \\ 0 & 0 & 0 & 1 \end{bmatrix} \tag{5.135}$$

The critical time step for the XFEM-approximation depends on the location of the discontinuity s in the element. The smallest critical time step is obtained when the discontinuity is located at $x = 0$ or $x = l$. For the consistent XFEM mass matrix, the critical time step goes to zero when the discontinuity approaches 0 or l while the critical time step at $x = 0$ and $x = l$ for the lumped XFEM mass matrix is $\Delta t^{lumped}_{c,XFEM} = \frac{1}{\sqrt{2}} \Delta t^{lumped}_{c,FE}$. Hence, even when the discontinuity is located very close to a node, the critical time step is not destroyed. In contrast, for the Hansbo-Hansbo approach, a standard row sum technique can be employed. However, the critical time step will tend to zero when the discontinuity approaches a node. In practice, a certain minimum mass is assigned to a node such that the computation can be proceeded.

Limitations

For particular discretizations and crack configurations, the XFEM approximation cannot accurately represent the discontinuity in the near-tip displacement

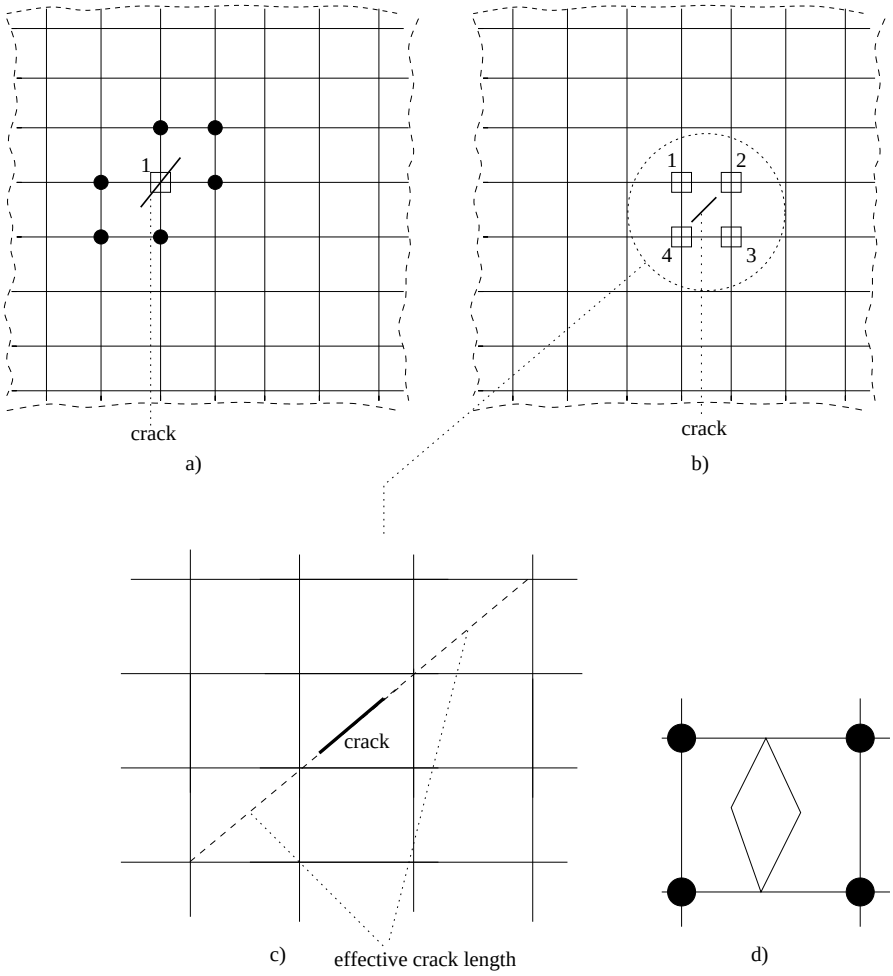

Figure 5.23: a),b) Crack length that approach the local element size cannot be accurately represented by the standard XFEM approximation. Dots denote single enriched nodes and squares denote double (in our case, the node will contain the enrichment of two crack tips) enriched nodes; c) the dashed line shows the effective crack length; d) even if no crack tip enrichment is used, in order to close the crack within a single element, no nodes have to be enriched with a step function

fields. Difficulties occur for the non-physical case of too close parallel cracks (within a single element) and when the extent of the crack approaches the support size of the nodal shape functions. Then, the asymptotic branch functions for each tip may extend beyond the length of the crack, resulting in a non-conforming approximation. Although the XFEM approximation is capable of representing crack geometries that are independent of element boundaries, it also relies on the interaction between the mesh and the crack geometry to determine the sets of enriched nodes. This leads to particular crack configurations that cannot be accurately be represented by eq. (5.87). Such cases are shown in figure 5.23. As the crack size approaches the local nodal spacing, the set $\mathcal{S}_c$ of nodes for the Heaviside or step enrichment is empty, figure 5.23b. Moreover, node 1 for the cracking case in figure 5.23a or nodes 1 to 4 for the cracking case in figure 5.23b, respectively, contain two branch enrichments. Thus, the standard approximation gets difficulties with this crack configuration since the discontinuous function $\sqrt{2}\sin(\theta/2)$ extends too far. This problem always arises when one or more nodal supports contain the entire crack geometry. Usually, this kind of problem arises whenever a crack nucleates. Similar difficulties occur for approximations without any crack tip enrichment, see figure 5.23d. In order to close the crack within a single element, the set $\mathcal{S}_c$ is empty as well. One solution is to refine the mesh locally such that the characteristic element size falls below that of the crack. An admissible crack configuration is shown in figure 5.24d.

Tracking the crack path

There are numerous ways to track the crack path and to represent the crack surface. The crack surface can be represented explicitly, meaning by introducing another mesh for the crack surface. Most commonly, the crack surface is described by piecewise linear crack segments though it is also possible to describe the crack surface smoothly, e.g. with B-splines or NURBS (Non uniform rational B-Spline). The crack surface can also be described implicitly with the help of level sets or signed distance functions[11]. Crack path tracking algorithms can be classified into three classes: global methods, local methods and the level set method.

The basic idea of the global crack tracking procedure is to define a linear thermal problem to be solved each time step of the original mechanical problem. Therefore, two vector fields $\mathbf{a}$ and $\mathbf{b}$ are introduced that have to fulfill the following condition:

$$\mathbf{a} \cdot \mathbf{n}_0 = \mathbf{b} \cdot \mathbf{n}_0 = 0 \tag{5.136}$$

where $\mathbf{n}_0$ is the crack normal in the initial configuration. The family of surfaces, enveloping both vector fields $\mathbf{a}$ and $\mathbf{b}$ can be described by a temperature-like

[11] Note that if the same approximating functions are used for the level set and the physical properties, meshfree methods are well suited for describing curved cracks due to their higher continuous shape functions

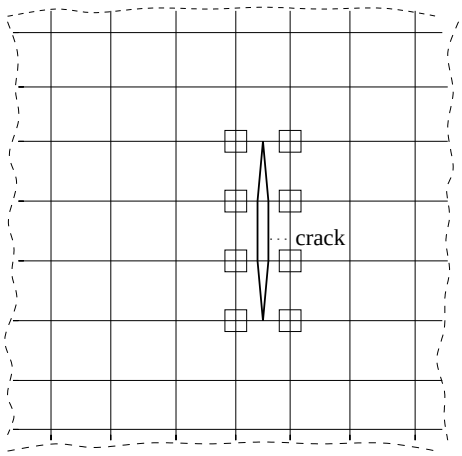

Figure 5.24: Admissible crack representation

function $\mathcal{T}(\mathbf{X})$ if

$$\begin{aligned} \mathbf{a} \cdot \nabla_0 \mathcal{T} = \nabla_0 \mathcal{T} \cdot \mathbf{a} = 0 \text{ in } \Omega_0 \\ \mathbf{b} \cdot \nabla_0 \mathcal{T} = \nabla_0 \mathcal{T} \cdot \mathbf{b} = 0 \text{ in } \Omega_0 \end{aligned} \tag{5.137}$$

holds. Eq. (5.137) can be rephrased as an anisotropic heat conduction problem. The drawback of this method is that the heat conduction problem has to be solved at every time step, that makes the method computationally expensive.

With local crack tracking algorithms, the alignment of the crack surfaces is enforced with respect to its neighborhood. Local crack tracking algorithms are usually characterized by recursively "cutting" elements and are especially effective in three dimensions.

As mentioned earlier, the original level set method is not well suited to track the crack path. First, the zero level set must be updated behind the tip to take into account the fact that once a material point is cracked, it remains cracked. Second, the level set functions are not updated with the speed of an interface in the direction normal to itself but with the speed at the crack fronts. Hence, the equations for updating the interface

$$\frac{\partial \phi}{\partial t} + \mathbf{v} \cdot \nabla \phi = 0 \tag{5.138}$$

cannot be adopted to model crack propagation. And third, the crack is an open surface that grows from its crack front. Therefore, an additional level set has to be introduced to be able to completely describe the crack surface. This additional level set function (at the crack tip) is perpendicular to the original level set function (and perpendicular to the current crack front) and hence has to be updated as well. The accuracy of the crack surface representation depends

on the discretization (shape functions) of the level set functions. Usually, the same discretization is employed for the mechanical properties and the level set function that makes the method very attractive and elegant from an implementational point of view. If highly curved cracks occur, linear finite element shape functions will fail to represent the crack surface exactly. Note, that a reinitialization is necessary after updating the level set functions to ensure that the zero level set function remains the signed distance function.

Crack propagation with level sets can be modelled by different techniques that can be classified into four groups. In the first group, the level set is updated by the solution of differential equations, similar to eq. (5.138) where the level set functions are the unknowns. These methods require the discretization of the level set functions. The second group is defined on algebraic relations between the coordinates of a given point, the coordinates of the crack front and the crack advance vector. The Vector level set method is defined in terms of geometric transformations. In the vector level set method, the distance to the crack surface is stored in addition to the signed distance function. This facilitates implementation since there is no need to solve a PDE to update the level set. The last class of methods are based on algebraic and trigonometric equations involving the initial value of the level set functions and the crack advance vector. Some of them also require the description of the crack front.

The level set technique couples well for methods that use a crack tip enrichment since they can be exploited to compute the distance to the crack front $r = \sqrt{\phi^2 + \psi^2}$ where ψ is the level set perpendicular to ϕ and the angle $\theta = \arctan(\phi/\psi)$, see figure 4.6. The level sets are especially useful for the approximation of θ since they guarantee that $\theta = \pm\pi$ on the crack surface since $\phi = 0$.

Non-matching meshes

As stated before, one big advantage of tracking the crack path with level sets is that no explicit representation of the crack geometry is needed. The level set can be approximated with the same shape functions as the mechanical properties. However, in certain cases, this approximation might not be sufficient. For example, if the "usual" mesh is described with linear finite elements[12], then the curvature of the crack might be not represented accurately enough for certain applications. In this case, the level set is approximated with different[13] shape functions and a different mesh that is non-conforming with the "usual" finite element mesh.

Then, the mechanical model will provide the crack orientation and crack length. Update, reinitialization and orthogonalization can be done on the "usual" mesh. The crack update is made by solving the Hamilton-Jacobi equation at each point of the "level-set mesh". Once the new level set functions are determined, a projection is needed to give their value on the "usual" mesh. In

[12] i.e. with triangular elements
[13] in that case higher order shape functions

order to keep projection errors small, the size of the level-set mesh should be of the order of the "usual" mesh.

Chapter 6

Other Methods

6.1 EXtended meshfree methods

EXtended meshfree methods basically have the same structure as the XFEM. One major difficulty in extended meshfree methods is the closure of the crack at its crack tip due to the strong overlapping of the meshfree shape functions, see figure 6.1. The simplest way to ensure that the crack closes at its tip is with the use of branch functions. Another opportunity is to modify the support size of the nodes close to the crack tip such that its domain of influence will be cut completely as shown in figure 6.2. The domain of influence of node 1 is completely cut by the crack and it is enriched by the sign function. Crack tip P is located inside the domain of influence of node 2 which is partially cut. The shape function Φ_I for the discontinuous displacement is scaled down so that the crack tip is positioned at its edge as shown in the figure, i.e.

$$\Phi_J^*(\mathbf{X}) = \mathbf{p}^T(\mathbf{X}) \cdot \mathbf{A}^*(\mathbf{X})^{-1} \cdot \mathbf{D}^*(\mathbf{X}_J) \tag{6.1}$$

$$\mathbf{A}^*(\mathbf{X}) = \sum_J \mathbf{p}(\mathbf{X}_J)\, \mathbf{p}^T(\mathbf{X}_J)\, W(\bar{r}_J^*;\, h^*) \tag{6.2}$$

$$\mathbf{D}^*(\mathbf{X}_J) = \sum_J \mathbf{p}(\mathbf{X}_J)\, W(\bar{r}_J^*;\, h^*) \tag{6.3}$$

in which the asterisk denotes the modification for the crack tip and h^* is the modified size of the domain of influence. Note that the shape function for the continuous displacement remains unchanged.

The domain of influence of node 3 is also partially cut and the shape function may be shrunk, too. However, the node is not enriched since it is very close to the crack tip and the shape function becomes very small compared to others after it is modified and the approximation for the discontinuous displacement field becomes bumpy. Therefore, when the domain of influence of a node is partially cut, we enrich the node if the support of the shape function includes at least one enriched node after it is modified. Node 4 is not enriched because the shape function becomes not cut by the crack as it is modified.

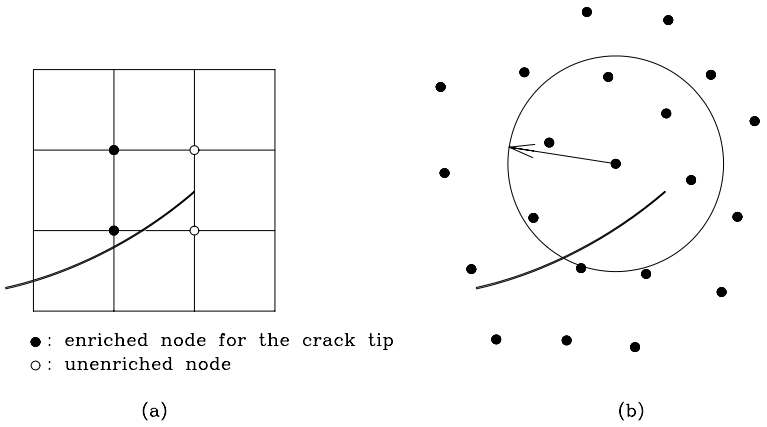

Figure 6.1: a) XFEM enrichment such that the crack closes at its crack tip and b) the problematic of crack closure in meshfree methods

One drawback of the method is that the crack appears to be shorter for particles close to the crack and the crack tip. Instead of modifying the shape function of the node of which domain of influence is partially cut, we may consider the use of the Lagrange multiplier method. If only the sign function enrichment is used, there is the extension of discontinuity $\Gamma_{c,ext}$ beyond the crack tip; see Fig. 6.3. To model the crack, the discontinuity on $\Gamma_{c,ext}$ should vanish. Because the condition should be satisfied along a line, not at a point, the Lagrange multiplier must be discretized, too. To avoid introducing another nodes for the discretization, the same shape functions as those partially cut by the crack can be used.

6.2 Embedded elements

In 1987, Ortiz et al. [25] modified the approximation of the strain field to capture weak discontinuities in finite elements to improve the resolution of shear bands. Therefore, they enriched the strain field to obtain the kinematic relations shown in figure 6.4a. Based on this idea, Belytschko et al. [26] allowed two parallel weak discontinuity lines in a single element, figure 6.4b, so that the element was able to contain a band of localized strain. Dvorkin et al. [27] were the first who developed a method that was able to deal successfully with *strong* discontinuities in finite elements. The class of *embedded elements* was born. The name comes from the fact that the localization zone is embedded in a single element, see figure 6.4c. This way, crack growth can be modeled without remeshing. This class of methods are much more flexible than schemes that allow discontinuities only at element interfaces, and it eliminates the need for continuous remeshing. As in XFEM, embedded elements introduce additional

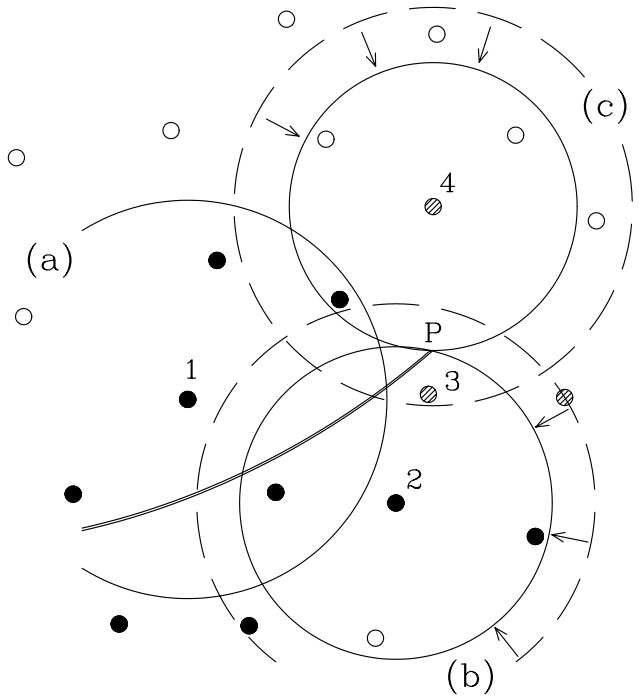

Figure 6.2: Decreasing the support size to close the crack at its crack tip

unknowns into the variational formulation. However, the enrichment is on the element level. This has the advantage, that the additional unknowns can be condensed on the element level, so that discontinuities can be captured only with very small changes of the existing code. The drawback is that embedded elements are less flexible than XFEM. The crack can only open piecewise constant. Moreover, the crack can be propagated one element at a time. A typical crack representation for embedded elements are shown in figure 6.5. Note, that in embedded elements, a tip enrichment cannot be employed as is XFEM[1] since the crack opens piecewise constant.

The first version of *embedded elements* is often called statical optimal symmetric (SOS) since traction continuity is fulfilled but it is not possible to capture the correct crack kinematics. It has been shown, that SOS formulations lead to stress locking, i.e. stresses are transmitted across the crack even if the crack is wide open. The kinematical optimal symmetric (KOS) version by Lofti and Shing [28] ensures the correct crack kinematics but violates the traction continuity condition. Consequently, the criteria for the onset of localization written in terms of stresses in the bulk are no longer equivalent to the same criteria

[1] due to the lack of a crack tip

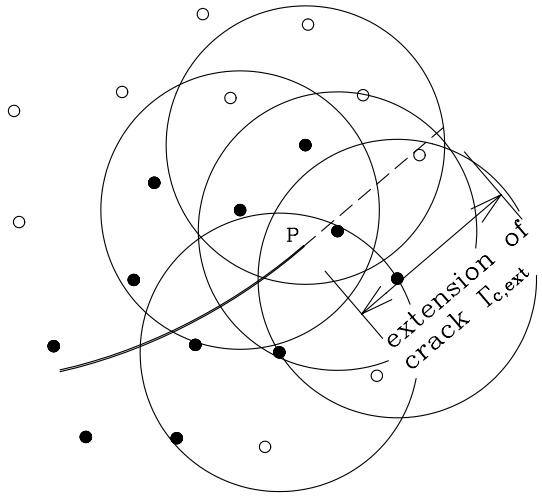

Figure 6.3: The discontinuity $\Gamma_{c,ext}$ beyond crack tip P when nodes are enriched by using only the sign function.

written in terms of the tractions on the discontinuity area; e.g. for the Rankine criterion, the normal traction at the onset of localization should be equal to the tensile strength and the shear traction should be zero. This cannot be properly reproduced by the KOS formulation. The kinematical and statical optimal non-symmetric (KSON) version of embedded elements [27] guarantees traction continuity and the appropriate crack kinematics but leads to a non-symmetric stiffness matrix with all its disadvantage with respect to solving the linearized system of equations.

In embedded elements, the approximation of the displacement field is given

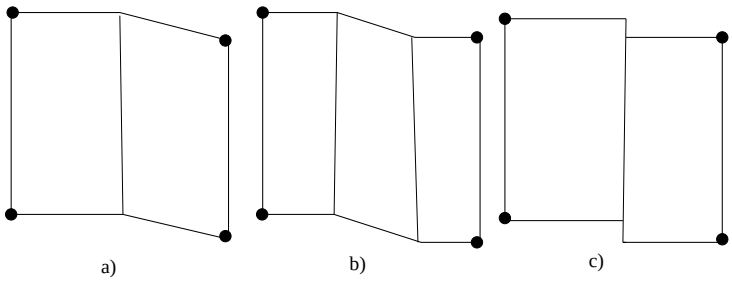

Figure 6.4: Element with a) one weak discontinuity, b) two weak discontinuities, c) one strong discontinuity

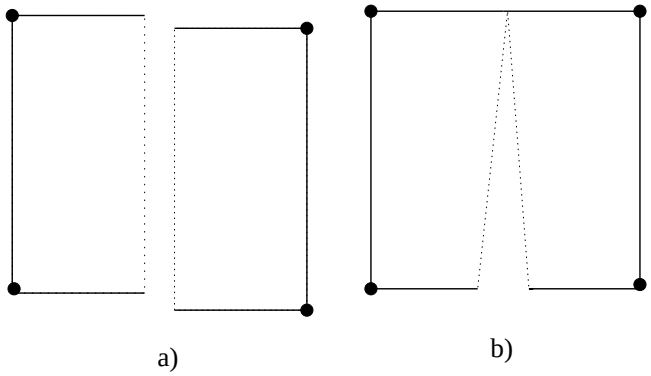

Figure 6.5: a) Piecewise constant crack opening in embedded elements and b) linear crack opening for linear XFEM

by:

$$\mathbf{u}^h(\mathbf{X}) = \sum_{I \in \mathcal{S}} N_I(\mathbf{X})\ \tilde{\mathbf{u}}_J + \mathcal{M}_s^{(e)}(\mathbf{X})\ [\![\hat{\mathbf{u}}_I^{(e)}(X)]\!] \tag{6.4}$$

where $\tilde{\mathbf{u}}$ is the usual approximation, $\hat{\mathbf{u}}$ is the enrichment and the superimposed "(e)" indicates the enrichment on element level. In other words, only one additional degree of freedom in every coordinate direction is introduced per element. Let us consider a linear quadrilateral element for example. In XFEM, this element would have 4 additional degrees of freedom in every coordinate direction, i.e. 8 additional degrees of freedom while in embedded elements only one additional degree of freedom[2] in every coordinate direction is introduced. The function $\mathcal{M}_s^{(e)}$ is given by

$$\mathcal{M}_s^{(e)}(\mathbf{X}) = \begin{cases} 0 & \forall (e) \notin S \\ H_s^{(e)} - \rho^{(e)} & \forall (e) \in S \\ \rho^{(e)} = \sum\limits_{I=1}^{N_e^+} N_I^+(\mathbf{X}) & \end{cases} \tag{6.5}$$

where H_s is the step function acting on the crack line S and N_e^+ is the number of nodes of element (e) that belong to the domain Ω_0^+, see figure 6.6. By standard differentiation, the discontinuous strain field is obtained:

$$\boldsymbol{\epsilon}^h(\mathbf{X}) = \sum_{I \in \mathcal{S}} (\nabla_0 N_I(\mathbf{X}) \otimes \tilde{\mathbf{u}}_I)^S - \left(\nabla \rho^{(e)} \otimes [\![\hat{\mathbf{u}}_I^{(e)}(X)]\!]\right)^S + \frac{\eta_s^{(e)}}{k} \left([\![\hat{\mathbf{u}}_I^{(e)}(X)]\!] \otimes \mathbf{n}\right)^S \tag{6.6}$$

where the superimposed S denotes the symmetric part and the term $\eta_s^{(e)}/k$ is a

[2] This enrichment is inherent of the element

regularized Dirac delta function and $\eta_s^{(e)}$ is a collocation function defined as

$$\eta_s^{(e)} = \begin{cases} 1 & \forall \mathbf{X} \in S_e^k \\ 0 & \forall \mathbf{X} \notin S_e^k \end{cases} \tag{6.7}$$

with the thickness k of the localization band. Considering the equilibrium equation in elastostatics and with the trial and test function of the structure of (6.4), the discrete equations in matrix form can be written as

$$\begin{bmatrix} \mathbf{K}_{\tilde{u}\tilde{u}}^{(e)} & \mathbf{K}_{\tilde{u}\hat{u}}^{(e)} \\ \mathbf{K}_{\hat{u}\tilde{u}}^{(e)} & \mathbf{K}_{\hat{u}\hat{u}}^{(e)} \end{bmatrix} \begin{Bmatrix} \tilde{\mathbf{u}}^{(e)} \\ [\![\hat{\mathbf{u}}_I^{(e)}]\!] \end{Bmatrix} = \begin{Bmatrix} \mathbf{F}_I^{ext} \\ \mathbf{0} \end{Bmatrix} \tag{6.8}$$

with

$$\begin{aligned} \mathbf{K}_{\tilde{u}\tilde{u}}^{(e)} &= \int_{\Omega_0} \mathbf{B}^T \, \mathbf{C} \, \mathbf{B} \, d\Omega_0 \\ \mathbf{K}_{\tilde{u}\hat{u}}^{(e)} &= \int_{\Omega_0} \mathbf{B}^T \, \mathbf{C} \, \hat{\mathbf{B}} \, d\Omega_0 \\ \mathbf{K}_{\hat{u}\tilde{u}}^{(e)} &= \int_{\Omega_0} \hat{\mathbf{B}}_*^T \, \mathbf{C} \, \mathbf{B} \, d\Omega_0 \\ \mathbf{K}_{\hat{u}\hat{u}}^{(e)} &= \int_{\Omega_0} \hat{\mathbf{B}}_*^T \, \mathbf{C} \, \hat{\mathbf{B}} \, d\Omega_0 \end{aligned} \tag{6.9}$$

where $\mathbf{C}$ is the elasticity tensor, $\mathbf{B}$ is the B-operator defined earlier,

$$\nabla \rho^{(e)} = \begin{bmatrix} \frac{\partial \rho^{(e)}}{\partial x} & 0 \\ 0 & \frac{\partial \rho^{(e)}}{\partial y} \\ \frac{\partial \rho^{(e)}}{\partial y} & \frac{\partial \rho^{(e)}}{\partial x} \end{bmatrix} \tag{6.10}$$

$$\mathbf{n}^{(e)} = \begin{bmatrix} n_x & 0 \\ 0 & n_y \\ n_y & n_x \end{bmatrix} \tag{6.11}$$

and $\hat{\mathbf{B}}$ is the B-operator of the enrichment that depends on the embedded element formulation (SOS, KOS or KSON). For the KSON formulation, $\hat{\mathbf{B}}_* \neq \hat{\mathbf{B}}$, that will result in a non-symmetric stiffness matrix. For the SOS and KOS formulation, $\hat{\mathbf{B}}_* = \hat{\mathbf{B}}$. The elemental enrichment $[\![\hat{\mathbf{u}}_I^{(e)}]\!]$ can be condensed on the element level:

$$[\![\hat{\mathbf{u}}_I^{(e)}]\!] = -\left[\mathbf{K}_{\hat{u}\hat{u}}^{(e)}\right]^{-1} \mathbf{K}_{\hat{u}\tilde{u}}^{(e)} \, \tilde{\mathbf{u}}^{(e)} \tag{6.12}$$

that leads with the expression for $[\![\hat{\mathbf{u}}_I^{(e)}]\!]$ to the system of equations of the type

$$\bar{\mathbf{K}} \, \mathbf{u} = \mathbf{f} \tag{6.13}$$

with

$$\bar{\mathbf{K}} = \mathbf{K}_{\tilde{u}\tilde{u}} - \mathbf{K}_{\tilde{u}\hat{u}} \, \mathbf{K}_{\hat{u}\hat{u}}^{-1} \, \mathbf{K}_{\hat{u}\tilde{u}} \tag{6.14}$$

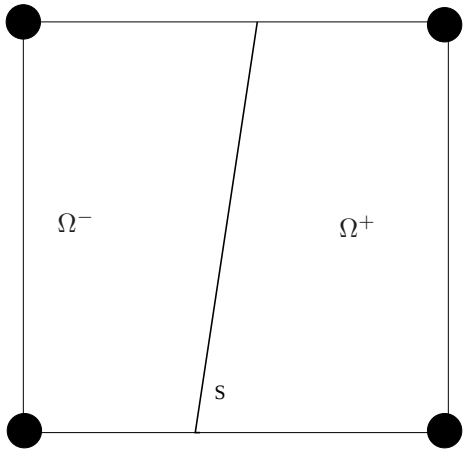

Figure 6.6: Embedded element cut by a discontinuity S

The embedded element formulation is proposed in different format, starting from the extended principle of virtual work over Hellinger Reissner to Hu-Washizu variational principle, using an enhanced assumed strain (EAS) or B-bar format.

6.3 Interface separation models

Standard finite elements will generally have difficulties to capture the crack kinematics since they use continuous trial functions that are not particularly well adapted for solutions with discontinuous displacement fields. Therefore, it is not surprising that the first models capable of describing the crack are the so-called *interelement – separation methods*. In these methods, cracks are only allowed to develop along existing interelement edges. This endows the method with comparative simplicity, but can result in an overestimate of the fracture energy when the actual crack paths are not coincident with element edges. The results depend severely not only on the mesh size (and form of the chosen element) but also the mesh bias that can be compensated only by computational expensive remeshing. Furthermore, it has been noted that the solutions sometimes depend significantly on mesh refinement. This sensitivity has been mollified by adding randomness to the strength, as in Zhou and Molinari [29] and Espinosa et al. [30], though such corrections are not yet understood. Nevertheless, many interesting problems have been studied by this method.

There are basically two types of interlement separation models. The Needleman-group introduces (initially inactive) cohesive surfaces at the beginning of the computation. This method is from the implementational point very simple but suffers from all the drawbacks mentioned above. The interelement separation models of Ortiz use remeshing and adaptive insertion of cohesive segments in the course of the simulation. This technique is more accurate but computa-

tionally expensive (because of the remeshing) and from an implementational point of view more burdensome. Moreover, errors are introduced because of the mapping that is needed during remeshing.

Bibliography

[1] T. Belytschko, W. K. Liu, and B. Moran. *Nonlinear Finite Elements for Continua and Structures*. John Wiley and Sons, Chichester, 2000.

[2] T. Belytschko, Y. Krongauz, D. Organ, M. Fleming, and P. Krysl. Meshless methods: An overview and recent developments. *Computer Methods in Applied Mechanics and Engineering*, 139:3–47, 1996.

[3] A. Huerta, Belytschko T., Fernandez-Mendez S., and Rabczuk T. *Encyclopedia of Computational Mechanics*, chapter Meshfree Methods. John Wiley and Sons, 2004.

[4] R.A. Gingold and J.J. Monaghan. Smoothed particle hydrodynamics:theory and applications to non-spherical stars. *Mon. Not. R. astr. Soc.*, 181:375–389, 1977.

[5] G.R. Johnson and S.R. Beissel. Normalized smoothing functions for sph impact computations. *International Journal for Numerical Methods in Engineering*, 39:2725–2741, 1996.

[6] Y. Krongauz and T. Belytschko. Consistent pseudo derivatives in meshless methods. *Computer Methods in Applied Mechanics and Engineering*, 146: 371–386, 1997.

[7] P.W. Randles and L.D. Libersky. Recent improvements in sph modeling of hypervelocity impact. *International Journal of Impact Engineering*, 20: 525–532, 1997.

[8] W. K. Liu, S. Jun, and Y. F. Zhang. Reproducing kernel particle methods. 20:1081–1106, 1995.

[9] C.A.M Duarte and J.T. Oden. An h-p adaptive method using clouds. *Computer Methods in Applied Mechanics and Engineering*, 1996.

[10] T. Strouboulis, K. Copps, and I. Babuška. The generalized finite element method: An example of its implementation and illustration of its performance. *International Journal for Numerical Methods in Engineering*, 47 (8):1401–1417, 2000.

[11] J.S. Chen, C.T. Wu, S. Yoon, and Y. You. A stabilized conforming nodal integration for galerkin meshfree-methods. *International Journal for Numerical Methods in Engineering*, 50:435–466, 2001.

[12] C.T. Dyka and R.P. Ingel. An approach for tensile instability in smoothed particle hydrodynamics. *Computers and Structures*, 57:573–580, 1995.

[13] P.W. Randles and L.D. Libersky. Normalized sph with stress points. *International Journal for Numerical Methods in Engineering*, 48:1445–1462, 2000.

[14] P. Krysl and T. Belytschko. Element-free galerkin method: Convergence of the continuous and discontinuous shape functions. *Computer Methods in Applied Mechanics and Engineering*, 148:257–277, 1997.

[15] D. Organ, M. Fleming, T. Terry, and T. Belytschko. Continuous meshless approximations for nonconvex bodies by diffraction and transparency. *Computational Mechanics*, 18:225–235, 1996.

[16] T.G. Terry. Fatigue crack propagation modeling using the element free galerkin method. *Master thesis, Northwestern University*, 1994.

[17] T. Belytschko and M. Fleming. Smoothing, enrichment and contact in the element-free galerkin method. *Computers and Structures*, 71:173–195, 1999.

[18] M. Fleming, Y.A. Chu, B. Moran, and T. Belytschko. Enriched element-free galerkin methods for crack tip fields. *International Journal for Numerical Methods in Engineering*, 1997.

[19] A. Hansbo and P. Hansbo. A finite element method for the simulation of strong and weak discontinuities in solid mechanics. *Computer Methods in Applied Mechanics and Engineering*, 193(33-35):3523–3540, 2004.

[20] J. Chessa, H. Wang, and T. Belytschko. On the construction of blending elements for local partition of unity enriched finite elements. *International Journal for Numerical Methods in Engineering*, 57(7):1015–1038, 2003.

[21] G. Zi, J.-H. Song, E. Budyn, S.-H. Lee, and T. Belytschko. A method for grawing multiple cracks without remeshing and its application to fatigue crack growth. *Modelling and Simulation in Materials Science and Engineering*, 12(1):901–915, 2004.

[22] G.C. Shih. Strain energy density factor applied to mixed-mode crack problems. *International Journal of Fracture*, 10:305–321, 1974.

[23] C-H Wu. Fracture under combined loads by maximum energy release rate criterion. *Journal of Applied Mechanics*, 45:553–558, 1978.

[24] R.V. Goldstein and R.L. Salganik. Brittle fracture of solids with arbitrary cracks. *International Journal of Fracture*, 10:507–527, 1974.

[25] M. Ortiz, Y. Leroy, and A. Needleman. Finite element method for localized failure analysis. *Computer Methods in Applied Mechanics and Engineering*, 61(2):189–214, 1987.

[26] T. Belytschko, J. Fish, and B. Englemann. A finite element method with embedded localization zones. *Computer Methods in Applied Mechanics and Engineering*, 70:59–89, 1988.

[27] E. N. Dvorkin, A. M. Cuitino, and G. Gioia. Finite elements with displacement interpolated embedded localization lines insensitive to mesh size and distortions. *International Journal for Numerical Methods in Engineering*, 30:541–564, 1990.

[28] H.R. Lofti and P.B. Shing. Embedded representation of fracture in concrete with mixed finite elements. *International Journal for Numerical Methods in Engineering*, 38:1307–1325, 1995.

[29] F. Zhou and J.F. Molinari. Dynamic crack propagation with cohesive elements: a methodolgy to address mesh dependence. *International Journal for Numerical Methods in Engineering*, 59(1):1–24, 2004.

[30] H.D. Espinosa, P.D. Zavattieri, and S. Dwidivedi. Adaptive fem computation of geometric and material nonlinearities with application to brittle failure. *Special issue of Mechanics and Materials*, 29(3-4):275–305, 1998.